GEORG-AUGUST-UNIVERSITÄT GÖTTINGEN

II. Physikalisches Institut

Dynamic Efficiency Measurements for Irradiated ATLAS Pixel Single Chip Modules

von

Mike Pfaff

The ATLAS pixel detector is the innermost subdetector of the ATLAS experiment. Due to this, the pixel detector has to be particularly radiation hard. In this diploma thesis effects on the sensor and the electronics which are caused by irradiation are examined. It is shown how the behaviour changes between an unirradiated sample and a irradiated sample, which was treated with the same radiation dose that is expected at the end of the lifetime of ATLAS. For this study a laser system, which is used for dynamic efficiency measurements was constructed. Furthermore, the behaviour of the noise during the detection of a particle was evaluated studied.

GEORG-AUGUST-UNIVERSITÄT

GÖTTINGEN

II. Physikalisches Institut

Dynamic Efficiency Measurements for Irradiated ATLAS Pixel Single Chip Modules

von

Mike Pfaff

aus

Kassel

Contents

1 Introduction

One of the most fundamental questions in physics is the one for the structure of matter and for its smallest components. The first person who found one of these elementary particles was Joseph John Thomson, who discovered the electron in 1898. From that time on physicist have been getting closer to the answer for the question for the fundamental structure of matter. In the first quarter of the last century the components of the atomic nucleus, the neutrons and protons, and the mediator of the electromagnetic force, the photon, were discovered.
Until the middle of that century further particles, like pions or muons, were discovered in cosmic radiation. By reaching higher energies and with the beginning of the use of collider experiments a large number of new particles were discovered.
To describe and predict the properties and interactions of these particles the standard model of particle physics was invented. This model predicts particle interactions with a very high precision and has, until now, passed every test. Only one of the particles that were predicted by the standard model has not been found yet, the Higgs boson.
But despite its success the standard model leaves some questions unanswered. More than 100 years after the discovery of the first elementary particle, questions like the hierarchy problem or the matter-antimatter asymmetry in the universe are still open. To answer these questions different standard model extensions, like supersymmetry, have been conceived.
For the discovery of the Higgs boson and the verification of these standard model extensions the Large Hadron Collider (LHC) was built. The LHC will allow the testing of possible standard model extension with a high precision. Furthermore the center of mass energy of the LHC is supposed to be high enough to find the standard model Higgs boson.
One of the four experiments in progress at the LHC is the ATLAS (A Toridal LHC ApparatuS) detector. ATLAS is, additionally to CMS, one of the two experiments which cover the whole range of physics questions handled at the LHC. The ATLAS detector consists of different sub-detectors, which are arranged in an onion like structure around the interaction point. The pixel detector is the innermost subdetector of ATLAS. It is that part of the inner tracking system which provides the best spatial resolution. Because of the small distance to the interaction point the pixel detector is irradiated very heavily.
The irradiation of the detector modules impairs the performance of the detector. If the radiation dose gets to high, it is even possible that the modules fail. For the understanding and the prediction of the change of the detector performance test measurements have to be done. The changes in the hit detection efficiency and the time behaviour at different irradiation fluences have to be surveyed. Only with this knowledge it is possible to make statements about the detector performance and lifetime.

In chapter 2 an overview on the physics that are handled at the LHC and a description of the LHC and the ATLAS detector is given. Chapter 3 describes the ATLAS pixel detector explicitly. It is shown how a traversing particle is measured and how the signal is created in the sensor. For this, the functional principles of the sensor and the electronics are described.
Chapter 4 deals with the setup of the measurements. For dynamic efficiency measurements a laser system was set up, whose sub-components and performance are described.

In chapter 5 the evaluated modules are described. The performances of an unirradiated and an irradiated sample are shown and compared to each other. These measurements are shown in chapter 6, where time resolved measurements with the help of the laser system are described. Finally chapter 7 shows the behaviour of the noise of an unirradiated module when a pixel of a module is hit by a particle. This noise level is compared to the noise without a hit to study a possible noise increase when the module processes a particle hit.

2 The Large Hadron Collider and the ATLAS Experiment

This chapter will give a short overview on the standard model of particle physics and possible extensions of the standard model. Testing the standard model and verifying standard model extensions is one of the goals of the Large Hadron Collider (LHC). Furthermore, a short overview on the LHC and the ATLAS experiment, which is one of the four big experiments at the LHC, will be given.

2.1 The Standard Model of Particle Physics and Beyond

The standard model of particle physics (SM) describes the properties of and the interactions between elementary particles. The standard model consists of 12 elementary spin 1/2 particles, which are called fermions. These 12 particles can be divided into two groups of 6 particles each, the leptons and the quarks. The interaction of these particles is described by three forces that are transmitted by spin 1 bosons [1].

Figure 2.1: Overview on the standard model particles [2], the Higgs boson is not shown.

The fermions can be arranged in three generations. Most of the matter around us is built up by particles from the first generation, like electrons or up and down quarks, which are the constituents of neutrons and protons. The particles of the higher generations are much heavier than these of the first generation and therefore not stable. Figure 2.1 shows the 12 standard

model fermions and the four force transmitting bosons. Not shown is the last standard model particle that was not discovered until now, the Higgs boson. To each standard model fermion there belongs a standard model anti particle. These anti particles have the same properties like the fermions, but the opposite charge sign. Quarks also carry a color charge with the three states red, green and blue.

The fermions can interact by three forces. The electromagnetic force is mediated by photons. It couples to every charged particle. Photons have no mass, so the force has an unlimited range. The weak force is mediated by the W and Z bosons. These bosons have high masses and the force has a short interaction length. All fermions interact by weak force.

The strong force is mediated by 8 gluons that have no mass. The strong force couples to those particles who carry a color charge. These are the quarks and the gluons themself. Strong interacting particles only appear in bound states, so they can't be observed as single particles. Quarks are bound in baryons with three quarks or mesons with two quarks.

The standard model is a locally gauge invariant theory, which leads to gauge bosons without mass. However, in experiments the W and Z gauge bosons were found to have masses of $m_{W^\pm} = 80.398 \pm 0.025\,\text{GeV}$ and $m_Z = 91.1876 \pm 0.0021\,\text{GeV}$ [3]. To explain these masses the Higgs mechanism was proposed. This mechanism creates a scalar background field by spontaneous symmetry breaking and leads to the massive spin 0 Higgs boson. Finding this particle is one of the goals of the LHC. The SM predicts all parameters of the Higgs boson, except the mass. Higgs masses below $114.4\,\text{GeV}$ could be excluded by other experiments [4]. The maximum Higgs mass is, due to theoretical considerations, $1\,\text{TeV}$. In this range, the LHC is capable to find the Higgs boson.

There are open questions in the SM. Like the question for a fundamental force, or the hierarchy problem. Many extensions try to explain these questions. One of the promising ones is supersymmetry (SUSY). In this theory every spin 1 boson gets an identical spin 1/2 fermion as super partner and every spin 1/2 fermion gets an identical spin 1 boson as super partner. SUSY has to be a broken symmetry, because if the super partners of the standard model particles had the same mass as the standard model particles they would have to be discovered already. So if SUSY is realized in nature the supersym
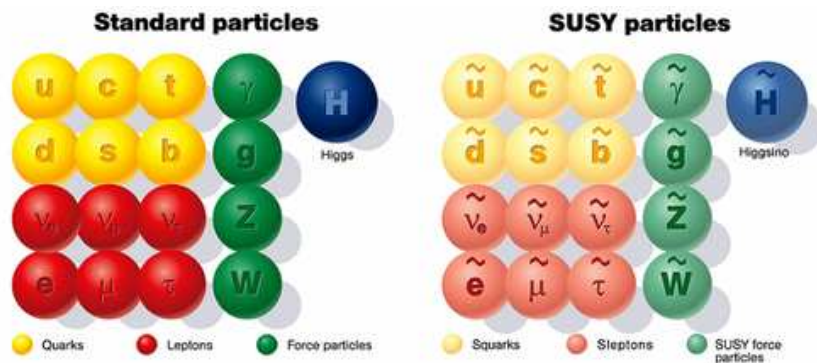
Figure 2.2: Left: Standard model particles with Higgs boson, right: supersymmetric partners of the standard model particles [5].

2.2 The Large Hadron Collider
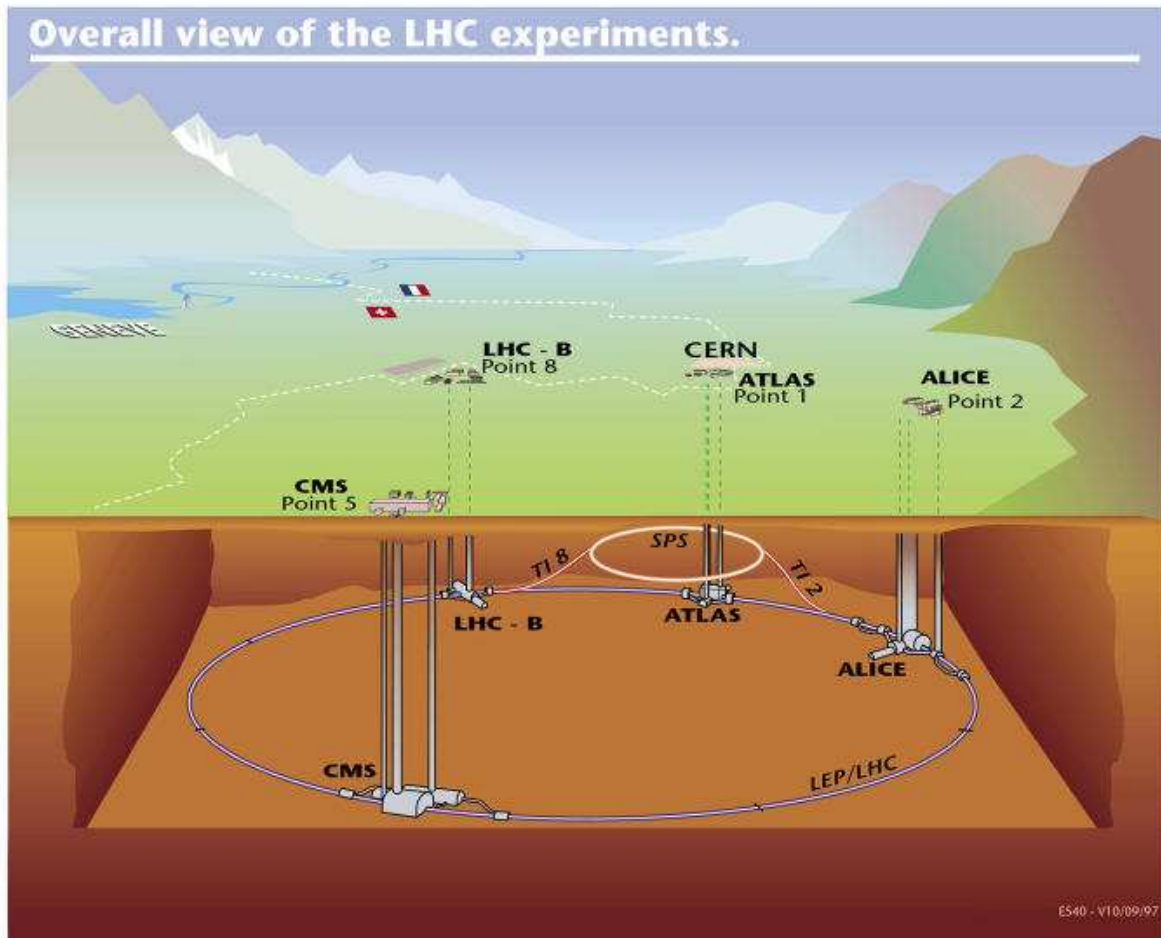
Figure 2.3: Overview of the LHC [6].

The Large Hadron Collider (LHC) is the world largest proton-proton collider and located at CERN close to Geneva. The LHC is a ring collider with a diameter of 27 kilometers. The machine is built in a tunnel 100 meters below the ground level. This tunnel was previously used by the LEP collider. The LHC is designed for center of mass energies up to 14 TeV. At the design luminosity of $10^{34}\,\mathrm{cm}^{-2}\mathrm{s}^{-1}$, there will be 2808 proton packages with $1.1 \cdot 10^{11}$ protons in the collider. At the interaction points the collisions take place with a rate of 40 MHz. At each collision there are about 20 inelastic interactions with over 1000 produced charged particles. The design values for the proton-proton collisions are given in table 2.1.

Inside the LHC, the protons rotate in two different beam pipes in opposite direction. On four interaction points the proton beams collide. At these four points the big experiments of the LHC are installed. ATLAS and CMS cover the whole spectrum of physical questions handled at the LHC. The LHC-B experiment is specially designed for B-physics. The fourth experiment, ALICE, is for measurements in a heavy ions mode. For the ALICE experiment, not protons, but lead ions are accelerated and collided inside the LHC.

ring circumference	26658.883 m
magnet field strength	8.33 T
bending radius	2803.95 m
number of proton packages	2808
protons per package	$1.1 \cdot 10^{11}$
distance of packages	25 ns
collision rate	40 MHz
design luminosity	$10^{34} \, \text{cm}^{-2}\text{s}^{-1}$

Table 2.1: Design parameters of the LHC in proton-proton mode [7].

Until the end of 2010 the LHC has reached a luminosity of $2 \cdot 10^{32} \, \text{cm}^{-2}\text{s}^{-1}$. The maximal number of bunches inside the collider has been 368 [8].

There are different upgrade possibilities for the LHC. One possibility is to increase the design luminosity from $10^{34} \, \text{cm}^{-2}\text{s}^{-1}$ by a factor of ten to $10^{35} \, \text{cm}^{-2}\text{s}^{-1}$. Another possibility is to increase the center of mass energy by a factor of two to 24 GeV. The second possibility is the more complicated and much more expensive one, so the first one is favored [9].

2.3 The ATLAS Experiment
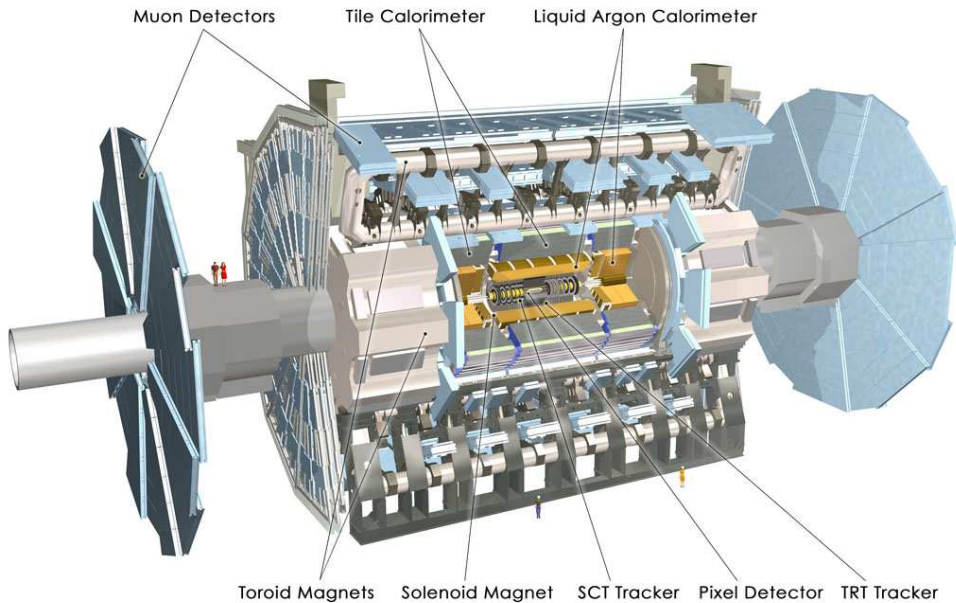
Figure 2.4: The ATLAS Detector with subdetectors [10].

The ATLAS detector has a diameter of 25 meters, a length of 46 meters and a weight of 7000 tons. The detector is a classical 4π detector. That means that the whole solid angle is covered by the detector. Only a very small part through which the beam pipes go into and out of the detector is not covered. The detector is built in the standard collider detector architecture. That means, that there are different subdetectors for different tasks.

The innermost part of the detector is the tracking system. Here the particle tracks are measured.

The tracking system consists of three subdetectors. The innermost one is a semiconductor pixel detector. It is followed by a silicon microstrip detector (SCT) and a transition radiation tracker (TRT). The inner detector system is surrounded by a solenoid magnet, so transverse momentum can be measured with the tracking system.

The next part of the detector is the calorimeter system. Here the particles are stopped and their energy is measured. The calorimeter system consists of two subdetectors, the electromagnetic calorimeter and the hadronic calorimeter.

The outermost part of the ATLAS detector is the muon system. It consists of a huge toroid magnet and a muon tracker. Muons are the only charged particles that can leave the calorimeter system. With the magnetic field and the muon tracker the momentum of the muons can be measured.

With this detector structure different goals can be reached. Because of the 4π geometry the whole event can be detected and missing transverse energy[1] can be related to neutrinos or new unknown particles. Because of the huge volume of the muon tracking system a precise measurement of the muon momentum is possible. With the inner detector system a very precise tracking is possible. Furthermore, the interaction point can be located very precisely.

2.3.1 The Inner Detector and the Solenoid Magnet
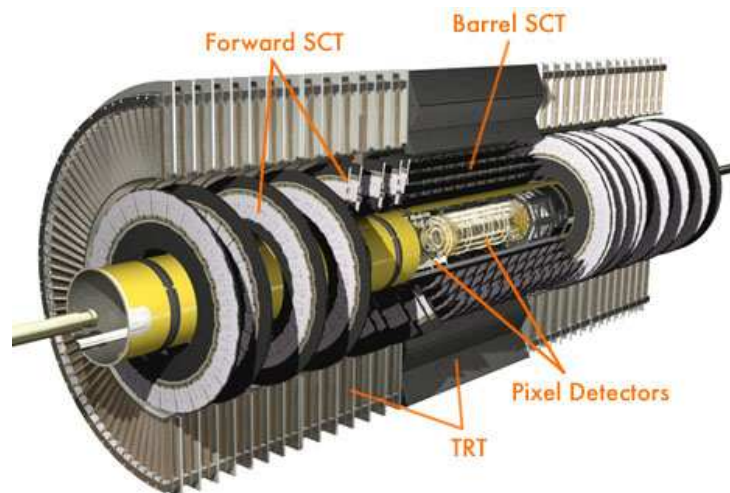
Figure 2.5: The inner detector system [10].

The inner detector consists of 3 subdetectors: the pixel Detector, the silicon strip detector (SCT) and the transition radiation tracker (TRT). The whole inner detector system is embedded into a 2 T solenoidal magnetic field. With this tracking system a very precise measurement of particle momentum is possible. The relative momentum resolution is $\sigma/p = (4.83 \pm 0.16) \cdot 10^{-4}\,\mathrm{GeV}^{-1} \cdot p_T$ [11]. The whole inner detector has a length of 7 meters and a diameter of 2.3 meters.

The pixel detector has the best resolution of the whole detector and is nearest to the interaction point. So a good tracking is possible. With this the position of the interaction point and

---

[1]Transverse energy is that part of the momentum which is not parallel to the beam axis. Before the protons collide, the transverse energy is zero. Because of the conversation of energy it can be checked if the detector had detected every particle of the event.

secondary decay vertices can be measured precisely. The pixel detector consists of 3 barrel layers around the beam pipe and 2 endcaps with 3 disks each in forward and backward direction. So the pixel detector supplies 3 space points on average. An exact description of the pixel detector follows in chapter 2.

The SCT is the next subdetector system. It consists of 4 barrel layers and 2 endcaps with 9 disks each. The resolution in $R\phi$ plane is 16 µm and 580 µm in z direction [12]. The detector consists of single sided p-in-n microstrip sensors which are glued back to back. The strips are rotated against each other by about 40 mRad, so that two-dimensional hit information is created. The detector has 6.2 million read out channels.

The outermost part of the inner detector is the TRT. This is a system of straw tubes which typically yield 36 track points per particle. This detector has a spatial resolution of 170 µm per straw [10]. The barrel TRT tubes are arranged in parallel to the beampipe. The endcap tubes are arranged in planes perpendicular to the beam direction. The subdetector has 420000 readout channels. Every single tube is filled with a gas mixture and a sense wire. Every time a particle traverses a tube wall, photons are emitted. The intensity of this transition radiation depends on the $\gamma = E/m$ of the particle. Light particles emit more transition radiation than heavy ones, so it can be distinguished between electrons and heavy particles. Direct ionization caused by traversing particles is also detected.

Outside of the inner detector the superconducting solenoid magnet is installed. The magnet is 5.3 meters long and 2.4 meters in diameter. The magnet requires a current of 7600 A and creates an axial magnetic field with peak field strength of 2.6 T.

Figure 2.6: The ALTAS solenoid magnet [10].

2.3.2 The Calorimeter System

Once the particles have left the inner detector system they reach the calorimeter system. Here they are stopped (except of neutrinos and muons) and deposit their whole energy in the calorimeters. The calorimeters are designed to measure this deposited energy very precisely. The calorimeter system consists of the electromagnetic calorimeter and the hadronic calorimeter. The innermost one is the electromagnetic calorimeter, which stops gammas and electrons. But

also hadrons deposit a little energy here while they cross the electromagnetic calorimeter. The electromagnetic calorimeter is a liquid argon calorimeter built in sampling architecture. Lead is used as absorber.

The hadronic calorimeter is for the measurement of hadron energies. It is a sampling calorimeter, too, but with steal as absorber and plastic scintillators as active medium. Both calorimeters are approximately 20 interaction lengths[2] thick, so nearly all particles are stopped in the calorimeters.

2.3.3 The Muon Chambers and the Toroid Magnet

The endmost subsystem of the ATLAS detector is the muon and toroid magnet system. Muons are the only charged particles which can leave the calorimeters. So if a track is seen in the muon system, it has to be from a muon. The muon system measures the particle track in a magnetic field, so the transversal momentum can be calculated.

The magnetic field for the muon chambers is created by a superconducting toroid magnet. The toroid consists of eight barrel coils and two endcaps. The barrel coils are 25.3 meters long. They begin at a radius of 9.4 meters and end at 20.1 meters. They can produce a peak magnetic field of 3.9 T. The endcaps begin at a radius of 1.65 meters and end at 10.7 meters. They create a peak magnetic field of 4.1 T.
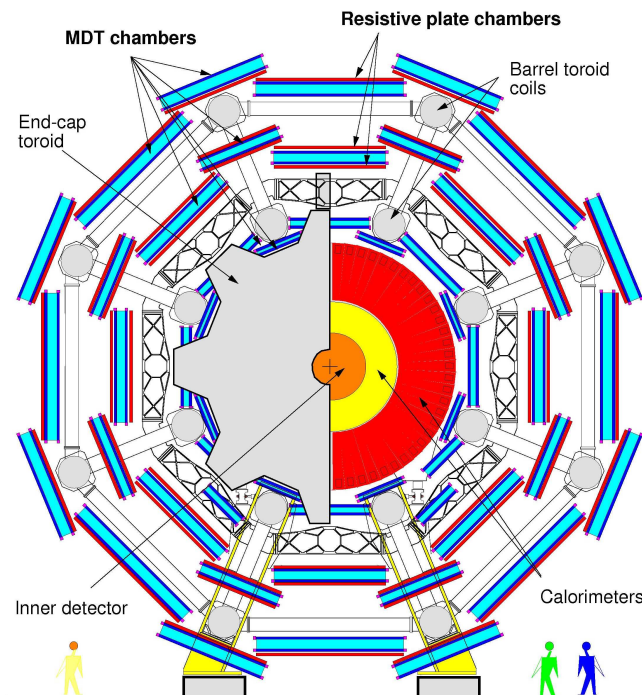
Figure 2.7: The toroid magnet system and the muon system [13].

The muon system consists of different detector types. There are resistive plate chambers (RPCs) operating in avalanche mode in the barrel region. In the endcap region there are thin gap chambers (TGCs) operating in saturated mode. These two detector types are very fast and

---

[2]The Interaction length is the length required to reduce the energy of charged particles by the factor $1/e$ as they pass through matter.

used for triggering. For high resolution measurements drift tubes (MDTs) are used for a pseudo-rapidity[3] smaller than two. These MDTs are drift chambers made of aluminum and filled with a gas mixture that survives high doses of radiation without aging. In the pseudorapidity region between 2 and 2.7 cathode strip chambers (CSCs) are used. These are multi-wire proportional chambers. The MDTs and CSCs have a spatial resolution of approximately 50μm.

---

[3]Pseudorapidity η is defined as $\eta = ln\,tan\frac{\theta}{2}$. θ is the polar angle of the particle relative to the beam line.

3 The Pixel Detector
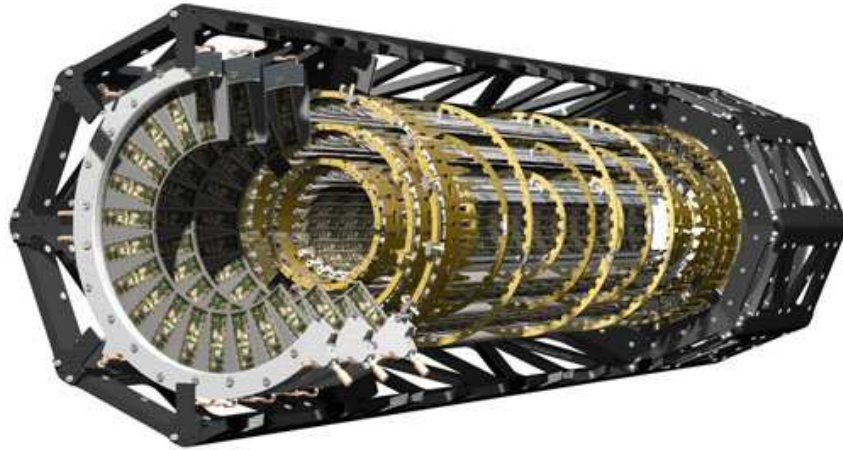
Figure 3.1: The ATLAS pixel detector [14].

The pixel detector is the innermost subdetector of the ATLAS experiment. Because of its small distance from the interaction point the particle flux is the highest of all subdetectors. This high particle flux is the reason why the pixeldetector has to be particularly radiation hard. Another consequence of the high flux is that the detector needs many readout channels to measure plenty particles at once. A higher number of readout channels results in a smaller pixel size. This improves the resolution of the detector, which causes a better reconstruction of the particle tracks. The whole pixel detector has approximately 80 million readout channels, which are connected to $400\,\mu$m long and $50\,\mu$m wide sensor pixels[1]. The spatial resolution of the pixel detector is the best of the whole ATLAS experiment. In the $R\phi$ plane it is $12\,\mu$m, in z direction (parallel to the LHC beamline) it is $115\,\mu$m [9]. This resolution is required to measure the position of the interaction point very precisely. In addition to that such a high resolution is needed for the measurement of secondary decay vertices.

The detector consists of three barrel layers and two endcaps with three disks each. The innermost barrel layer is called b-layer, the following ones are named layers one and two. In the barrel region 13 pixel modules, which are the smallest units of the detector (see chapter 3.1), are installed on one stave. The staves are similar for all three layers. Both the modules on the staves and the staves themselves are shingled in such a way that no gaps exist between the modules. The endcap disks consist of eight sectors each with three modules on the front and the backside. Also these modules are arranged so that there are no gaps between the modules. With this setup it is possible to provide at least three space points up to a pseudorapidity of $\eta = 2.5$. Table 3.1 shows the radii of the barrel layers, the z-positions of the disks and the numbers of staves, sectors and modules on the different layers and endcaps.

---

[1]For geometrical reasons there are also $600\,\mu$m $\times$ $50\,\mu$m pixels (see chapter 3.1.2).

	Radius (mm)	No. of staves	No. of modules
b-layer	55.5	22	286
Layer one	88.5	38	494
Layer two	122.5	52	676
	z-position (mm)	No. of sections	No. of modules
Disk 1	±495	8+8	48+48
Disk 2	±580	8+8	48+48
Disk 3	±650	8+8	48+48
Total			1744

Table 3.1: Setup and dimensions of the ATLAS Pixel detector [15].

3.1 The Pixel Module

The Pixel detector consists of 1744 pixel modules. They have a size of approximately $6.2 \times 2 \, cm^2$. One module consists of a silicon sensor, the Front-End electronics and a copper-capton-flex board (see figure 3.2). Each sensor is connected to 16 equal Front-End chips (FE-chips) in such a way that every sensor pixel has a link to its own read out cell.
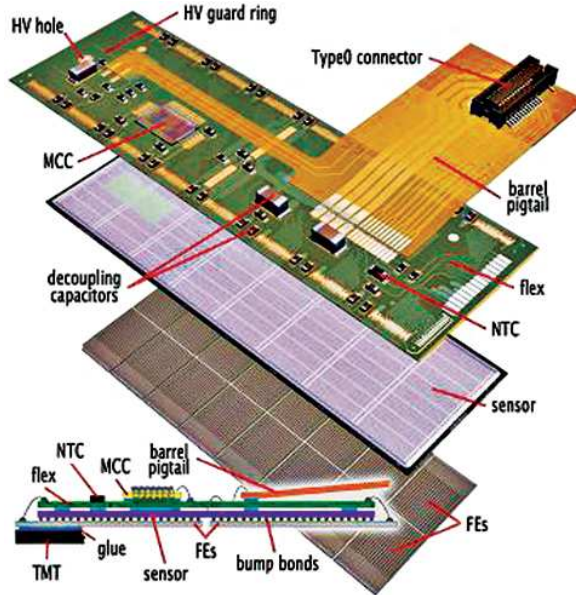
Figure 3.2: Schematic view on the pixel module [16].

The connections between the sensor and the FE-chips are provided by little metal pellets called bump bonds. There are two different kinds of bump bonds, which are made of lead-tin or indium. The reason for the appearance of two different kinds of bonds is that the bonding of the sensors and the FE-chips was done by two different facilities, by using different methods. The two kinds of bonds show slightly different behaviours. The indium bonds have a diameter of approximately $20 \, \mu m$ and a height of $8 \, \mu m$. They have a resistance of several ten ohms. The

lead-tin bonds have a spherical geometry with a diameter of $20\,\mu m$ and a resistance of less than one ohm [17].

On the back side of the sensor, the copper-capton-flex board is installed. The FE-chips and the flex board are connected with wire bonds that are located at the long edges of the module (see figure 3.2). On the board the Module Control Chip (MCC) is installed. This chip gathers hit information from the FE-chips, processes them and sends them to the off detector electronics. For temperature measurements a negative temperature coefficient thermistor (NTC) is installed on the flex board. In the following the sensor, the FE-chip and the MCC are described in detail.

3.1.1 The Sensor

Silicon Semiconductor Detectors

Depleted pn junctions of semiconductors can be used for the detection of charged particles [18]. When traversing a semiconductor, a charged particle deposits energy inside the material and, thereby, creates electron-hole pairs along the particle's path. If there exists an electric field, these electron-hole pairs are separated and start drifting towards the read-out electrodes, where they induce an electrical signal. If the semiconductor is not depleted, the electron-hole pairs will recombine immediately, and the measurement of a signal will be impossible.

The bandgap of silicon is $1.12\,\text{eV}$ [19]. Because of lattice vibrations and stimulation the required average energy for the production of an electron-hole pair is increased to $W = 3.62\,\text{eV}$ [20]. To calculate the mean energy loss $\langle dE/dx \rangle$ of a particle by traversing matter, the Bethe-Bloch equation can be used. For traversing particles with a mass much bigger than the electron mass the energy loss is given by

$$-\left\langle \frac{dE}{dx} \right\rangle = 2\pi N_a r_e^2 m_e c^2 \rho \frac{Z}{A} \frac{z^2}{\beta^2} \cdot \left[ln\left(\frac{2m_e\gamma^2 v^2 W_{max}}{I^2} - 2\beta^2 - \delta - 2\frac{C}{Z} \right) \right] \qquad (3.1)$$

with:

$N_a = 6.022 \cdot 10^{23}\,\text{mol}^{-1}$ is Avogadro's number.

$r_e = 2.817 \cdot 10^{-13}\,\text{cm}$ is the classical electron radius.

$m_e = 511\,\text{keV}$ is the mass of an electron.

$\rho = 2.33\,\text{g/cm}^3$ is the density of the absorbing material.

$I \approx 173\,\text{eV}$ is the average effective ionization potential.

$Z = 14$ is the atomic number of the absorbing material.

$A = 28$ is the atomic weight of the absorbing material.

z is the charge of the traversing particles in units of e.

$\beta = v/c$ is the speed of the traversing particle in terms of the light speed c.

$\gamma = 1/\sqrt{1 - \beta^2}$.

δ is the density correction. It is important for higher energies and depends on the density of the traversing material.

C is the shell correction. It reduces the energy loss at lower energies and occurs with the wrong assumption that there are stationary electrons inside the material.

$W_{max} = 2m_e c^2 \beta^2 \gamma^2$ is the maximum energy transfer in a single head on head collision (for $M >> m_e$).

The shown formula is valid down to $\beta\gamma \approx 0.1$. Its minimum is at $\beta\gamma \approx 3.5$. Particles with corresponding or higher $\beta\gamma$ are called minimum ionizing particles (MIPs). An example for the Bethe-Bloch equation is given in figure 3.3. In $250\,\mu m$ silicon the average energy loss of a MIP is approximately $69.9\,\text{keV}$, which corresponds 19300 electron hole pairs [21].
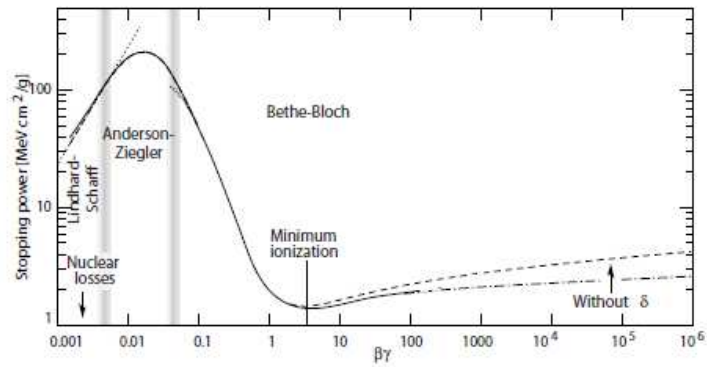
Figure 3.3: Bethe Bloch equation for the energy loss of a muon in copper [9].

The ATLAS Pixel Sensor

The ATLAS Pixel sensor [22] has the following dimensions $63 \times 18.6 \times 0.25 \, \text{mm}^3$. By cutting the sensor out of the waver, on which it is produced, lattice damages can occur. At these damages current paths can occur. To protect the sensor pixels against those current paths, 17 guard rings are implemented at the edges of the sensor. This leads to an active sensor area of $60.8 \times 16.4 \, \text{mm}^2$. The sensor is built in the n in n design. This means that the bulk of the sensor is n doped, on one side higher n doped pixels are implemented into the bulk. The other side of the sensor is p^+ doped. Here also the guard rings are implemented.

Due to the short distance between the interaction point and the Pixel detector the modules are irradiated with a very high radiation dose. The n in n pixel technology is well suited to withstand such high doses. If the sensor material is irradiated the effective doping concentration changes and becomes p like. So in the course of time the n doped bulk changes to a p doped one (see figure 3.4).

For particle detection the sensor has to be depleted. If it is not, the produced electron-hole pairs recombine immediately. For the depletion of the sensor a bias voltage is applied. At an unirradiated sensor the depletion zone grows from the p doped side of the sensor (see figure 3.4 top). Here the sensor has to be fully depleted, if it is not, the pixels are not insulated against each other and particle detection is not possible. For the full depletion of an unirradiated sensor a bias voltage of -60 V is enough[2]. If the sensor is irradiated, the depletion zone grows from the pixel side of the sensor (see figure 3.4 bottom). Here the pixels are isolated against each other, even if the sensor is not fully depleted. If this is the case, particle detection is still possible, whereas the amplitude of the sensor signal is smaller than with a fully depleted sensor. The ATLAS detector is validated for bias voltages of up to -600 V, the guard rings of the sensor do survive bias voltages up to -1000 V.

The ATLAS Pixel sensors are made of oxygenated silicon, which shows a very good performance as sensor material. Figure 3.5 shows the effective doping concentration and the bias voltage that is needed for the full depletion of the sensor. On the x-axis an LHC runtime of ten years is shown. The effective doping concentrations for the b-layer and layer one are shown (solid lines). The dashed lines show the performance for a scenario with a 50% increased particle fluence. It can be seen that for layer one, after ten years LHC runtime, the depletion voltage does not exceed -600 V. For the b-layer this border is reached after approximately six years. For

---

[2]To secure that at the sensor electrodes, the electrical field is not zero, a bias voltage of -150 V has to be applied.
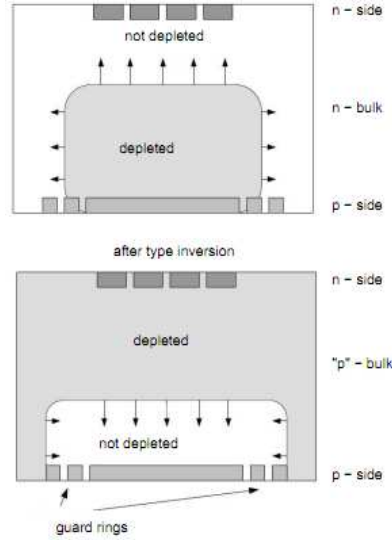
Figure 3.4: Growing of the depletion zone of a pixel before and after irradiation [23].

this reason it is planed to insert an additional b-layer after five years runtime[3]. The pixel modules are designed for a radiation dose of 10^{15}cm^{-2} neutron equivalent[4]. This is the calculated dose, which a module is exposed to at the end of the ATLAS lifetime.
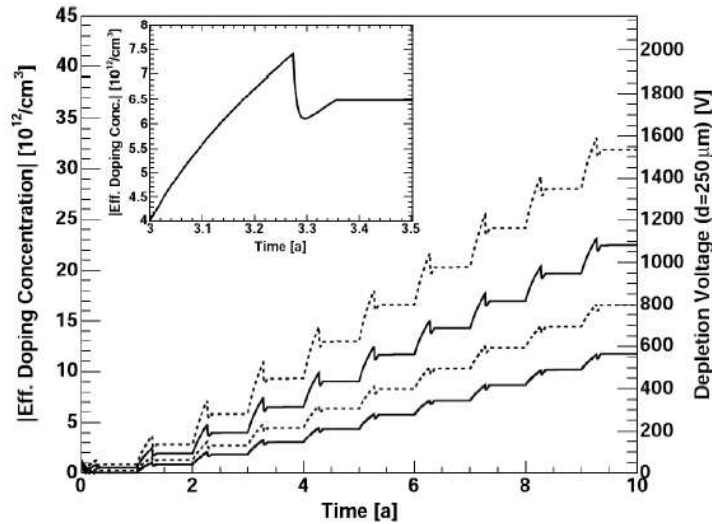
Figure 3.5: Depletion voltage for oxygenated silicon (solid lines) as a function of the LHC operation time. The dashed lines show the performance for a 50% increased particle fluence. Also shown is the effective doping concentration. The upper lines show the b-layer, the lower ones layer one. [25].

The aging effects of the sensor are temperature dependent. Tests showed that the optimal operating temperature for the sensor is -10°C. At any time, thermal free charge carriers are produced inside the sensor material. The number of these charge carriers, and with that also

---

[3]The insertable b-layer project (IBL).

[4]"The 1 MeV equivalent neutron fluence is the fluence of 1 MeV neutrons producing the same damage in a detector material as induced by an arbitrary particle fluence with a specific energy distribution" [24].

the leakage current of the sensor, depends on $T^{3/2}$ [9]. This is the reason why cooling of the sensor reduces the leakage current. After the irradiation of a sensor, this becomes especially important, because then the leakage current is increased.

If the sensor is warmed up from time to time, the material defects, which were created by the radiation, heal out. This effect is called annealing. If the sensor is warmed up too long, the sensor properties start getting worse again. To use this annealing effect, the sensor is warmed up once a year, during the LHC run pause for a couple of days. This annealing effect can be seen at the knees of figure 3.5.

3.1.2 The Front-End Chip

The pixel side of each sensor is connected to 16 similar FE-chips (see figure 3.6 top). The FE-chips contain one read out cell (FE-pixel) for each sensor pixel. In these cells the sensor signals are amplified and digitized. At the edges, where the FE-chips border on each other, dead areas emerge. To avoid such dead areas in the sensor surface, the sensor pixels are modified. In the long pixel direction the sensor pixels at the edges are extended from 400 to 600 μm. In the short pixel direction four rows of FE-pixels are connected to two sensor pixels each. The connection of these four pixels is done in such way that only every other of the topmost eight FE-pixels is connected to a sensor pixel in the dead region (see figure 3.6 bottom). These pixels are called ganged pixels, whereas the pixels between the ganged pixels are called interganged pixels.
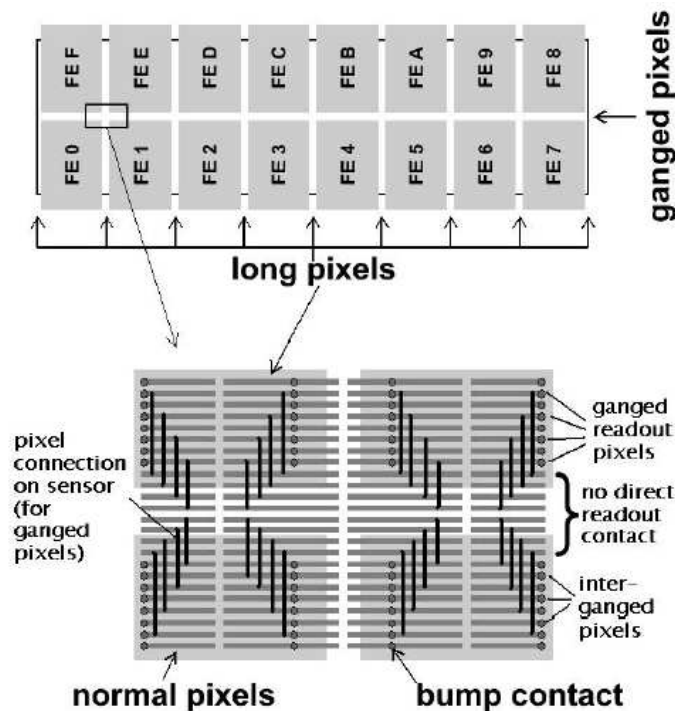
Figure 3.6: Top: Positions of the 16 FE-chips under the sensor. Bottom: Layout of the sensors between 4 adjacent FE-chips [9].

The FE-chip has the dimensions of $7.2 \times 10.8\,\text{mm}^2$. The FE-pixels are arranged in 9 double columns and 160 rows, adding up to 2880 pixels on one FE-chip. Every FE-pixel consists of an analogue and a digital read out part.

Figure 3.7 shows a schematic of a whole FE-chip, while figure 3.8 shows the circuit of one

single FE-pixel. The signal is transmitted from the sensor through a bump bond to the FE-pixel. Here it is amplified and digitized by a very fast discriminator. The threshold of this discriminator can be set between zero and 12000 electrons. If a signal is above the threshold, the rising edge of the discriminator output signal gets a timestamp and the time between rising and falling discriminator edge is calculated ("time over threshold" or TOT). Each discriminator is connected to a fast OR, called hitbus. The hit information is sent to the end of column buffers (EoC buffers), where it is stored. In the EoC buffers the address of the hit, the timestamp of the rising discriminator edge and the TOT are stored. If these information have reached the EoC buffers, they are erased from the FE-pixels. From this moment forth the cell is ready to detect a new hit. If a trigger is sent to the FE-chip, the information of the corresponding EoC buffers is read out to the MCC.
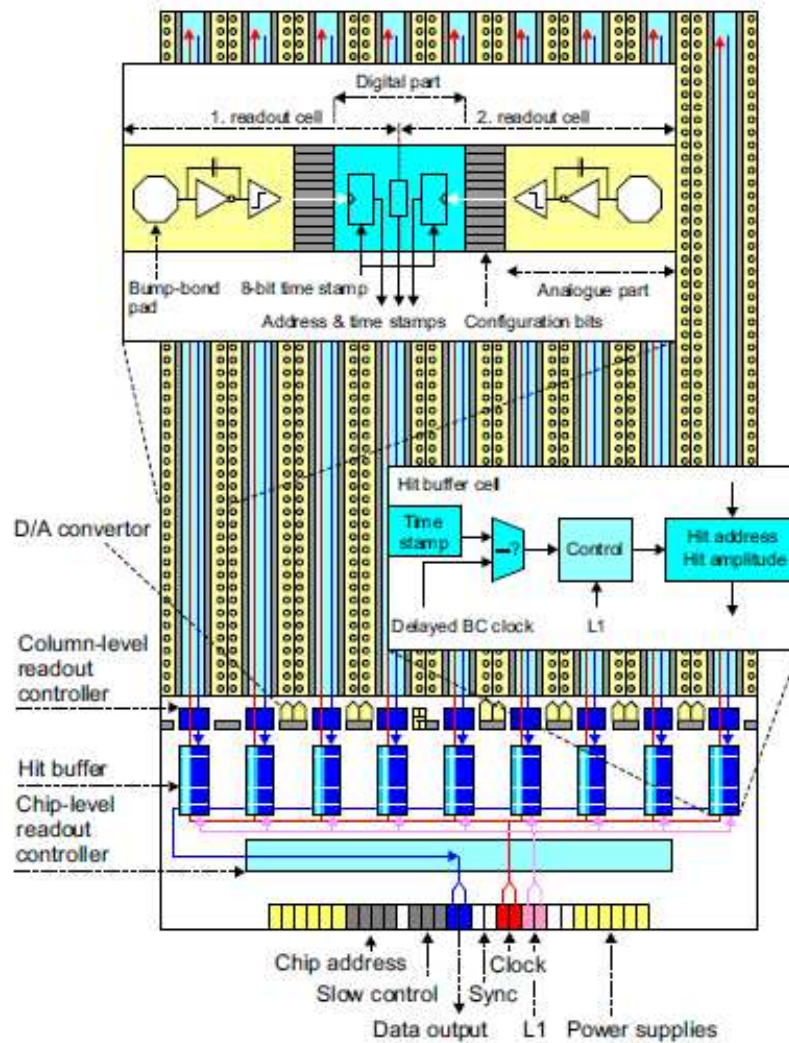
Figure 3.7: Schematic of a FE-chip [9].

For the testing of the module and for adjustment of the threshold and TOT, a test system was implemented on the FE-chips. With the help of two capacitors in each FE-pixel ($C_{low} \approx 7\,$fF and $C_{high} \approx 40\,$fF), well known charges can be injected into the read out chain, and the FE-chip response can be measured. With a switch between the supply voltage and a voltage controlled
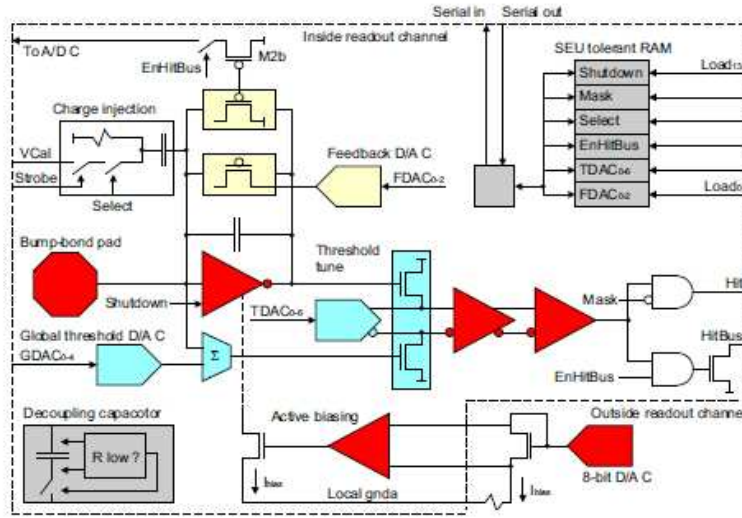
Figure 3.8: Circuit of one front end read out cell [9].

by a DAC[5], called V_{cal}, the capacitors can be charged, and so a signal similar to a sensor signal is created. The switch is controlled by an external signal, called strobe.

For test measurements it is also possible to disable different parts of an FE-pixel. The strobe, the preamplifier, the hitbus and the whole read out of a pixel can be disabled separately.

The Threshold

The threshold of the discriminator can be set between zero and 12000 electrons. If the charge that is created in the sensor is above the threshold, the pixel shows a hit. The ATLAS standard setting for the threshold is 4000 electrons. If it is set much lower (e.g. 2500 electrons), the FE-chip starts creating noise hits. The threshold can be set with two DAC's. For the whole FE-chip, the threshold can be changed by a global 5 bit DAC called G-DAC. For a fine tuning the 7 bit trim DAC (T-DAC) can be set separately for every pixel. With the two DACs it is possible to set the threshold for a whole sensor to the same value with an accuracy of approximately 15 electrons. The noise of the system is $\sigma_{noise} < 200$ electrons.

To measure the threshold charge $Q_{threshold}$, the threshold scan is used. This scan injects different charges into the read out chain of the FE-chips and measures the number of collected hits for a specific charge. As a result of this scan a step function should be created. Because of noise, however, charges near the threshold sometimes trigger, sometimes they do not. This behaviour results in the creation of the following s-curve function:

$$p_{hit}(Q) = Erfc\left(\frac{Q_{threshold} - Q}{\sqrt{\sigma_{noise}}}\right) \tag{3.2}$$

here Q is the injected charge and p_{hit} is the hit probability.

---

[5]Digital analogue converters.
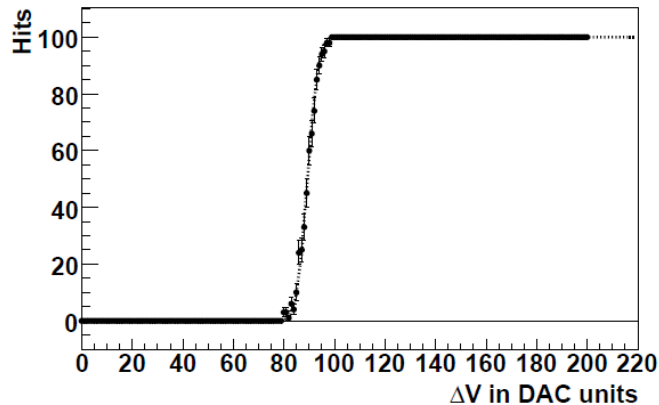
Figure 3.9: Number of hits as a function of the V_{cal} value fitted with a s-curve [9].

Time over Threshold

The signal generated by the sensor is amplified by a charge sensitive preamplifier. This preamplifier has a 10 fF feedback capacitor for charge collection, which is discharged by a constant current source. The discharging current can be regulated by two DAC's, a global 8 bit IF-DAC and a 3 bit F-DAC that can be set separately for every pixel. By these two DAC's a homogeneous amplifier recovery time for the whole FE-chip is ensured.
The recovery time of the amplifier, and with this the time over threshold of the discriminator output, depends on the charge that is produced by the traversing particle. This dependency is approximately linear [9]. So, with the IF-and F-DAC the TOT of the discriminator for a certain charge can be adjusted. The benchmark value for a charge of 20000 electrons is a TOT of 30 bunchcrossings. The described mechanism can be used for measuring the charge that a particle has created by traversing the sensor. In chapter 4.3.1 the procedure of a TOT-charge calibration is shown.

Timing and Timewalk

For reconstructing the particle track, it is necessary to ensure that the hits are associated with the correct 25 ns LHC bunchcrossing. Figure 3.10 shows the timing during charge injection with a strobe signal. A certain time after the strobe signal is sent, the preamplifier output starts rising and the discriminator output rises from zero to one. If a trigger signal is sent, the event corresponding to the bunchcrossing, which has occurred earlier by a time span called latency, is read out to the MCC. The bunchcrossing, which corresponds to the correct hit, is marked in green. The latency originates in the time the trigger system needs to make a decision. The trigger delay is the time between the strobe signal and the trigger signal. It has to be set in such way that the discriminator signal ends up in the correct acceptance window. One trigger can read out between one and 16 consecutive bunchcrossings. These bunchcrossings are labelled with numbers from 0 to 15, which are called LV1ID. In the ALTAS detector this LV1ID window is only one bunchcrossing long, because at every bunchcrossing collisions happen. For laboratory tests, however, it can be extended.
The rise time of the preamplifier is charge dependent. Lower charges result in longer rise times of the preamplifier, and with that in a later threshold crossing. If the collected charge is very small, it happens that the hit is not registered until the following bunchcrossing. This effect is called timewalk, it is illustrated in figure 3.11.
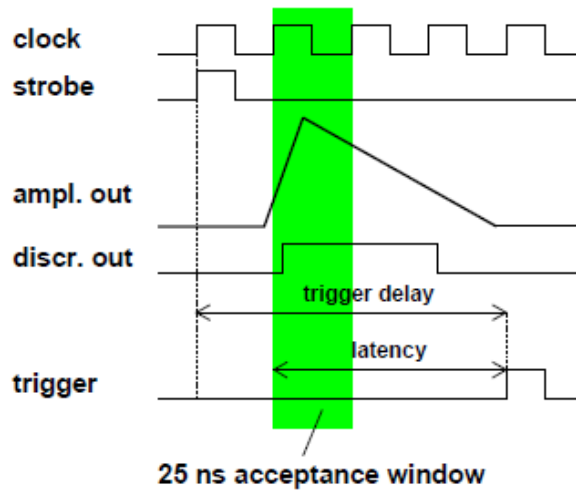
Figure 3.10: Sketch of the pixel read-out timing [9].
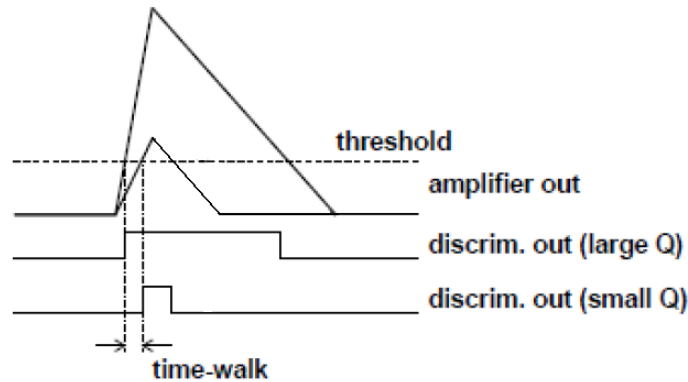
Figure 3.11: Amplifier output and discriminator response for small and large charges.

3.1.3 The Module Control Chip

The module control chip processes the data coming from the 16 FE-chips and handles the communication between the module and the ATLAS data taking system [9]. It receives the configuration data and distributes it among the different FE-chips. It also creates and distributes different reset and timing signals.

When the MCC receives the trigger signal from the ATLAS trigger system, it initiates the data readout from the FE-chips. The data is read out into 16 FIFO's[6], one for each FE-chip. With the whole data set from the 16 FE-chips the event is built and provided with a timestamp. Then it is forwarded to the further read out electronic and transformed into a serial data stream. Finally this data stream is sent to the ATLAS data taking system via two LVDS[7] data lines.

Another feature of the MCC is to test the read out chain between the FE-chips and the off detector electronic. The configurations sent to the FE-chips can be read back from the FE-chips. From the outside, artificial events can be sent in combination with a trigger, to the FIFO's, so the MCC data processing can be tested.

---

[6]First in first out buffers.
[7]Low voltage differential signals.

3.2 The USB-Pix System

For laboratory measurements an USB based test system was developed. With this system, which consists of a multi purpose IO-Board (S3MultiIO), an adapter card and a single chip module (see figure 3.12), it is possible to test the FE-chip and the sensor.

The Multi Purpose IO-Board

The Multi purpose IO-Board is equipped with a microcontroller with USB2.0 interface, an FPGA[8] and an SRAM[9] [26]. With the microcontroller the data transfer between the PC and the Multi purpose IO-Board is handled. The FPGA provides and handles the signal transfer to the FE-chip. Examples are: clock, trigger, reset signals or the configuration of the FE-chip. Moreover, it stores the data coming from the FE-chip on the 16Mbit SRAM.
The Multi purpose IO-Board provides a large number of connections, like the 100 pin connector for the connection to the adapter card, or six LEMO connectors, which can be used for signal in or output.
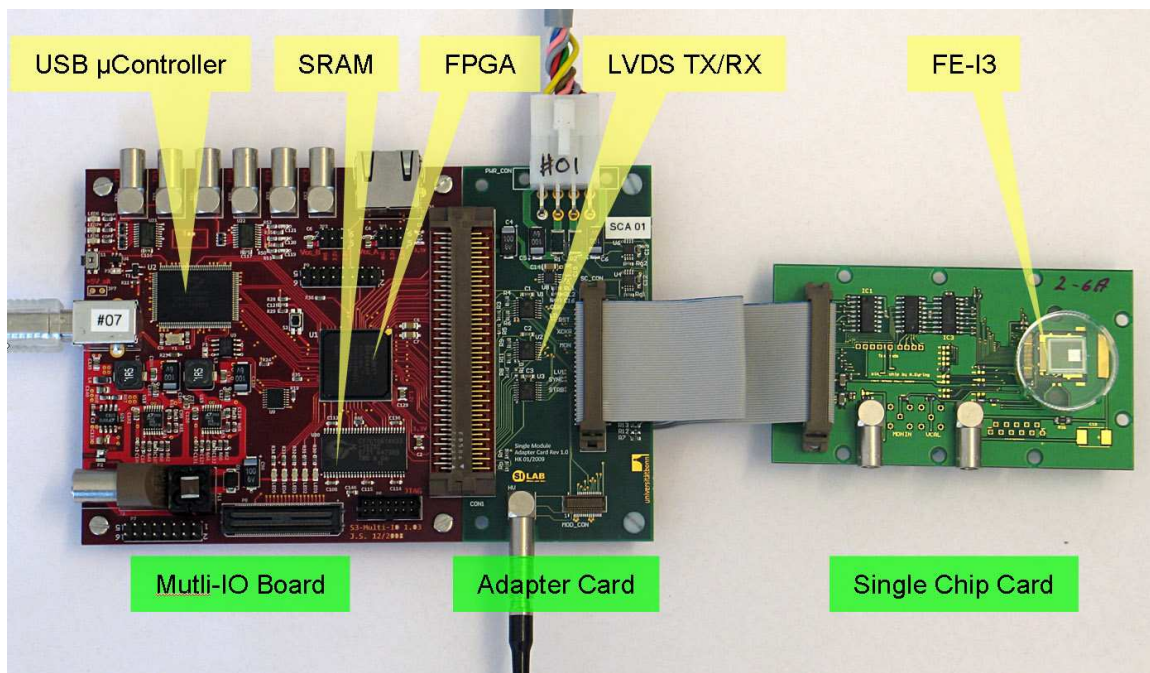
Figure 3.12: Components of the USBPix laboratory test system [27].

The LEMO connectors provide access to different signals. The channel layout of the LEMO connectors is set by the FPGA programming. The connectors are labeled with the names TX0, TX1, TX2, RX0, RX1 and RX2 (figure 3.12 from the left to the right). The connector TX2, for example, is connected to the hitbus signal, whereas the connector RX0 is used as trigger input.

---

[8]Field Programmable Gate Array.
[9]Static Random Access Memory.

FE-I3 Adapter Card

The FE-I3 Adapter Card [28] is connected to the hundred pin connector of the Multi purpose IO-Board. It provides LVDS signal buffers and the digital and analogue supply voltages for the FE-chip.

Single Chip Card

Single chip cards are modules with only one FE-chip and a customized sensor, they do not have an MCC. A single chip card is connected to an adapter card via a flat ribbon cable. The sensor bias voltage is applied to a LEMO connector. The supply voltage for the LVDS drivers of the single chip card can be supplied via a LEMO connector or via the flat ribbon cable. Which connection is used is set with a solder bridge. The physical address of the card can also be set by 4 solder bridges, so addresses between 0 and 15 are possible. There are several pins on the single chip card to pick up different signals like the clock or the analogue and digital supply voltages. The FE-chip is glued on the single chip card and via wire bonds, connected to it. For laboratory tests single chip cards are produced both with and without a sensors.

4 The Laser System

With a laser it is possible to inject charges with high precision into the sensor. The position of the charge injection can be adjusted with an accuracy of less than one micrometer. Furthermore, the area, where the charge is injected, can be measured very precisely, because the diameter of the laser beamspot is well known. The injected charge can be modified easily by variation of the laser pulse intensity. Because of the high laser pulse frequency (up to $1\,\mathrm{MHz}$) it is possible to reach a large number of charge injections in a very short time.

With a laser system it is possible to inject charges in different positions at the sensor. So it is possible to study the effects which appear at the edge of a pixel or at the edge of the whole sensor. With different laser wavelengths it is possible to inject charges only on the surface of the sensor or throughout the whole sensor thickness. Likewise, the time at which the laser pulse is injected can be controlled very precisely. With this, time response studies are possible.

4.1 Charge Injection via Laser Light

For the measurements of this study two lasers were available. One is an infrared laser with a wavelength of $1060\,\mathrm{nm}$, the other is a red laser with a wavelength of $671\,\mathrm{nm}$. The pulse width of the red laser is $31\,\mathrm{ps}$. It has a peak power of $500\,\mathrm{mW}$. The infrared laser has a pulse width of $41\,\mathrm{ps}$ and a peak power of $700\,\mathrm{mW}$.

Most of the particles that are detected by the ATLAS pixel detector are MIPs. By traversing the sensor they produce approximately 20000 electron-hole pairs (see chapter 3.1.1). For the simulation of a MIP that traverses the sensor, the laser pulse energy, which is needed to create such a charge, has to be calculated. The average energy needed to create one electron-hole pair in silicon is $W = 3.62\,\mathrm{eV}$ [20] (see chapter 3.1.1). Thus to create 20000 electron-hole pairs an energy of $E_{20000} = 20000 \cdot W = 63.2\,\mathrm{keV}$ is necessary.

The energy of one laser pulse is $E_{pulse} = Pt$, where t is the puls width and P the peak power of the laser pulse. From the peak power, the corresponding peak energies E_{peak} can be calculated. The red laser's peak energy is $106.1\,\mathrm{MeV}$. For the infrared laser it is $179.1\,\mathrm{MeV}$. It is apparent that for the creation of a charge that corresponds to a MIP the lasers have to be attenuated. The attenuation a that is needed to create 20000 electron-hole pairs is calculated by $a = E_{pulse}/E_{20000} = Pt/E_{20000}$. For the red laser the attenuation was calculated as 1679, for the infrared one as 2834.

The energy of one photon is given by $E_\gamma = h\nu = hc/\lambda$, where λ is the wavelength of the laser. For the red laser it results $E_{\gamma,red}{=}1.85\,\mathrm{eV}$, for the infrared one $E_{\gamma,IR}{=}1.17\,\mathrm{eV}$. With these values the number of photons that are needed to create 20000 electron-hole pairs could be calculate $n_{20000} = E_{20000}/E_\gamma$. It became apparent that with the red laser 34000 photons are needed, with the infrared laser the number of photons has to be 54000. Table 4.1 gives an overview of the calculated values for the red and the infrared laser.

Wavelength,	671 nm	1060 nm
Photon energy, E_γ	1.85 eV	1.17 eV
Laser peakpower, P	500 mW	700 mW
Pulswidth, t	34 ps	41 ps
Nominal pulse energy, E_{pulse}	106.1 MeV	179,1 MeV
Attenuation, a	1679	2834
Number of photons n_γ for a MIP	34162	54017

Table 4.1: Electron-hole pair production with red and infrared laser light in silicon.

The intensity loss of light by traversing matter is calculated by

$$I(x) = I_0 \cdot e^{-\alpha x} \tag{4.1}$$

Here α is the absorption coefficient, and x is the depth of the photon beam in matter. The absorption coefficient is frequency depended. This dependency is shown in Figure 4.1. It is apparent that the absorption coefficient gets smaller for higher frequencies. This results in the fact that the laser with a wavelength of 1060 nm penetrates the sensor more deeply than the laser with a wavelength of 671 nm does. The red laser light enters into silicon approximately 4 µm deep [29], so the charge is only produced at the surface of the sensor. For infrared laser light, at a 250 µm thick silicon layer approximately 55% of the intensity are absorbed. 12% are transmitted and 33% are reflected [30]. This shows that by using the infrared laser the charge production happens throughout the whole sensor.
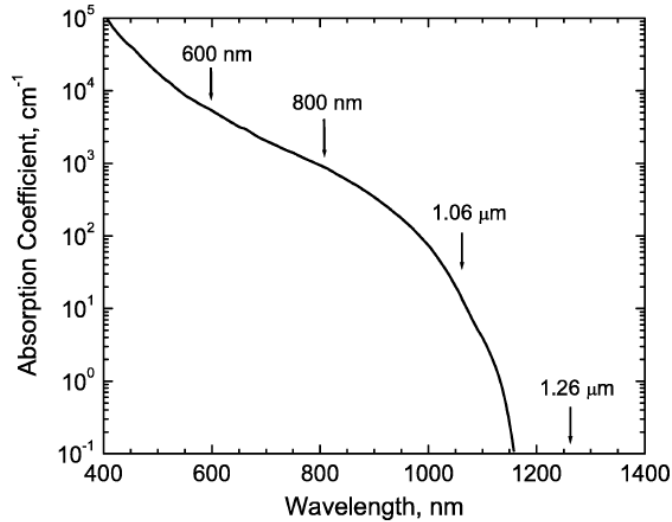
Figure 4.1: Absorption coefficient for silicon as a function of the wavelength [31].

4.2 Setup

The measurement setup has to fulfill different tasks: The laser beam has to be attenuated to adjust the correct laser intensity. It has to be divided to inject charges into the sensor and to

measure the beam intensity at the same time. For the intensity measurement one part of the beam is lead to a photodiode. The other part is lead into a microscope that focuses the beam on the sensor. To focus the beam on a certain point on the sensor, the beam and the sensor had to be observed by a camera.

For the realization of these tasks the set up shown in figure 4.2 was built. The laser and the attenuator are connected with a single-mode optical fiber. Another single-mode optical fiber guides the light from the attenuator to the optical system. Here the beam is focused with a collimator and split by an beam splitter into two parts. One part of the laser beam illuminates a photodiode where the laser intensity is measured. The other part is deflected into the microscope. The microscope focuses the beam on the sensor that is installed in a probe-station. The sensor and the beamspot can be observed with a ccd camera that is located above of the beam splitter.
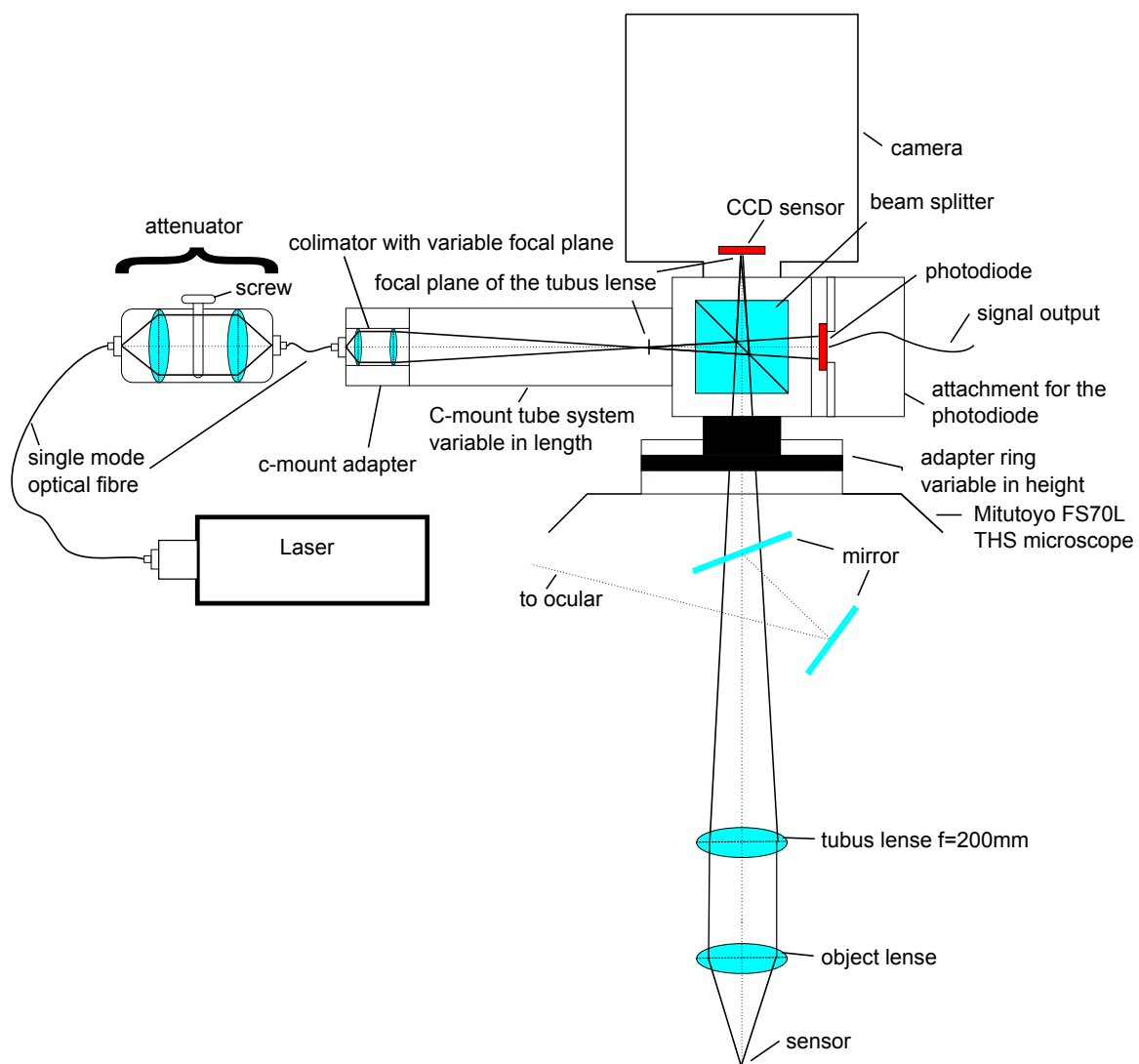
Figure 4.2: Setup of the laser system.

4.2.1 The Laser

As laser system the picoseconds injection laser (PiLas) from Advanced Laser Diode Systems was used. This laser system consists of a control unit and two diode laser heads (671 nm and 1060 nm). Both lasers are class one lasers. All measurements in this thesis were made with the red 671 nm laser.

The laser pulse repetition frequency can be adjusted between 10 Hz and 1 MHz. The laser pulse frequency jitters about 3 - 4 ps [32]. The controller allows manual and external triggering of the laser pulses. If the laser is triggered externally, the jitter of the optical output depends on the slope quality and the noise of the trigger's source [32]. For triggering a TTL[1] signal or a NIM[2] signal can be used. The trigger level can also b adjusted between -5 V and 5 V [32].

As the performance of the laser diode is temperature dependent, the laser system needs 15 minutes warm up time to reach a thermal equilibrium. With a temperature change of 1 K, the time of the laser pulse emission can change by up to 10 ps [32]. The laser intensity can be set by a TUNE value between 1 and 100%.

Laser Pulse Frequency Dependence of the Laser Intensity

The larger the TUNE value is, the larger is the intensity of the laser. A clear Gaussian single form is only generated up to a certain TUNE value [32]. The ideal TUNE value differs for each frequency; varying between 35 and 60%. If the TUNE value stays constant, the pulse intensity differs for different pulse frequencies. The higher the pulse frequency is, the lower is the laser peak power. For all measurements a TUNE value of 50% was chosen, independent on the used pulse frequency. In Table 4.2 the TUNE values for the red laser are shown for different pulse frequencies and a fixed laser peak power.

Frequency	TUNE value	Peak power	Pulse energy	Average Power
1 kHz	37%	230 mW	9 pJ	0.009 μW
10 kHz	42%	230 mW	9 pJ	0.092 μW
100 kHz	50%	230 mW	9 pJ	0.92 μW
200 kHz	51%	230 mW	9 pJ	1.85 μW
500 kHz	52%	230 mW	9 pJ	4.60 μW
1 MHz	52%	230 mW	9 pJ	9.20 μW

Table 4.2: TUNE values for different pulse frequency's and for a fixed laser peak power. Shown are the values for the laser with the wavelength of 671 nm [32].

4.2.2 The Attenuator

The light that is sent out by the laser is coupled into a single mode optical fiber, which is connected to the attenuator. The attenuator lowers the laser intensity by up to 40 dB. It consists of a lens which widens and parallelizes the beam. The attenuation is regulated by a screw that partially blocks the beam. After the attenuation the beam is collimated with another lens. The screw of the attenuator is manually. The attenuator has no influence on the Gaussian laser beam profile [33].

---

[1]Transistor-transistor logic, input voltages under 0.8 V are level 0, above 2 V are level 1.

[2]Nuclear instrumentation standard, input voltages above 0 V are level 0, under -0.6 V are level 1.

4.2.3 Optical System

For the focusing and splitting of the laser beam a system consisting of various optical components was used. To focus the beam on the sensor and to minimize the beamspot diameter, these optical components had to be adjusted.

Laser Collimator

The single mode optical fiber coming from the attenuator is connected to a laser collimator. This collimator is used for the focusing and collimation of the laser beam. The diameter of the beamspot depends on the adjustment of the laser collimator. The smallest beamspot is obtained if the focal plane of the collimator is the same as the focal plane of the microscope's lens tube (see figure 4.2).
The adjustment of the collimator is done via a little screw on top of the collimator. Subsequently, the focal plane is changed by rotating the screw until the beamspot is minimal. This calibration has to be redone when a different laser is used. The position of the focal plane of the lens tube depends on the reflection index of the lens tube which in turn is wavelength dependent.

C-Mount System

To connect the collimator with the beam splitter a c-mount[3] system from "Linos" was used. The focal plane of the lens tube is 17.5 mm in front of the beam splitter. The focal length of the collimator has to be in the same order as the focal length of the tube lens. If the focal length of the collimator is too short, the laser beam is fanned out too much and it is reflected at the microscope walls. If the focal length is too long, the beam is very small and the objective lens is not fully illuminated. As distance between the focal plane of the tube lens and the collimator the focal length of the tube lens, which is 200 mm, was chosen. Thus the c-mount structure between the collimator and the beam splitter had to have a length of 217 mm.
For its adjustment the c-mount system can be extended or shortened by screwing two parts of the system into each other.

Beam Splitter

The beam splitter is the part which connects the microscope, the camera, the photodiode and the collimator via c-mount connections. It splits the incoming beam into two parts. One part goes through the cube and the other part is deflected by 90°. In this process the beam is split in the ratio of one to one. The transmitted part of the laser beam is guided to the photodiode, where the laser intensity is measured. The reflected part is sent through an adapter ring into the microscope.
The laser beam has to be redirected in such way that it is parallel to the optical axis of the microscope. This could be accomplished by changing the angle between the beam splitter and the optical axis of the microscope. Only if this angle is set very precisely, is the laser beamspot in the middle of the observed picture. If this angle is set up badly, the laser beam would not reach the objective lens. The angel of the beam splitter can be adjusted with six little screws on the support structure of the beam splitter.

---

[3]The c-mount standard defines the parameters of the threads of optical components.

Camera

The pictures viewed by the microscope are monitored with a Sony CCD black and white video camera module XC-ST50 CE. This camera has a c-mount connection so that it can be installed easily on the beam splitter. The resolution of the camera is 768×494 pixels [34]. The camera is sensitive in infrared and visible wavelengths. In this way also the infrared laser beamspot can be observed.

Camera Adapter Ring

The camera adapter ring is located between the beam splitter and the camera input of the microscope. It is variable in height. With this ring the sensor of the ccd camera can be brought into the focal plane of the tube lens. If the camera is not in the focal plane of the tube lens, it becomes necessary to refocus the microscope when switching between observation by camera and by ocular. For the adjustment of the focal plane, the adapter is adjustable about 10 mm in height.

The Microscope

For observing and focusing the beamspot on the sensor a Mitutoyo FS70L THS microscope is used. The microscope is equipped with 4 different objectives with magnifications of $2\times$, $10\times$, $20\times$ and $50\times$. Moreover, a connection for the installation of a camera is available. Here the beam splitter is installed. For observation, the light can be switched between the ocular and the camera output. Having a picture on both outputs at the same time is not possible. The focal plane of the tube lens is 79.6 mm above the camera output.
The microscope is mounted on the probe-station. It can be moved in all three directions. In x and y direction the resolution is $0.25\,\mu\text{m}$, in z direction $0.1\,\mu\text{m}$ [35].
The $20\times$ and $50\times$ objectives generate beamspots that are small enough to inject charges only in one pixel (see chapter 4.4.2). Because of problems with the installation of the $50\times$ objective only the $20\times$ objective was used for the measurements.

4.2.4 The Probe-Station

The probe-station PA300 from Süss MicroTec consists of a chuck that can be cooled and a case around this chuck. The microscope is installed on top of this case. It can be lifted, so that it is possible to install hardware under the microscope. There are also other covers for the installation of hardware. The chuck could be driven in all three directions. In x and y direction the precision of the chuck is $0.5\,\mu\text{m}$, in z direction it is $0.25\,\mu\text{m}$ [35]. The chuck temperature can be adjusted between -55°C and 160°C. The accuracy of the set temperature is 0.5°C [36]. It is possible to flush the case with dry air, so condensation can be prevented. A safety interlock system was installed at the probe-station. This interlock ensures that people cannot come in contact with the laser beam.

Safety Interlock System

The whole system, from the laser collimator via the microscope through to the chuck, is light proof. So the user cannot get in contact with laser light. To ensure that the laser cannot be switched on while the microscope is lifted or while one of the covers is opened, an interlock system was installed. The interlock consists of different switches that are connected in series. If one of these switches is opened, the power connection of the laser control unit is interrupted.

The microscopes light path can be switched between the camera and the ocular by hand. This toggles a switch, which is closed when the light path is conducted to the camera position. Otherwise, if the light path is conducted to the ocular position, the switch is opened. So it is guarantied that it is not possible to look through the ocular into the laser beam. In this interlock circuit an additional hand switch is installed. It is used as remote control for the laser.

Temperature Monitoring

For the installation of a single chip card and to ensure good thermal contact between the sensor and the chuck a fixing structure was constructed. For temperature monitoring a negative temperature coefficient resistor (NTC)[4] is installed within this structure. In this way the temperature very close to the sensor can be measured. The NTC is read out by a digital multimeter. At the nominal temperature $T_0 = 25°C$ the NTC has a resistance of $R_0 = 2\,k\Omega$. The temperature range of the NTC extends from -60°C to +150°C. The tolerance is 0.5% and the characteristical B-value is 3976 K [37]. The temperature T can be calculated by measuring the resistance R:

$$T = \frac{B \cdot T_0}{B + ln\left(\frac{R}{R_0}\right) \cdot T_0}$$ (4.2)

4.2.5 The Photodiode

The photodiode is installed on the beam splitter. It measures the laser intensity of the transmitted part of the beam. The output voltage of the photodiode is linearly dependent on the laser intensity [38]. So the relation between the photovoltage and the laser intensity under the microscope can be calibrated easily. Thus it is possible to set up the right laser intensity at the attenuator.

For the measurement of the laser intensity a S9269 silicon photodiode with amplifier from Hamamatzu was used. This diode has an active area of $5.8 \times 5.8\,mm^2$. It is sensitive to visible and near infrared light. For a wavelength of 671 nm the photosensitivity is about $0.43\,\frac{V}{nW}$. For a wavelength of 1060 nm it is about $0.20\,\frac{V}{nW}$ [38].

The preamplifier of the diode needs a supply voltage of $U^{\pm} = \pm 15\,V$. The signal output of the diode is connected to an Agilent 34410A Digital Multimeter, which measures the output voltage of the diode. There is a strong laser pulse frequency dependence of the output voltage. This dependency is due to three reasons: First of all, the response of the photodiode changes by varying the frequency of the incoming light (see above). Secondly, the laser intensity itself is frequency dependent (see chapter 4.2.1). And finally, the photodiode measures the average intensity of the laser beam and not the pulse intensity. The average intensity depends on the laser pulse frequency, so if the pulse frequency is lowered by about a factor of 10, the photovoltage will also be lowered about a factor of 10.

Because of this frequency dependency it is difficult to do measurements at low laser pulse frequencies, because in that case the output voltage of the photodiode gets too low.

The output voltage of the photodiode ranges between 0 and 15 V. Photovoltages down to 1 mV can be measured reliably.

---

[4]NTC-Temp-Sensor TS-NTC-202-60/+150°C.

4.3 Calibration

For the calibration of the correlation between the photovoltage and the charge that is injected into the sensor the unirradiated sensor 11-5B was used. The threshold was tuned to 3200 electrons and for each measurement 50000 laser pulses were injected into the sensor. For the calibration, the TOT response was measured for several laser intensities, which were chosen in such a way that the whole voltage range of the photodiode (1 mV to 15 V) was covered. From the TOT values the corresponding charges could be calculated and the charge-photovoltage calibration could be done. Because of the laser pulse frequency dependency of the photovoltage, this calibration had to be done separately for each pulse frequency. The different object lenses have different reflection indexes, so the calibration had to be done, for each objective. The calibration shown here was done with the 20× objective.

For all calibration measurements the laser beam was focused on the pixel with the column number 9 and the row number 13 (pixel 9/13). For small charges (up to approximately 50000 electrons) the beamspot was smaller than 50 μm and only the targeted pixel showed hits. For larger charges also the neighbor pixels showed hits. For the calibration measurement all pixels were disabled, except for a small cluster around that pixel in which the charge was injected. So the noise could be minimized.

The photodiode calibration was split into two parts. The first part was the TOT-charge calibration of the FE-I3 readout chip. In this process the charge values were calculated from the TOT values. The second part was the photovoltage calibration itself. In this process the photovoltage was measured with the multimeter and the TOT was measured with the silicon sensor. With the TOT-charge calibration and the photovoltage-TOT calibration the relation between the photovoltage and the injected charge could be calibrated.

4.3.1 TOT-Charge Calibration

For the TOT-charge calibration a TOT-Calib scan was done. Well known charges were injected 50 times into each pixel and the TOT response was measured. This measurement was done with 54 different injection charges for each capacitor. The TOT-charge calibration was done separately for each pixel.

To inject a charge into a pixel, a capacitor (C_{low} or C_{high}) was charged by a voltage pulse. The height of this voltage pulse was calculated by multiplying the $V_{cal} - DAC$ with the voltage difference ΔV between two $V_{cal} - DAC$ values[5].

$$U = V_{cal} \cdot \Delta V \tag{4.3}$$

The injected charge is calculated by $Q = C \cdot U$. For each module an average capacitance was measured at the module assembly. These capacities were not very precise and by calculating the charges from the V_{cal} values a step was seen between the curves of the two capacities (see figure 4.3). To improve the calibration the capacities C_{low} and C_{high} were calculated separately for every pixel.

The capacities were measured with the help of a source scan. In this process the sensor was irradiated by an Americium 241 source and the TOT response was measured. The TOT spectra were plotted separately for each pixel and the peak was fitted with a Gaussian (see figure 4.4). The energy of the peak position of the Gaussian is well known. For Americium 241 it is 59.5 keV. The corresponding charge could be calculated by dividing the peak energy by the average energy

---

[5]ΔV was taken as equal for the whole module. It was measured on the assembly.
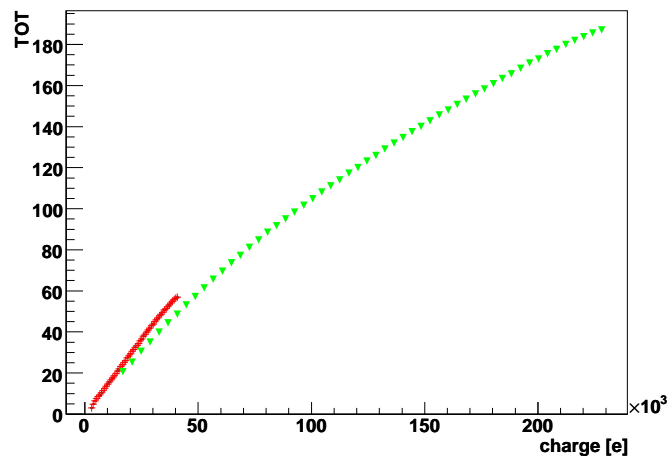
Figure 4.3: TOT-charge calibration curves for pixel 9/13 with the average capacities from the module testing procedure. Red crosses: C_{low}; green triangles: C_{high}. The TOT errors are too small to be seen.
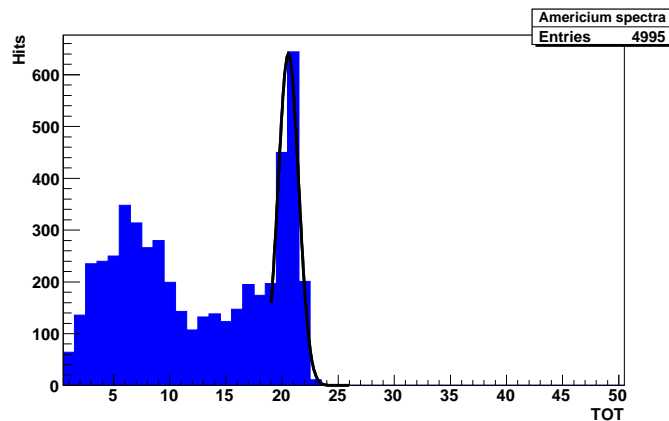
Figure 4.4: Americium 241 spectrum for pixel 9/13 with a Gaussian fit. The peak at lower TOTs comes from the 14 keV line of the americium spectrum.

that is needed to produce an electron-hole pair in silicon (see chapter 4.1). An energy of 59.5 keV corresponds a charge of 16436 electrons.

In the next step, the measured TOT was plotted as a function of the V_{cal} values. This was done for both capacities. Then these values were fitted with a ninth order polynomial function (figure 4.5). This fit was chosen, because it shows better results than the official ATLAS fit function [39]. With these fits the V_{cal} value could be calculated, which corresponds to the TOT value of the peak position of the Americium source scan ($V_{cal,Am}$). For pixel 9/13 the $V_{cal,Am}$ values were 330.04 ± 0.04 for C_{low} and 72.02 ± 0.03 for C_{high}.

With these values, the voltages $U = V_{cal,Am} \cdot \Delta V$ needed to inject a charge corresponding to the peak position of the Americium source, could be calculated. Thus the size of the capacitors could be calculated: $C = Q/U$. For the pixel 9/13 the capacities were $C_{low} = 7.97 \pm 0.01$ fC and $C_{high} = 36.56 \pm 0.04$ fC. These values differ significantly from the average measured capacities of $C_{low} = 7.3$ fC and $C_{high} = 40.808$ fC.
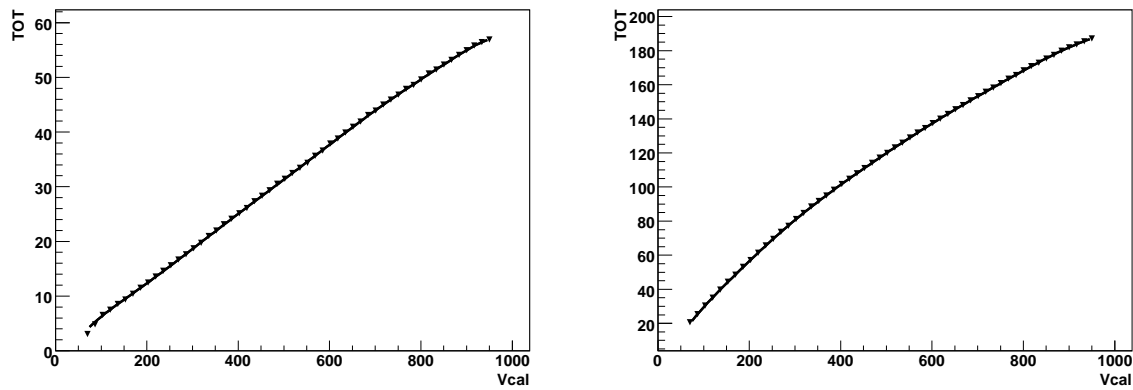
Figure 4.5: Measured TOT values for pixel 9/13 as a function of the V_{cal} values fitted with a ninth order polynomial; left: C_{low}; right: C_{high}. The TOT errors are too small to be seen.

With the new capacities the V_{cal} values from the measurement could be transformed into charges: $Q = C \cdot V_{cal} \cdot \Delta V$. The measured TOT values were plotted as a function of the corrected injected charges (figure 4.6). The TOT errors result from the widths of the TOT distributions, that where measured at the TOT-calib scan. The shown charge errors result from the capacity errors. The errors in figure 4.6 are to small to be seen. The TOT-charge dependence was fitted with a ninth order polynomial fit.
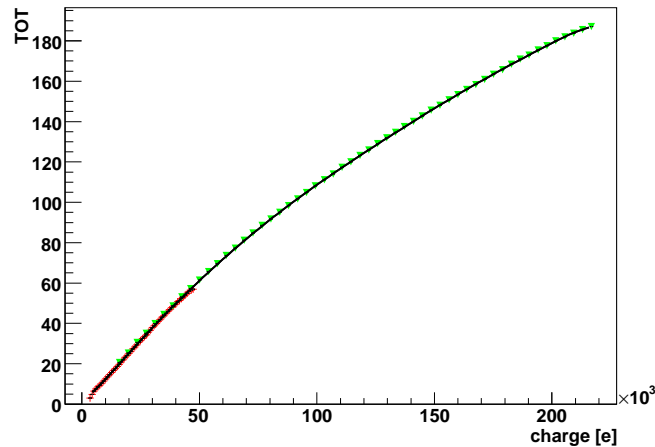
Figure 4.6: Calibration curve and ninth order polynomial fit for the pixel 9/13. The data from the C_{low} calibration is shown with the red crosses, that from the C_{high} calibration with the green triangles. The error bars are too small to be seen.

To show the quality of the fit, the charge residuals were plotted as a function of the TOT values. Charge residuals were defined as the difference between the injected charge and the measured charge. Figure 4.7 shows the charge residuals for the pixel 9/13. The TOT errors are again the widths of the TOT distributions. The residual errors result from the quadratical addition of the fit errors and the errors that results from the capacity errors. The small charge

residuals show that the applied polynomial fit yields good results for the charge calibration. Figure 4.7 still shows a little offset between the C_{low} and the C_{high} calibration. Reasons for this offset can be a yet too imprecise calculation of the capacitances or the assumption that the ΔV steps have always the same range.
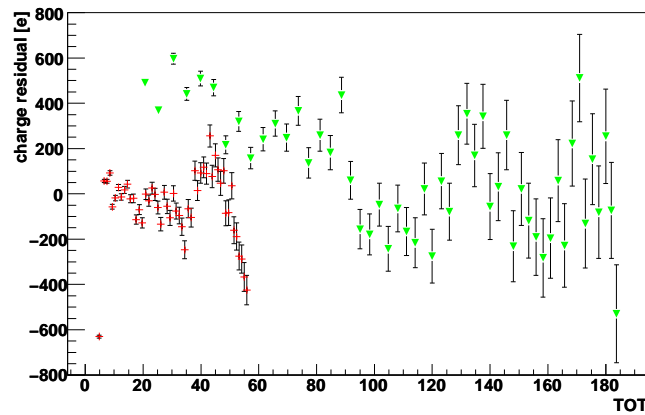
Figure 4.7: Charge residuals for pixel 9/13. The data from the C_{low} calibration is shown with the red crosses, that from the C_{high} calibration with the green triangles.

TOT values are digital integers. Therefore the charges had to be calculated which belong to integer TOT values. For the calculation of these charges a look up table was created. The look up table calculates a TOT value for every charge between 1 and 210000 electrons. Then the charges which correspond to the integer TOT values were plotted as a function of those. Such a plot is shown in figure 4.8. The charge errors result from the errors of the polynomial fit are to small to be seen in.

Because of the integer TOT values a number of charges is collected into one TOT bin. These binwidths are shown in figure 4.9. The binwidth errors are resulting in the fit errors. The binwidth is taken as systematical error of the TOT-charge calibration.
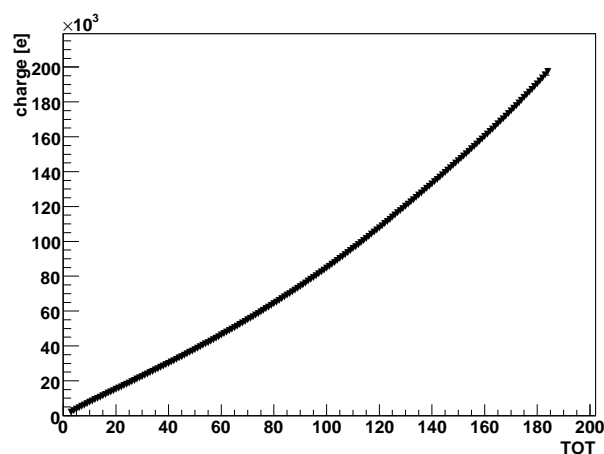
Figure 4.8: Charge values for integer TOT values for pixel 9/13. The charge errors are too small to be seen.
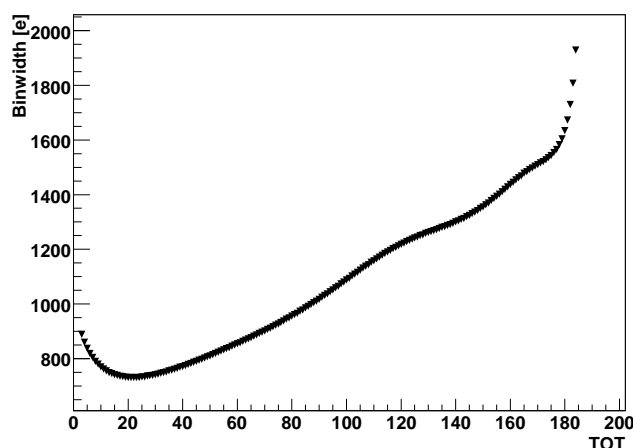
Figure 4.9: Binwidths for integer TOT values and pixel 9/13.

4.3.2 Photodiode Calibration

For the photodiode calibration different laser intensities were chosen in such a way that the whole dynamic range of the photodiode was covered. The photovoltage and the corresponding TOT spectra were measured. With the help of the TOT-charge calibration the TOT spectra could be transformed into charge spectra. One of these charge spectra is shown in figure 4.10. Now the measured photovoltages were plotted as a function of the mean values of the charge spectra. Figure 4.11 shows the charge-photovoltage calibration for a laser pulse frequency of 20 kHz. For the determination of the charge errors, the mean value of the measured charges and its error were calculated. For this calculation also the binwidth errors were taken into account. As photovoltage errors the measurement errors are shown. Figure 4.11 shows a linear dependency between the photovoltage and the laser intensity. This relation between the photovoltage and the injection charge is laser pulse frequency dependent. The resulting calibrations are discussed in chapter 4.4.1.
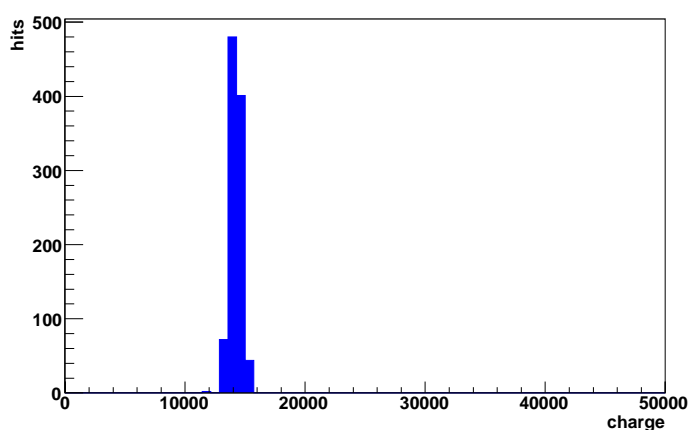
Figure 4.10: Charge spectrum for a frequency of 20 kHz and a laser intensity that corresponds a photovoltage of 200 mV, measured with pixel 9/13.
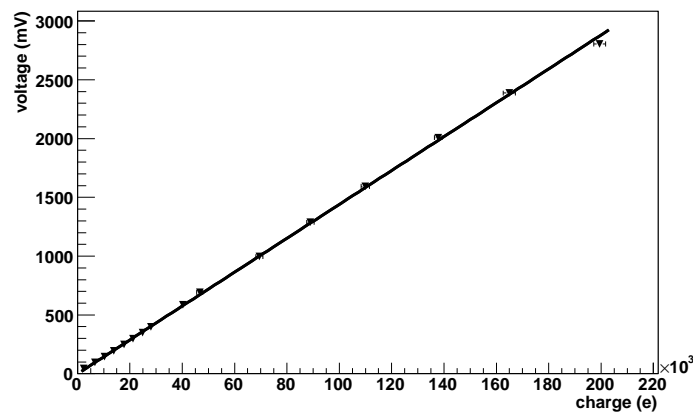
Figure 4.11: Dependency between photovoltage and injected charge for 20kHz laser pulse frequency with a linear fit.

4.3.3 Crosscheck with Radioactive Sources

For a crosscheck of the TOT-charge calibration the sensor was irradiated with three different γ-sources. The peak values of the γ-spectra are well known. If the peak energy of the source is divided by the average energy needed to produce an electron-hole pair in silicon ($3.62\,\text{eV}$), the charge that is produced in the sensor can be calculated (see chapter 4.1).

For the crosscheck Americium 241, Cadmium 109 and Cobalt 57 were used. For all three sources a source-measurement was made with sensor 11-5B. The charge spectra were done separately for every pixel. Figure 4.12 shows the measured charge spectrum of Cadmium 109 and pixel 9/13 with a Gaussian fit. The hits at very low charges are noise hits, that lay very close to the threshold.

Table 4.3 shows the peak energy E_p of the sources and the number of theoretically produced electrons n_e. In the last column the peak value of the measured spectrum is shown. As error the RMS is shown.
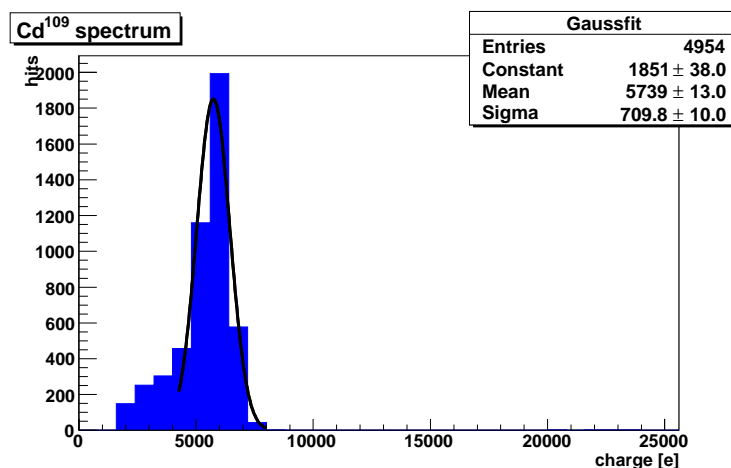
Figure 4.12: Charge spectrum for pixel 9/13, done with a Cadmium 109 source and fitted with a Gaussian.

| Source | Literature value | | measurement |
	E_p [keV]	n_e [e]	peak charge [e]
Cd^{109}	22.9	6326	5739 ± 710
Am^{241}	59.5	16436	15390 ± 643
Co^{59}	122	33702	30700 ± 855

Table 4.3: Measured peak energies and the corresponding literature values for Cadmium 109[40], Americium 241[41] and Cobalt 57[41].

For small charges, as they were injected with the Cadmium source, the TOT calibration works well. In the range of the error the measured source peak is at the expected position. For higher energies the calibration becomes worse. For Americium the measured charge is approximately 1100 electrons smaller than the theoretical value. For Cobalt the difference is approximately 3000 electrons.

A possible explanation is, that for high injection charges C_{high} injects too little charge into the sensor. This could be, because the voltage pulse which charges the capacitor could be to short to load the capacitor until it is fully charged. So the injected charge could be too low and the calibration fit becomes too flat.

4.4 Characterization of the System

The laser system can be used in different settings. Two lasers, of 671 nm and 1060 nm wavelength, are available. There are two possible objective lenses, 20× and 50×, which results in beamspot diameters smaller than the size of a pixel. The TUNE value can be varied between 1 and 100%, and frequencies between 10 Hz and 1 MHz are possible. For every one of these settings the calibration from chapter 4.3 would have to be redone.

Tests showed, that the following settings were suitable for dynamic efficiency measurements. The red 671 nm laser was used, in combination with the 20× objective. The 50× objective was because of installation problems not available. The TUNE value was fixed at 50%. To work out which laser pulse frequencies submit a wide range of available charges, the calibration was done for several laser pulse frequencies.

4.4.1 Laser Pulse Frequency Dependency

There is a strong laser pulse frequency dependency of the photovoltage (chapter 4.2.5). To gain a wide range of injection charges the used pulse frequency had to be chosen such that for high injection charges the photovoltage does not exceed its maximal output voltage of 15 V. On the other hand the photovoltage should not get too low for small charges. The laser pulse frequency should also be high enough to generate a large number of pulses in a short times.

If the laser pulse frequency is chosen too low, small charges (charges near the threshold) cannot be measured, because the photovoltage does not exceed the noise level. Here also the output voltage for the maximum laser intensity stays very small. Because of that behaviour, useful measurements could be done down to a pulse frequency of 1 kHz.

If the laser pulse frequency is too high, the maximum photovoltage of 15 V is exceeded for higher charges. For a frequency of 1 MHz this happens at a charge of 20000 electrons

In the middle of the laser pulse frequency range the measurable charge range is only limited by the TOT-charge calibration. Therefore charges of more than 200000 electrons can be measured. For

very low charges the photovoltage stays well above noise level.

Figure 4.13 shows the measurable charge range for laser frequencies between 1 kHz and 1 MHz. One can see that at high frequencies the maximal photovoltage is reached very early. It can also be seen that at low frequencies the photovoltage stays very small.

20 kHz and 200 kHz were chosen as useful laser pulse frequencies. At these pulse frequencies a wide charge range can be covered and they are high enough to get a large number of laser pulses in short time. For these laser pulse frequencies the calibration was redone with the same module configuration as was used for the measurements in chapter 6. The results of this calibration are shown in figure 4.14. The errors were calculated as described in chapter 4.3.2. With the shown linear fits the photovoltage that corresponds to a certain charge can be calculated by:

$$U_{photo,20kHz} \left[mV\right] = (0.0144 \pm 0.0001) \cdot Q \left[e^-\right] - (0.5 \pm 3.3) \tag{4.4}$$

$$U_{photo,200kHz} \left[mV\right] = (0.187 \pm 0.002) \cdot Q \left[e^-\right] - (573 \pm 55) \tag{4.5}$$

4.4.2 Beamspot Diameter

To inject charges only into one particular pixel, the beamspot has to be smaller than the short edge of a pixel. To secure that the diameter of the beamspot has to be measured. Three possible methods to measure the beamspot diameter are shown. In the case of the fist method the diameter is measured by using the camera and a sharp edge. The second and the third method use the ATLAS Pixel sensor in combination with a TOT measurement.

The beam has a Gaussian profile, and the beam quality factor[6] $M^2 = 1$. This means that the beam is a pure Gaussian beam with the minimal possible divergence [33].

Beamspot Diameter Measurement by Using the Camera

In the case of this kind of beamspot diameter measurement a sharp edge is used to have a fixed point under the microscope. The beamspot is observed with the camera. Then the chuck is moved in such way that the right end of the beamspot touches the edge. This chuck position is noted. Afterwards, the chuck is moved until the left end of the beamspot touches the edge. The difference between the two positions is the beamspot diameter.

The camera registers light only if its intensity is above a certain threshold. This causes the problem that the outer parts of the Gaussian beam profile, where the intensity is too low, are not shown by the camera. Because of this behaviour the beamspot diameter, which is observed with the camera, changes by varying the laser intensity.

Beamspot Diameter Measurement by Using the Sensor

Both of the other methods for measuring the beamspot diameter use the ATLAS Pixel sensor. For these measurements all pixels of the sensor except one are disabled. Then the beamspot is moved across the short edge of the not disabled pixel in 1 μm steps.

As soon as a part of the beamspot reaches the pixel, charge is created inside this pixel and a hit is shown[7]. The more of the beamspot covers the pixel, the more charge is produced and

---

[6]$M^2 = 1$ means that only the base mode of the Gauss beam is transmitted. This mode has the smallest divergence. For $M^2 > 1$ higher modes are also transmitted and the divergence of the beam is larger [42].

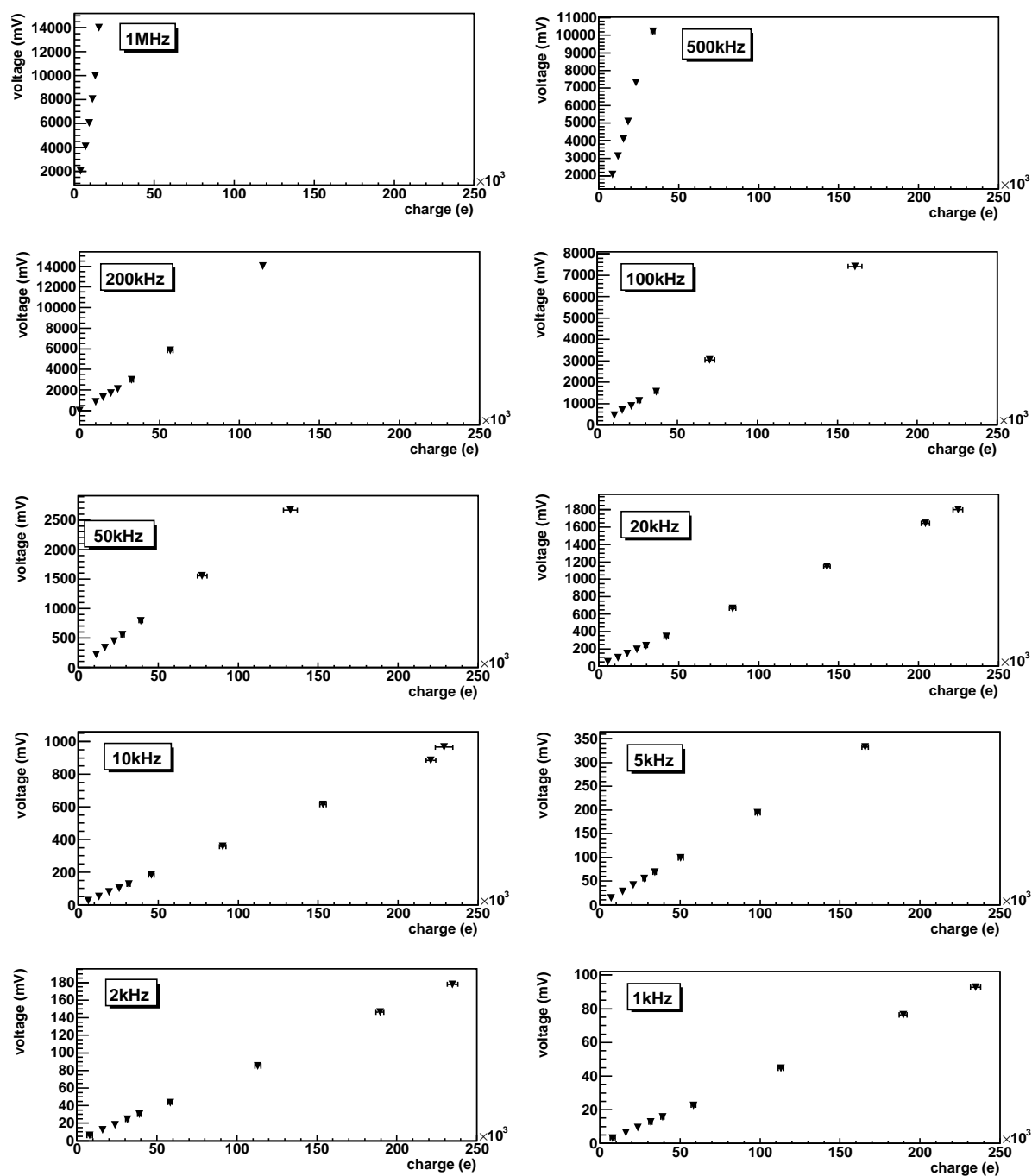[7]When the charge is high enough to exceed the threshold.

Figure 4.13: Photovoltage as a function of the injected charge for laser pulse frequencies between 1 MHz and 1 kHz. Note the different voltage scales.
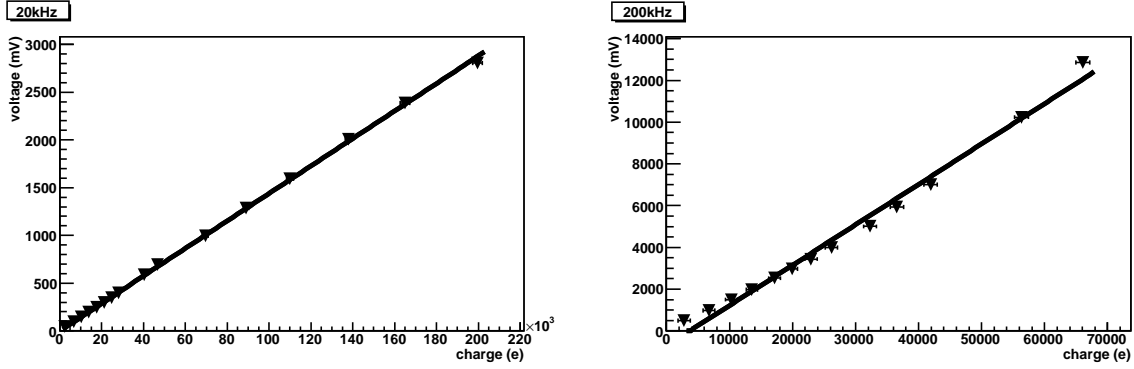
Figure 4.14: Photovoltage-charge calibration with a linear fit for left: 20 kHz and right: 200 kHz.

the TOT rises. The TOT only stops rising when the whole pixel is illuminated with the same intensity. If the beamspot is smaller than a pixel, this is the case when the whole beamspot is above the pixel[8]. In that case a plateau is reached. If the beamspot reaches the other edge of the pixel, the TOT response of the pixel decreases again until the whole beamspot has left the pixel.

For the first method the position (A), where the pixel shows a hit for the first time, is located. Then the laser beam is moved to the other edge of the pixel, and the position (B) is located, where for the last time a hit is observed.
So the beamspot diameter (d) is given by the difference between the first position (A) and the second position (B), minus the diameter of the pixel (D).

$$d = B - A - D \tag{4.6}$$

This method offers the problem that the hit detection efficiency is not equal to one over the whole pixel width and zero outside. Instead, the hit detection efficiency starts rising before the pixel is reached and ends decreasing just after the pixel is left. To calculate the beamspot diameter from the points A and B therefore, not the pixel diameter (D) but the distance (H) between the starting point and the end point of the hit efficiency distribution have to be known. So equation 4.6 can only be used to calculate the beamspot diameter, when the pixel diameter D is replaced by H. Another problem of this measurement is that at a lower threshold the hits are detected farther outside the pixel region than at a higher threshold. Because of the apparent threshold dependency of the beamspot diameter and the missing knowledge of the hit efficiency distribution for an unirradiated sensor this method was not used.

For the second method to measure the beamspot diameter with the sensor only one edge (A) of the pixel and the position (P), where the plateau is reached is used. In an ideal world, the TOT starts rising at the edge of the pixel A and reaches the plateau P, when the whole beamspot is above the pixel (if the beamspot is smaller than the pixel). On the plateau the whole charge created by the laser is injected into the pixel. So the beamspot diameter can be calculated by

$$d = P - A \tag{4.7}$$

---

[8]Only for an "ideal" pixel.
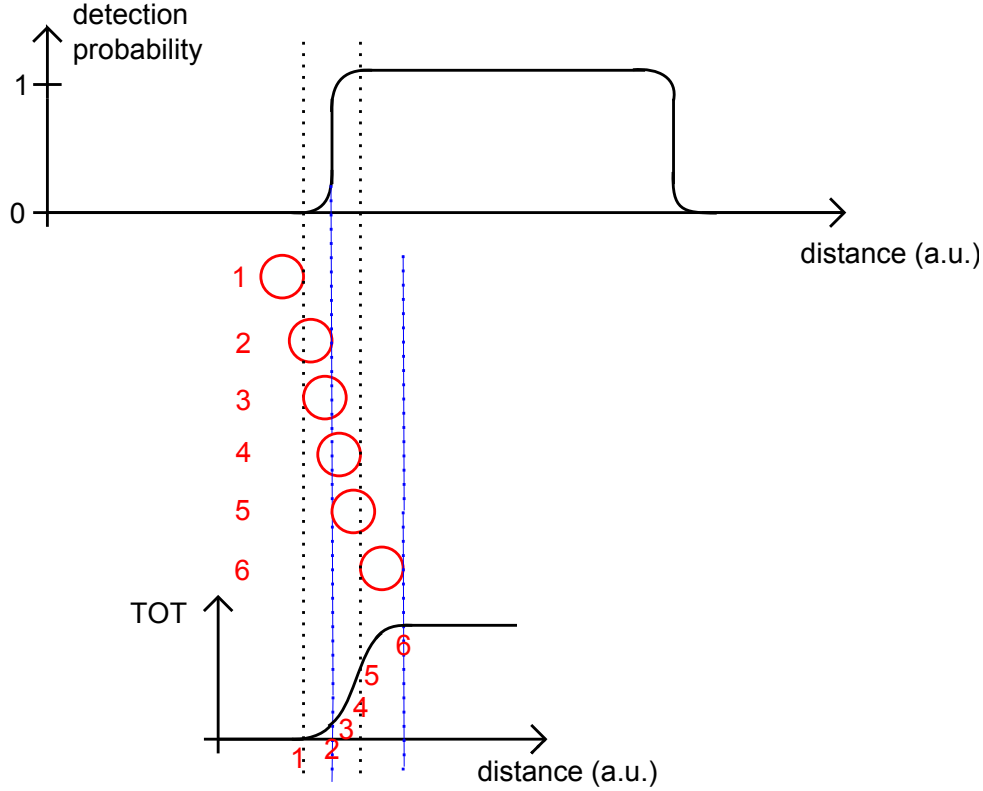
Figure 4.15: TOT-distance behaviour by passing the edge of a pixel, the beamspot is represented as red circle.

Similar to the hit efficiency, the value of the charge collection efficiency is not one over the whole pixel width and zero outside. This increases the distance between the position A and the plateau P. Figure 4.15 shows the behaviour by passing an edge of the pixel, while figure 4.16 shows the charge collection efficiency of "normal" pixels of an unirradiated sensor, measured at a test beam.

The TOT-distance relation, which is measured by passing the pixel, is created by a convolution of the charge collection efficiency with the Gaussian laser beam profile. The standard deviation for a convolution of two normal distributed measurements is given by

$$\sigma_{measured} = \sqrt{\sigma_{beamspot}^2 + \sigma_{efficiency}^2} \tag{4.8}$$

This equation can be solved for the standard deviation of the Gaussian beam profile:

$$\sigma_{beamspot} = \sqrt{\sigma_{measurement}^2 - \sigma_{efficiency}^2} \tag{4.9}$$

The standard deviation $\sigma_{beamspot}$ of the Gaussian defines the diameter of the beamspot.

Figure 4.17 shows two measurements of the sensors TOT response as a function of the distance. The measurements are done for injection charges of 10000 and 20000 electrons. As TOT errors the RMS of the measured TOT distributions is used[9]. The distance errors comes from the spatial resolution of the chuck of the probe station, which is 0.5 µm. The trends are fitted with an error

---

[9]The errors are too small to be seen in figure 4.17.
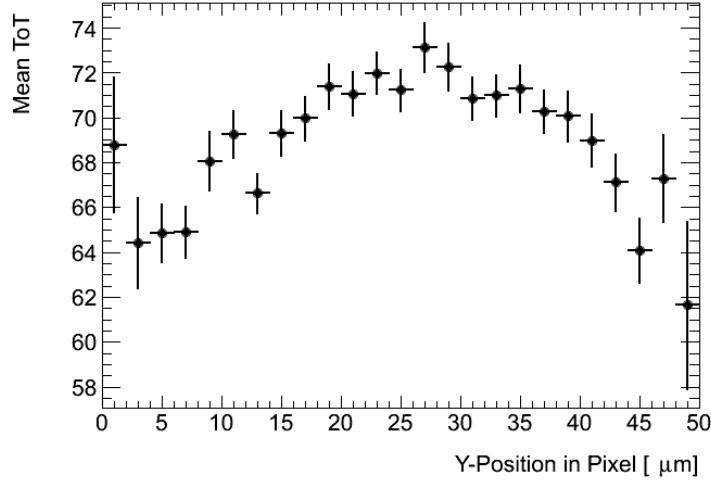
Figure 4.16: Charge collection efficiency: On the x-axis the position in short pixel direction is shown. On the y-axis the measured TOT is shown. This data was taken during test beam measurements at the SPS [43].
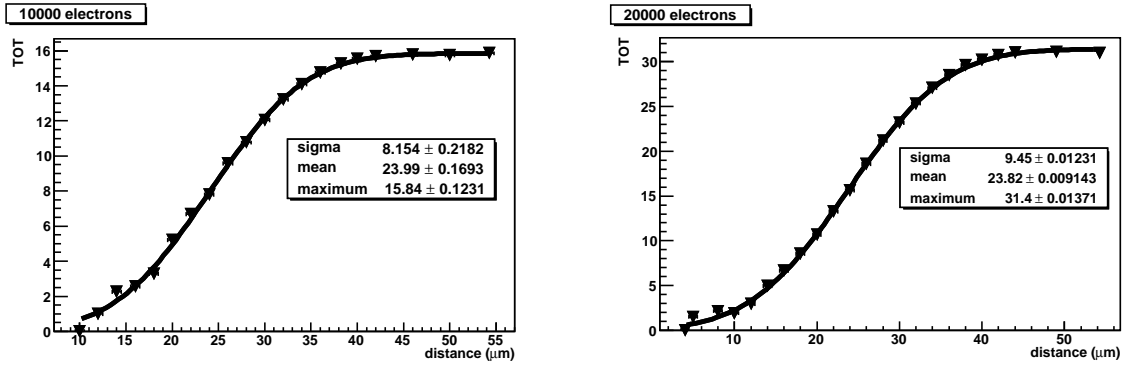
Figure 4.17: Measured TOT passing over the edge of a pixel for 10000 and 20000 electrons injected charge.

function. Due to this fit the standard deviation of the convoluted function is known. With the help of the standard deviation of the charge collection efficiency the standard deviation of the Gaussian beam profile can be calculated.

It was not possible to fit the charge collection efficiency plot with an error function. For an exemplary calculation of the beamspot diameter with this method, it was tried to estimate the standard deviation of the charge collection efficiency. The plateau of the distribution starts at a y-position of approximately $18\,\mu$m and the inflection point is at 9 or $10\,\mu$m, so the standard deviation of the charge collection efficiency is assumed to be $\approx 8\,\mu$m. An estimation of the error is not done, so the further calculations are done without error consideration. The following calculation is not convenient to calculate a beamspot diameter, it only shows the introduced method.

With this estimate on the charge collection efficiency the standard deviation for an injected charge of 10000 electrons is calculated as $\sigma_{beamspot} \approx 2\,\mu$m. For 20000 electrons it is calculated as $\sigma_{beamspot} \approx 5\,\mu$m.

The calculation of a beamspot diameter in μm is difficult, because its value always depends on a free parameter. Using the camera method this is the laser intensity, using the sensor method it is the threshold of the pixel. It is useful to define the beamspot diameter as that part of the Gaussian beam profile, which is above the threshold that is used for the measurements in this thesis. The used threshold of 3200 electrons corresponds an TOT of 4.28 bunchcrossings. With this value, with the standard deviation from the measurement and with the standard deviation from the charge collection efficiency the beamspot diameter for a threshold of 3200 electrons can be calculated. For 10000 electrons charge, the beamspot diameter is calculated as $\approx 10\,\mu$m. For 20000 electrons charge, the value is $\approx 30\,\mu$m.

These beamspot diameter can be compared to the beamspot diameters that is measured with the camera method. In this case the beamspot diameter for an injection charge of 10000 electrons was identified as $7\,\mu$m, for 20000 electrons as $9\,\mu$m. One can see that those beamspot diameters are smaller than these measured with the sensor method. Because of the missing charge efficiency fits, the results from the sensor measurement are only estimations for the size of the beamspot diameter. Nevertheless, in both measurements the beamspot diameter for an injection charge of 20000 electrons is larger than that for 100000 electrons injection charge. So one result of this measurement is that the size of the beamspot is smaller than a pixel and charge depended.

For the measurements in this thesis the beamspot diameters are controlled by using the camera method, because this method is quick enough to do it before every measurement. Additionally, it is ensured before every measurement that the beamspot is in the middle of a pixel, and that only one pixel shows hits.

If the slope of the charge collection efficiency is known, it is possible to do precise beamspot diameter measurements and to calculate the standard deviation of the Gaussian laser beam profile. With the data which was available for this thesis, however, this is not the case, so the method can only be shown theoretically.

The camera method is a good method to get a quick impression of the beamspot diameter. For a more precise measurement other methods, like laser power measurements that support spatial information, have to be used, though.

5 Sample Characterisation

The measurements in this thesis were done with two different silicon sensors. The first one was unirradiated and its reactions were known very well. The second sensor was irradiated with thermal neutrons up to a dose of $1 \cdot 10^{15} \mathrm{cm}^{-2}$ neutron equivalent. That conforms the ATLAS lifetime dose.

For both samples the same tuning and characterization procedure was used. The samples were tuned to a threshold of 3200 electrons and the TOT was tuned such that 20000 electrons corresponded a TOT of 30. The whole procedure consists of the following steps:

- Digital test

- Analog test

- Threshold tuning

- TOT tuning

- Monleak scan

- IV scan

The individual steps are described in the following chapter.

5.1 Sample 11-5B

The sample 11-5B was used to compare its behaviours with the irradiated sample. It was tuned and characterized in the same way as the irradiated sample. This way the changes between an unirradiated and an irradiated sample can be shown.

All tests and measurements with this sample were done at a bias voltage of -150 V and at room temperature. The leakage current was approximately $0.2 \, \mu\mathrm{A}$. To verify the function of the digital part of the FE-chip, a digital test was done. At this measurement a charge was injected 200 times into the digital read out electronics of the FE-chip. The chip showed a very consistent response. All pixels of the chip registered the 200 injected charges. Also the analogue test, which injects a charge 200 times into the analogue part of the FE-chip, showed a completely uniform response of the electronics. Every pixel showed the 200 charges which were injected.

The threshold was tuned by using the global and the individual threshold DAC's. The threshold scan, which was done at the end of the tuning procedure showed a threshold of 3199 electrons with a RMS of 27 electrons. The noise of the s-curve (see chapter 3.1.2) was $\sigma = 176.8 \pm 10.8$ electrons. The results of the threshold scan are shown in figure 5.1. With the IF-DAC and F-DAC tuning the TOT for a injected charge of 20000 electrons was tuned to 33.52 bunchcrossings with a RMS of 2.84.

To receive information about the uniformity of the leakage current a monleak scan was done. This scan measures the combined feedback and leakage current from the feedback circuit

$$I_{monleak} = I_{leak} + 2 \cdot I_f \tag{5.1}$$
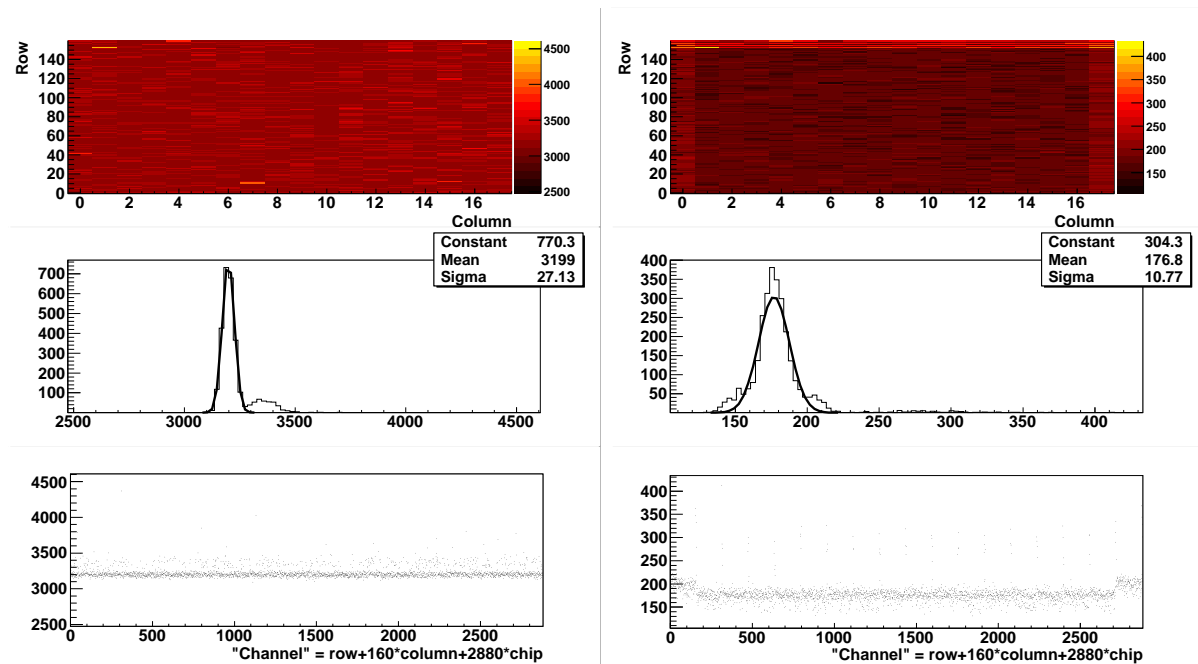
Figure 5.1: Left: Threshold-curve, right: Noise. Top: pixelmap with threshold and noise information. Middle: threshold and noise distribution. Bottom: threshold and noise for each of the 2880 pixels.
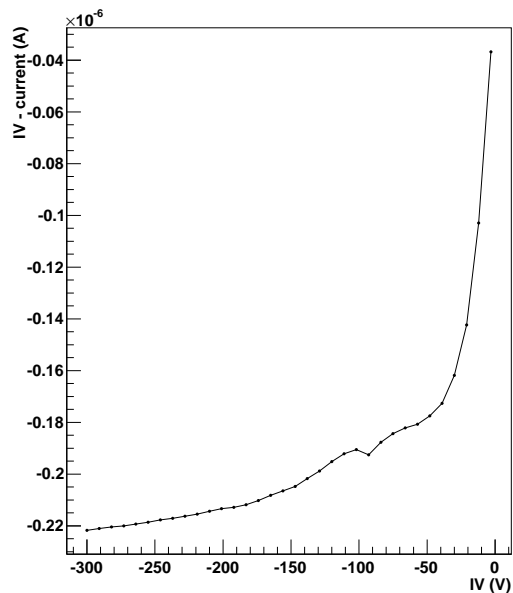
Figure 5.2: IV curve: Dependence of the leakage current on the bias voltage.

where I_f is defined by the IF and F-DAC parameters [9]. The monleak scan showed a homogeneous behaviour for the whole chip. There was no evidence for pixels with increased leakage currents.

The last scan that was done was an IV-scan. Here the bias voltage was changed in steps from -10 V to -300 V and the corresponding leakage current was measured. Figure 5.2 shows the IV-curve for sample 11-5B. At smaller bias voltages the leakage current is rising sharply, at higher bias voltages the dependency becomes more linear. Up to a bias voltage of -300 V, the IV-curve does not show a breakdown.

5.2 Sample 4-6B

This sample was irradiated with thermal neutrons to a dose of $1 \cdot 10^{15} \text{cm}^2$ neutron equivalent. This is the ATLAS lifetime dose for a pixel module. With this the behaviour of the sensor and the FE-chip at the end of the ALTAS lifetime can be studied.

To minimize the leakage current, the tuning procedure and the later measurements were done at a chuck temperature of -40°C. That corresponds a sensor temperature[1] of approximately -25°C. The sensor was in a good state and the tuning of the chip was possible without bigger problems. The tuning and characterization procedure was done at a bias voltage of -600 V. This is the maximal possible voltage in the ATLAS detector. At -600 V the leakage current was approximately 2.2 μA. Because of sensor and electronics defects which were generated by irradiation, the sample showed more noise than the unirradiated sample. In the analogue test the most normal pixels showed 200 injected hits, but especially the long ganged and interganged pixels were noisy. They showed up to 220 hits. The long pixels showed more noise, because they have a bigger surface then the normal pixels, and they lay at the edges of the sensor. Leakage current from the edge of the sensor increases the noise for these pixels. The reason for the higher noise level of the ganged pixels is the fact, that in comparison to normal pixels, the sensor surface is doubled. The digital test showed no differences to the unirradiated sample, where all pixels showed the 200 injected charges.

It was not possible to do a normal G-DAC tuning. The tuning procedure choose the G-DAC value very low. That increases the noise heavily and made a threshold scan impossible. This problem was fixed by setting the G-DAC value by hand to a higher value of 24. With this setting the noise was decreased and the T-DAC tune and threshold scan worked. Figure 5.3 shows the threshold distribution for sample 4-6B. With 3261 ± 49 electrons the threshold was further away from the set value of 3200 electrons than at sample 11-5B. With $\sigma = 290.3 \pm 17.8$ electrons also the noise was approximately 100 electrons higher than at sample 11-5B. The noise distribution (figure 5.3 middle, right) shows a smaller peak at high values. One reason for this peak are the long ganged and intergang pixels. Especially the long pixels show a different behaviour, as can be seen in the hitmap and the pixelnumber-threshold plot (figure 5.3 upmost and bottommost). However it can be seen that also many normal pixels are responsible for the peak. The reason for this behaviour lies in the worse performance of these pixels after irradiation. In figure 5.3 (top) it also can be seen that there are pixels, where the fit does not work (shown in white). Especially the long pixels and a few ganged pixels were too noisy to be fitted. The TOT for 20000 electrons was tuned to 33.53 bunchcrossings, with a RMS of 2.84. Here the tuning itself worked without any differences to sample 11-5B, also the tuned value was very similar. Only the RMS was a bit higher as at sample 11-5B.

---

[1]Measured with the NTC of the single chip card attachment.
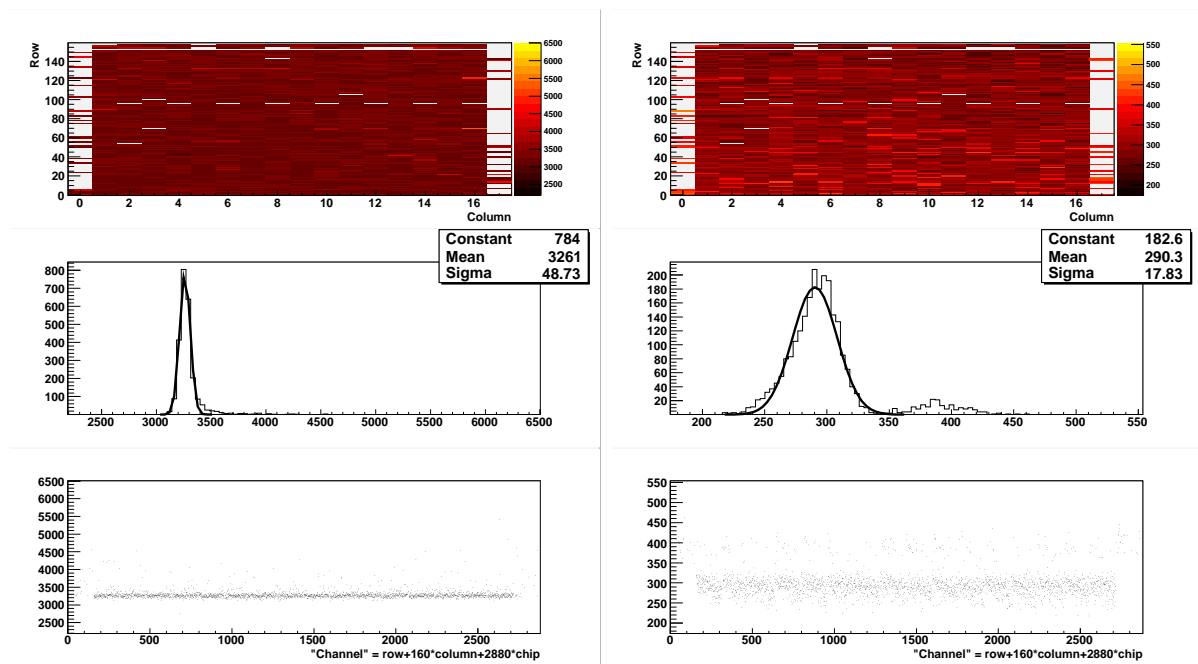
Figure 5.3: Left: Threshold-curve, right: Noise. Top: pixelmap with the threshold and noise information, with pixels where the s-curve fit did not converge (in white). Middle: threshold and noise distribution. Bottom: threshold and noise for each of the 2880 pixels.
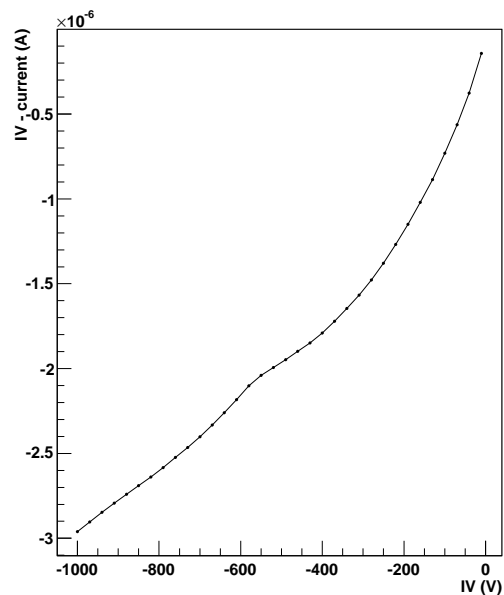
Figure 5.4: IV-curve: Dependence of the leakage current on the bias voltage.

A monleak scan was done, which showed higher monleak currents and a bigger spread of the distribution than the unirradiated sample. This was expected because of the higher leakage current of the whole sensor. Apart from that there was nothing special in the monleak scan. The monleak current was uniform for the whole sensor.

An IV-scan was done up to a bias voltage of -1000 V. In figure 5.4 the scan results are shown. On the measured bias voltage range no breakdown can be seen.

Table 5.1 shows the parameters of the evaluated samples. With the limitation that the G-DAC value had to be set by hand, the irradiated sample could be tuned and used in the same way as the unirradiated sample. The noise level and the leakage current of the irradiated sample were higher than at the non irradiated one. Especially the long pixels were very noisy and many of them could not be tuned. After irradiation with the ATLAS lifetime dose the sample 4-6B showed a good performance and it was still usable for particle detection.

	11-5B	4-6B
Dose [Neq]	0	$1 \cdot 10^{15}$
Irradiation type	-	thermal neutrons
Chuck temperature	room temperature	-40°C
Temperature near the sensor	room temperature	-24°C
V_{bias} [V]	-150	-600
I_l [µA]	0.2	2.1
Threshold [e$^-$]	3199 ± 27	3261 ± 49
Width of the threshold distribution [e$^-$]	176.8 ± 10.8	290.3 ± 17.8
TOT_{20000}	33 ± 2	33 ± 3

Table 5.1: Characteristics of the studied samples.

6 Time-Resolved Hit Efficency Measurements

Every 25 ns a LHC bunchcrossing happens inside the ATLAS detector. The FE-chip has to relate the collected hits to the correct bunchcrossings. The detection probability during a bunchcrossing is studied before and after the irradiation of a module. The unirradiated sample 11-5B and the irradiated sample 4-6B are used. An ideal module would have a detection probability of one during the correct bunchcrossing and zero before and afterwards (figure 6.1 left). In case of the real module the detection probability rises at the beginning of the bunchcrossing up to a value near one and decreases to zero again at the end of the bunchcrossing (figure 6.1 right). In this chapter the behaviour of the detection probability will be studied for an unirradiated and an irradiated sample. The detection probability in the middle of the bunchcrossing, where the plateau of the distribution is reached and, the slopes of the distribution are evaluated.
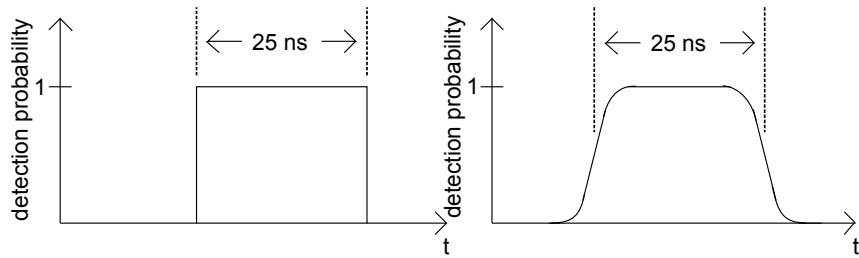
Figure 6.1: Detection probability for an ideal module (left) and for a real module (right).

To study these behaviours, laser pulses are injected into the sensor at different times during the bunchcrossig. For this, the laser pulses are delayed with respect to the clock. At the slopes of the detection probability distribution the laser is delayed in 1 ns steps. In the middle of the bunchcrossing, when the plateau is reached, the laser delay is changed in 2.5 ns steps. For every delay time 1000 laser pulses are injected into the sensor and the number of hits that are detected in the different LV1IDs is counted.

For the evaluation, the data is fitted. The fit is a combination of a box fit and two error functions on the edges of the distribution. For the measurement of the slopes, the standard deviation from the error functions are used. The FWHM[1] of the distribution and the point in time of the center of the distribution are also given by the fit. The fit function is:

$$f(x) = \frac{1}{2} \cdot (1 + F \cdot (x - x_0)) \cdot A \cdot \frac{\left(0.5 \cdot \left(1 + erf\left(\frac{x+W-x_0}{\sqrt{2}\cdot\sigma}\right)\right)\right) - \left(0.5 \cdot \left(1 + erf\left(\frac{x-W-x_0}{\sqrt{2}\cdot\sigma}\right)\right)\right)}{W}$$

(6.1)

A, F, W, x_0, and σ are parameters of the fit. W is the FWHM of the distribution divided by two, and σ is the standard deviation of the error function. x_0 gives the point in time of the center of the distribution. An example for recorded data with the fit is shown in figure 6.2[2].

---

[1] Full width half minimum; width of the distribution at a probability of 50%

[2] In this plot, as in all other plots in this chapter, the error bars are not shown.
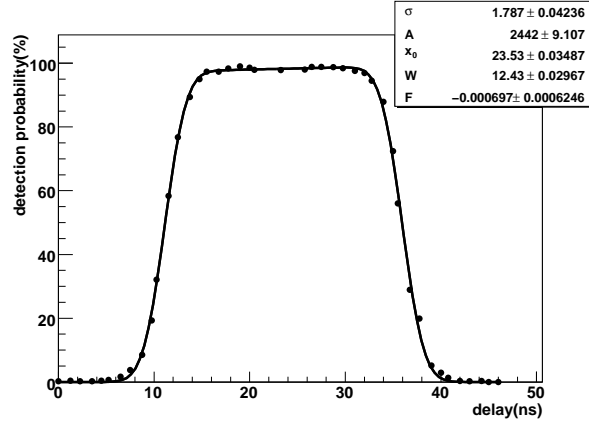
Figure 6.2: Example for a detection probability distribution fitted with equation 6.1.

The detection probability distribution is measured in three different ways. The time of the laser injection can be varied by changing the time of the laser pulse emission. It is also possible to change the arriving time of the trigger at the module. The third way is to change both, the laser pulse emission and the trigger arrival at the module together. As reference time for the delay measurements, the first clock cycle that lies in the LV1ID window is defined as zero (measured without any delay). All delays are referred to this point in time. The phase between the beginning of the bunchcrossing and the time of the laser injection is not known, but constant without delay.

All measurements are done with two different injection charges. By traversing the sensor, a MIP creates approximately 20000 electrons, so this charge is also chosen for the measurements. The second charge that is used is 10000 electrons. It is chosen to see the behaviour at lower charges like they are produced after the irradiation of a sensor.

For the detection probability measurements the beamspot diameter is set up small enough that only one pixel is illuminated by the laser. The diameter of the beamspot is controlled like described in chapter 4.4.2. The laser beamspot is located in the middle of the used pixel. All other pixels that are not illuminated are disabled to minimize noise hits.

6.1 The External Trigger

To study the detection probability during a bunchcrossing, hits are injected at different times during the bunchcrossing. For that task an external trigger system was installed (see figure 6.3), it is used to trigger the laser pulse emission and the read out trigger of the USBPix system.

To generate the trigger signal a frequency generator AGF 3521 from Tektronix is used. This frequency generator is triggered by the 40 MHz clock from the single chip card. This way the output signal from the frequency generator is generated always at the rising edge of the clock from the single chip card. The output of the frequency generator shows a jitter of up to 100 ps [44].

As trigger signal a 1 μs long pulse is used. This pulse has a low level of 0 V and a high level of 5 V, the rising time of the signal is 2.5 ns . It is send with a frequency of 20 kHz, which was one of the frequencies that were calibrated in chapter 4.3.

The output of the frequency generator is connected with LEMO cables of the same length to the laser trigger input and to the external trigger input of the USBPix system. When the trigger reaches the USBPix system, it read out a 16 bunchcrossings long LV1ID window (see
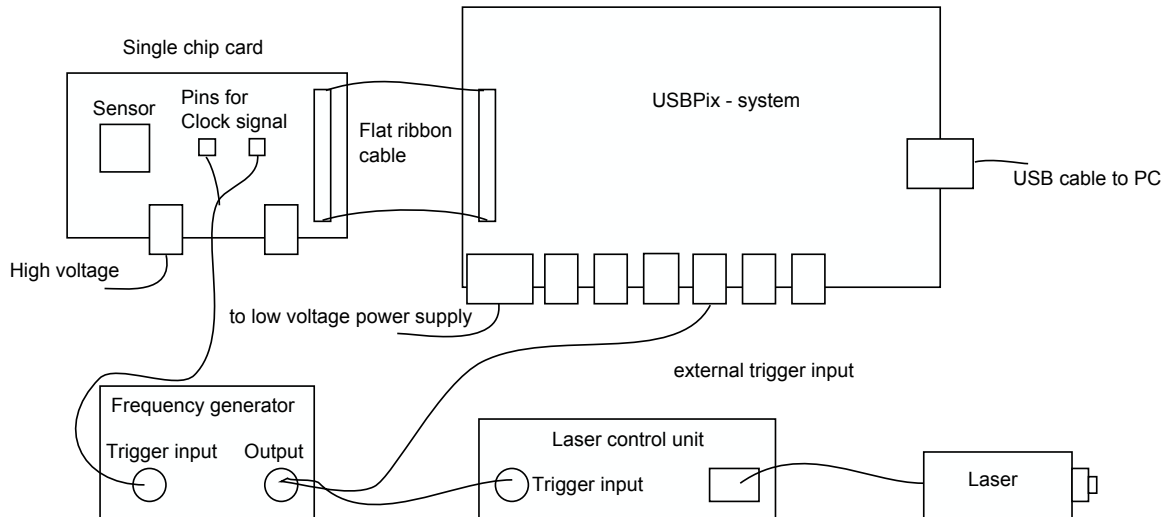
Figure 6.3: The trigger circuit.

chapter 3.1.2). The hit is always sorted into that LV1ID which belongs to the clock cycle after the next rising edge of the clock shifted back by the latency (see chapter 3.1.2). The trigger delay is set up that way that the hits are collected in LV1ID 9.

As mentioned above, there are three different ways to measure the detection probability distribution during a bunchcrossing (or during one LV1ID). In all three cases the different measurement times are produced by varying the length of the cables that lead to the laser trigger or to the USBPix system trigger input. So the signals are delayed and different laser injection times can be set.

The delay time of the different cables is controlled by an oscilloscope. In this process a pulse provided by the frequency generator is observed with the oscilloscope at the input and output of the LEMO cable. The time difference between the two signals is measured with the oscilloscope. Figure 6.4 shows such a measurement. These measured delay times for the different LEMO cables are added up to calculate the correct time delay for the different measurements. With these measurements the cable delay times can be determined very precisely. The errors of these cable delay times where very small in comparison to the delay times and are not considered in the evaluation.

6.1.1 Laser Delay

For the laser delay measurements the cable that leads from the frequency generator output to the laser trigger input is extended. So the time of the laser injection is delayed in comparison to the clock. The trigger for the USBPix system is not delayed. Figure 6.5 shows the timing of the trigger system. The first line shows the 40 MHz clock, the second one shows a 20 kHz signal not in phase with the clock[3]. The third line shows the frequency generator output in phase with the clock. The fourth line shows the Front-End preamplifier output. The position of this output peak depends on the time when the laser pulse is injected, and this depends on the laser delay. The fifth line shows the Front-End discriminator output that has, for equal charges a fixed distance to the preamplifier output. The sixth line shows the Front-End trigger input. This trigger is also generated by the frequency generator, but it is not delayed like the laser

---

[3]The distance between the shown 20 kHz peaks are not in the correct scale.

Figure 6.4: Example of a cable delay time measurement for a 5 ns delay LEMO cable.

trigger. The USBPix system trigger delay[4] is set in such way that the rising discriminator edge is in the middle of the LV1ID window. The LV1ID window is shown in green[5]. The seventh line shows the clock, again. By the following lines the discriminator output (blue) and the trigger input of the module (red) are shown for different laser delays. The numbers show the LV1IDs of the bunchcrossings. Because of the stable time of the trigger input the LV1IDs do not change with respect to the clock. A hit is sorted into that LV1ID where the discriminator output rises. This window is labeled with a red number.

As one can see in figure 6.5, with an increasing delay of the laser injection the LV1ID increases. The LV1ID always changes when the rising edge of the discriminator output passes the rising edge of the clock. The width of the slopes of the detection probability distribution is generated by the discriminator jitter. If the discriminator rises a bit earlier, the hit is associated with a lower LV1ID. If the discriminator rises a bit later it is associated to a higher LV1ID.

Even when holding the produced charge constant, the time when the discriminator edge rises depends on several factors. The laser pulses are sent out, when the laser is triggered, which happens with an accuracy of 4 ps. This is a very small time, so this effect does not have a big influence on the slope.

The time, when the discriminator rises also depends on the time when the frequency generator sends the trigger signal, which jitters up to 100 ps in comparison to the clock[6].

An influences on the slope, which is caused by the sensor itself, is the time interval, in which the electron-hole pairs are created inside the sensor, and in which they drift to the surface of the sensor. Also the Front-End electronic has an influence on the discriminator rinsing time.

Another influence on the discriminator output is the jitter of the arriving trigger signal. The trigger signal for the USBPix system is created by the frequency generator with the same accuracy as the trigger signal for the laser (100 ps). This signal is processed by the USBPix system and the jitter of the processed signal is unknown. If the trigger jitter had an influence on the measurement, this would be seen in a changing of the LV1ID even if the laser pulse was

---

[4]This is not the trigger delay which is set with a delay cable, but the USBPix system trigger delay to set the right module timing. Compare 3.1.2.

[5]only a 4, instead of 16, bunchcrossing long LV1ID window is shown in figure 6.5.

[6]This jitter is a feature of the frequency generator

injected in the middle of a bunchcrossing (see chapter 6.1.2). For the measurements it is ensured that this is not the case.

The laser intensity is not exactly the same for every laser pulse. This causes different injection charges which shifts the rising edge of the discriminator (timewalk), and which is another reason for the shape of the slope of the detection probability distribution. Because of the charge dependence of the discriminator output (see chapter 3.1.2), it is expected that the laser signal is detected later for smaller charges. Larger charges are detected faster and still occur in the previous bunchcrossing, while smaller charges already occur in the following bunchcrossing.
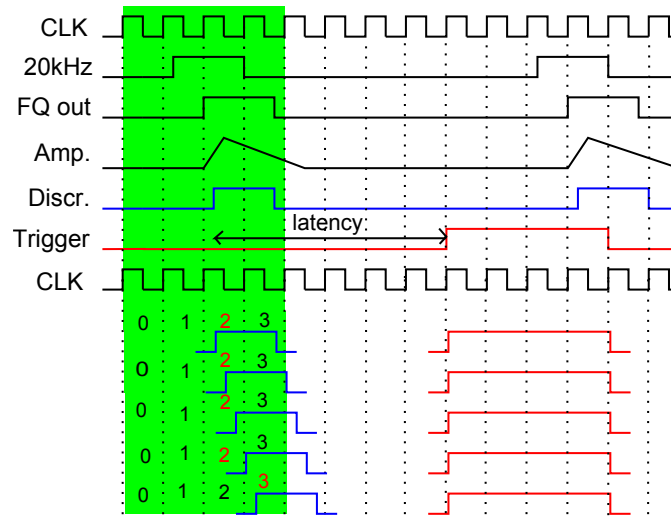
Figure 6.5: Time behaviour of the system: Upper part: The behaviour between the clock, the frequency generator output, the Front-End amplifier, the discriminator output (blue) and the readout trigger is shown. In the lower part the Front-End discriminator output (blue) and the readout trigger (red) are shown for different laser injection times. A four bunchcrossing wide LV1ID acceptance window is marked in green, the LV1IDs of the hits are given in red.

6.1.2 Trigger Delay

For the delay of the trigger signal the cable that leads to the USBPix System trigger input is extended. This delays the time at which the trigger arrives at the FE-chip. With the delay of the trigger the beginning of the LV1ID window is also delayed. Figure 6.6 shows the delay of the trigger in red and the LV1ID window in green. The different rows show the same signals as in chapter 6.1.1. The first rising edge of the clock, which lays in the LV1ID window, belongs to the bunchcrossing that gets the LV1ID 0. The LV1IDs are labelled as described in figure 6.5. The laser pulse, and thus the discriminator output (in blue), is not delayed and arrives always at the same time. The laser intensity fluctuations and the discriminator output jitter have no influence on the measurement, because it is ensured that the rising edge of the discriminator lies in the middle of a bunchcrossing. Because of this independence from the discriminator output jitter the different injected charges of 10000 and 20000 electrons are assumed to have no influence on the detection probability.

The LV1ID always changes when the beginning of the LV1ID window passes a rising edge of the clock. If the beginning of the acceptance window is exactly on the rising edge of the clock, it
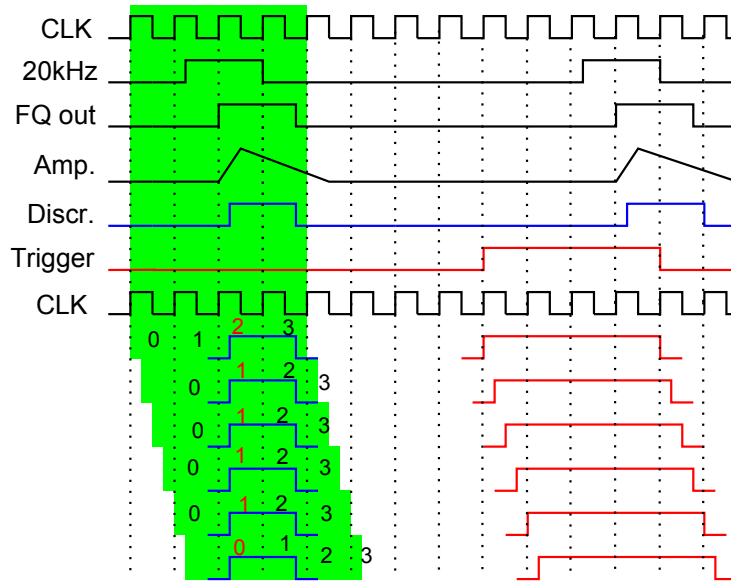
Figure 6.6: Time behaviour of the system: Upper part: Behaviour between the clock, the frequency generator output, the Front-End amplifier and discriminator (blue) output and the trigger for the hit readout is shown. In the lower part the Front-End discriminator output (blue) and the trigger for the hit readout (red) are shown for different trigger delays. The four bunchcrossing wide LV1ID acceptance window, shown in green, moves with the time of the trigger. The LV1IDs of the hits are shown in red.

depends on the Front-End electronics, with which LV1ID window the hit is associated. If the processing of the arriving trigger is fast, the trigger signal arrives before the clock edge rises and the hit is sorted into the higher LV1ID window. If the processing is a bit slower, the trigger arrives after the clock edge rises and so the following bunchcrossing gets the LV1ID 0, so the hit is sorted into the lower LV1ID. The speed of the signal's processing depends, in first order, on the preamplifier and the discriminator behaviour. But, especially after irradiation, also the other electrical components can have an influence on the processing time.

Through delaying the trigger signal in comparison to the clock, the trigger arrives later at the FE-chip, the delay gets bigger and the bunchcrossing, or LV1ID where the hit is detected, gets larger. If the beginning of the LV1ID window (which depends on the trigger delay) is compared to the time of the discriminator output rising, it is observed that for the module it seems like the laser pulse comes earlier after the beginning of the acceptance window. This can be seen in figure 6.6 by comparing the distance between the beginning of the LV1ID window and the rising edge of the discriminator for the different trigger delays. Because of this behaviour the LV1IDs gets smaller for bigger trigger delay times.

6.1.3 Laser and Trigger Delay

A third method is the simultaneous delay of both, laser and trigger. During this measurement both signals are delayed by the same cable. In this case the LV1ID changes from smaller values to higher ones when the rising edge of the discriminator output passes the rising edge of the clock[7] (figure 6.7, row 3 or row 9). When the beginning of the LV1ID window passes the rising

---

[7]As described in chapter 6.1.1.
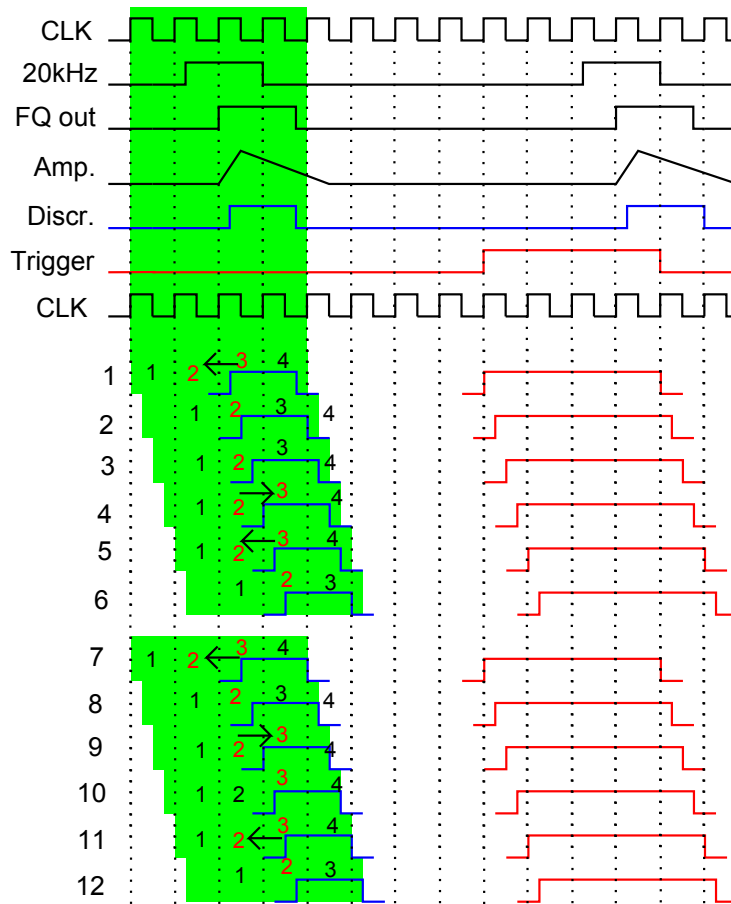
Figure 6.7: Time behaviour of the system: Upper part: The behaviour between the clock, the frequency generator output, the Front-End amplifier and discriminator output (blue) and the trigger for the hit readout is shown. Middle part: The behaviour while delaying laser and trigger simultaneously with laser injection in the fist quarter of a bunchcrossing. Lower part: The behaviour while delaying laser and trigger simultaneously with laser injection in the middle of a bunchcrossing. The arrows show when the LV1ID is shifted in which direction.

edge of the clock, the LV1ID changes from higher to smaller values[8] (figure 6.7, row 1, 5, 7 or 11). This results in a toggling of the hits between two LV1ID values, as it can be seen in figure 6.7.

The sum of the width of the hit detection probability distributions of both LV1IDs is the width of the bunchcrossing. The ratio between the widths of the two distributions depends on the phase of the rising edge of the discriminator output in comparison to the clock. When the discriminator rises after a quarter of the bunchcrossing, the FWHMs are divided in a ratio three to one (see figure 6.7 middle). If the discriminator output rises in the middle of the bunchcrossing, the FWHMs are divided in a ratio of one half (see figure 6.7, bottom). Through this measurement the time, when the discriminator output rises, and with this the approximate laser injection time T, is given by the width of the hit detection probability distribution with the higher LV1ID.

---

[8]Like described in chapter 6.1.2

6.2 Measurements with Sample 11-5B

First the hit detection probability of the unirradiated sample 11-5B was examined. For measuring of the hit detection probability during a bunchcrossing the sample was tuned as described in chapter 5.1. All measurements were done at room temperature, the threshold was tuned to 3200 electrons and a bias voltage of -150 V was applied. The leakage current was 3.6 μA, and the laser attenuator was set in such way that the photovoltage was 156.9 ± 0.2 mV, which corresponded a charge of 10861.1 ± 13 electrons. To reach the charge that should correspond an MIP, the laser attenuator was set in such way that the photovoltage was 308.7 ± 0.2 mV. This corresponded an injected charge of 21333.3 ± 13 electrons. For the measurements pixel 9/13 was used.

The beamspot diameter was controlled for 10000 and 20000 electrons charge, in order to secure that it was smaller than the size of a pixel. It was also ensured that the beamspot was in the middle of a pixel so that no other pixels showed hits. Then the remaining pixels were disabled to minimize noise.

These three measurements were all made consecutively in the order: laser delay, trigger delay, laser and trigger delay. The laser intensity stayed constant, in the range of the shown errors, during the whole measurement.

6.2.1 Laser Delay

Figure 6.8 shows the hit detection probability during one bunchcrossing for 10000 electrons and 20000 electrons injected charge. With the help of equation 6.1 the FWHMs were calculated. The widths σ of the slopes, the center positions x_0 of the distributions and the heights M of the distribution plateaus were also given by equation 6.1. Table 6.1 shows the results of the laser delay measurements.
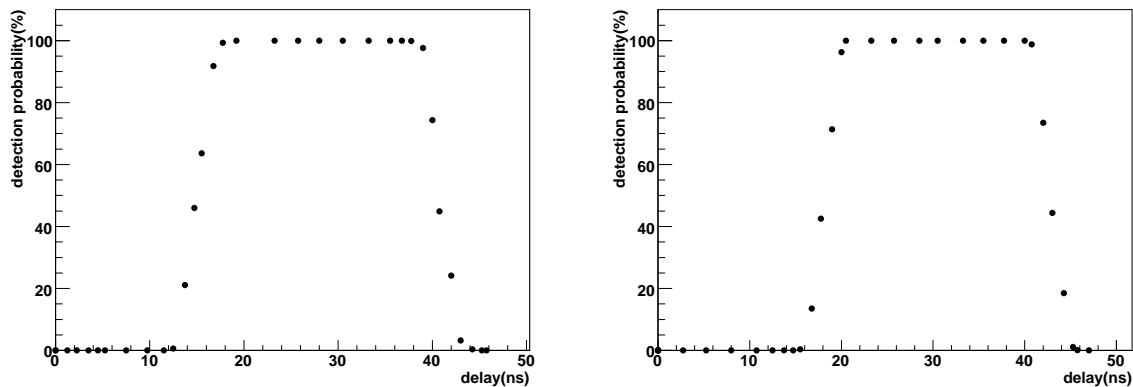
Figure 6.8: Hit detection probabilities during a bunchcrossing for sample 11-5B measured by delaying the laser; left: 10000 electrons injected charge; right: 20000 electrons injected charge.

It is apparent that the FWHMs of the measurements at 10000 electrons and at 20000 electrons differ by about 1.1 ± 0.1 ns. This effect was unexpected, because the FWHM depends only on the length of the clock cycle, but not on the injected charge. As reason for the differing FWHMs, a problem with the delay time is assumed. A defect LEMO cable extension plug, which causes an additional delay, is one example for such a problem. An evidence for this assumption is that such differences which were seen here, were also seen in other FWHM measurements. The differences

	10000 electrons	200000 electrons
FWHM (ns)	25.86 ± 0.08	24.74 ± 0.07
slope (ns)	1.33 ± 0.05	1.30 ± 0.04
x_0 (ns)	27.85 ± 0.04	30.49 ± 0.04
M (%)	100 ± 0.1	100 ± 0.1

Table 6.1: Summary of the measured values of the laser delay measurement with sample 11-5B.

in all these measurements had nearly the same size (see below). That the higher injection charge is responsible for different FWHMs is unlikely, because a higher injection charge only leads to a faster discriminator rising and as a result, to an earlier hit detection. This timewalk effect causes the later center position x_0 of the distribution for 20000 electrons. The center position of the distribution for 10000 electrons is found to be 2.64 ± 0.06 ns before that of the distribution for 20000 electrons. This value can be compared with the expected value from the timewalk effect.

Figure 6.9 shows the timing behaviour of an FE-I3 chip. On the x-axis the charge is shown, on the y-axis the rising time t_0 of the preamplifier can be read. The upper dashed line shows the rising time for a high injection charge (e.g. 150000 electrons). By the distance between this line and the lower horizontal lines, the timewalk for a certain charge is represented. The lower dashed line and the solid black line show the in time threshold[9], which corresponds to a charge of approximately 5800 electrons. The two solid red lines show the timewalk for 10000 electrons and 20000 electrons charge. It can be seen that the difference between the timewalk of 10000 electrons and that of 20000 electrons is approximately 6 ns. This difference is twice the value that was measured. A possible explanation for this difference could be that the measured value is compared to the timewalk of a different FE-I3 chip. So maybe the timewalk for different FE-chips, or even different pixels, have a spread bigger than 3 ns.
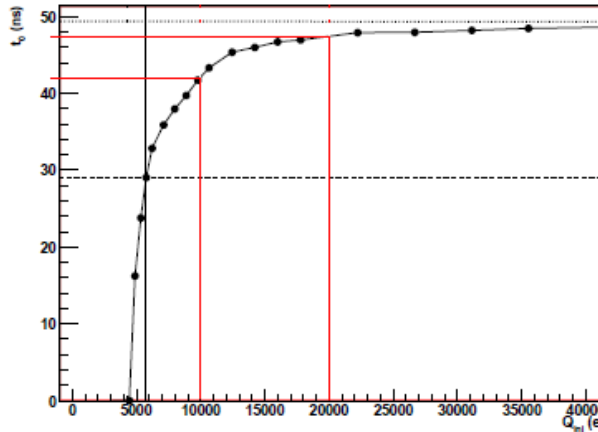
Figure 6.9: Timing behaviour of one pixel of an FE-I3 chip [9]. The charge is shown on the x-axis. On the y-axis the rising time t_0 of the preamplifier is shown. For the description of the lines, see the text.

---

[9]At the in-time threshold the injected charge is so low that the timwalk is more than 20 ns (at 25 ns the hit would be detected in the wrong bunchcrossing).

The slopes of the hit detection probability distributions are equal in the range of the errors. This suggests that the magnitude of the injected charge has no influence on the sensor performance or on the Front-End electronics noise, which creates the width of the slope.

The plateau value of the hit detection probability distributions is for both injected charges 100%. This shows that in the middle of a bunchcrossing the hit detection probability for an unirradiated module is very good.

6.2.2 Trigger Delay

The evaluations of the trigger delay measurements were done in the same way as the laser delay measurements. The plots for the hit detection probability measurements with 10000 and 20000 electrons injected charge are shown in figure 6.10, and the results of the measured values are shown in table 6.2.
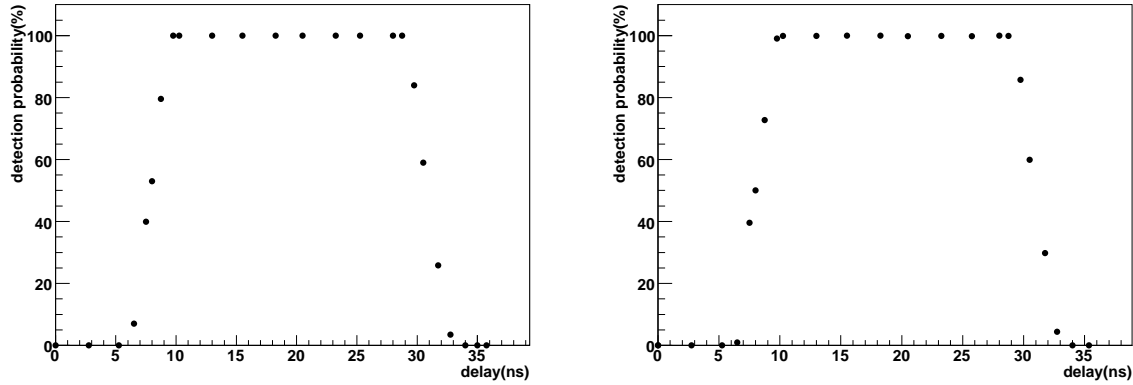
Figure 6.10: Hit detection probabilities for sample 11-5B while delaying the trigger; left: 10000 electrons injected charge; right: 20000 electrons injected charge.

	10000 electrons	200000 electrons
FWHM (ns)	22.98 ± 0.06	22.9 ± 0.1
slope (ns)	1.11 ± 0.04	1.14 ± 0.06
x_0 (ns)	19.38 ± 0.04	19.48 ± 0.06
M (%)	100 ± 0.1	100 ± 0.1

Table 6.2: Summary of the measured values of the trigger delay measurement with sample 11-5B.

The FWHMs of the distributions for 10000 and 20000 electrons injected charge are, in the range of the errors, equal. The FWHMs of the laser delay measurements are approximately 3 ns for 10000 electrons injected charge and approximately 2 ns for 20000 electrons injected charge wider than those of the trigger delay measurements. The FWHMs of the distributions should be always the same, because they depend only on the length of the clock cycle, which was equal for both measurements. It is assumed that the difference between the laser and the trigger delay measurements has its origin in the data processing in the USBPix system, but the actual reason

of the phenomenon could not be spotted.

In the range of the errors, the slopes of the trigger delay measurement are equal for both injected charges. Because of the injection charge independence (see chapter 6.1.2) of the trigger delay measurements this behaviour was expected.

Also the center positions of the hit detection probability distributions are equal, in the range of the errors. The cause of this behaviour is that the point in time, when the LV1ID window changes, depends only on the phase of the trigger for the FE-chip in respect to the clock. In this case the discriminator rising does not matter, because it always rises in the middle of a bunchcrossing and the timewalk effect is too small to switch the bunchcrossing.

As for the laser delay measurement, the hit detection probability on the plateau of the distribution was for both injected charges, 100%.

The laser and trigger delay measurements show different slopes. For the measurement with 10000 electrons injected charge, the slope was 0.22 ± 0.06 ns wider for the laser delay measurement as for the trigger delay measuremet. For 20000 electrons injected charge the slope measured with the laser delay measurement was 0.16 ± 0.07 ns wider than that with the trigger delay measurement. This is, because during the trigger delay measurement the spread of the laser intensity and the sensor's behaviour have no influence on the slope (see chapter 6.1.2). Instead, the pure electronics effects, which are responsible for the width of the slopes, can be observed. Together with the hit detection probability measurements it could be shown that the electronics of sample 11-5B caused a slope of 1.11 ± 0.04 ns for 10000 electrons injected charge and of 1.14 ± 0.06 ns for 20000 electrons injected charge. The broadened slopes seen in the laser delay measurements could be linked to sensor and laser behaviours. Which part of the broadening was related to the laser and which one to the sensor could not be determined.

The equal plateau values of the hit detection probabilities were expected, because in the middle of the bunchcrossing neither the beginning of the LV1ID window nor the discriminator were at the edge of the clock. It makes no difference for the single measurement whether the LV1ID window or the discriminator edge is moved in steps, so equal plateau values were expected and observed. In both cases, none of the 1000 injected hits got lost, so the plateau values were (100 ± 0.1)%.

6.2.3 Laser and Trigger Delay

To calculate the phase of the injection with respect to the clock, the laser and trigger delay measurement was done. The delay time range was chosen big enough to measure two hit detection probability distributions for each LV1ID. When one complete bunchcrossing is scanned by the measurement, one detection probability distribution is measured for both LV1IDs. When the delay was furthermore enhanced until it reached the next bunchcrossing, the hits were again related to the first LV1ID, as it is discribed in chapter 6.1.3. With this toggling a second hit detection probability distribution could be measured by extending the delay cabels. In figure 6.11 the different rising and falling times, of the slopes can be seen, the FWHMs for LV1ID 8 and 9 are shown in table 6.3. The laser injection times T are shown separately for 10000 and 20000 electrons. The last row of table 6.3 shows the average laser injection time of both measured distributions for each injected charge.

For 10000 electrons the difference between the injection times for the two measured distributions was 0.9 ± 0.1 ns. Again this difference was as in the laser delay measurement, probably related to a problem with the delay cables. For 20000 electrons charge there was no injection time difference measured between the two distributions.
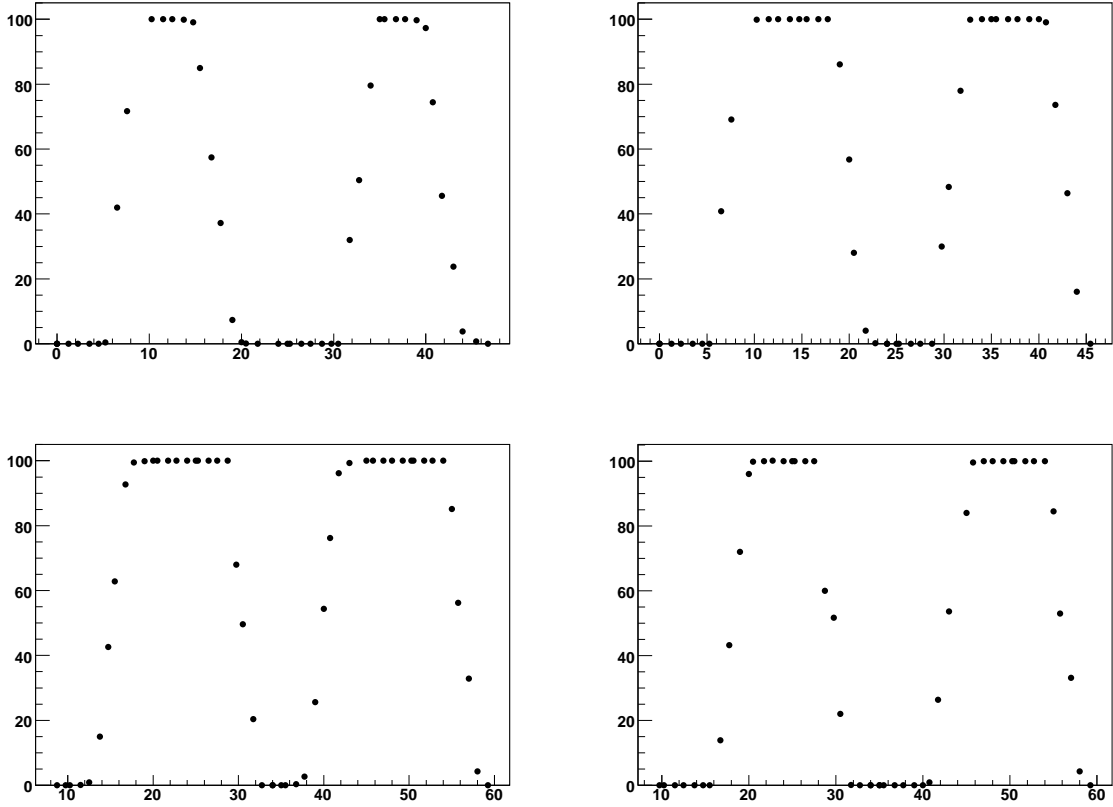
Figure 6.11: Hit detection probabilities for sample 11-5B, LV1ID 8 (above) and LV1ID 9 (below). On the left the plots for 10000 electrons injected charge are depicted, on the right these for 20000 electrons injected charge.

The difference between the injection times of 10000 and 20000 electrons charge is of the same order as the differences between the center positions x_0 of the distributions from the laser delay measurement ($2.64 \pm 0.06\,\text{ns}$ in comparison to $3.3 \pm 0.2\,\text{ns}$), but it is not in the region of the expected timewalk of 6 ns.

	$10000\,e^-$		$20000\,e^-$	
	LV1ID 8	LV1ID 9	LV1ID 8	LV1ID 9
FWHM 1	$10.66 \pm 0,1$	$15.03 \pm 0,07$	$13,0 \pm 0,1$	$11.6 \pm 0,1$
T	$15.03 \pm 0,07$		11.6 ± 0.1	
FWHM 2	9.0 ± 0.1	$16.18 \pm 0,07$	$13.2 \pm 0,2$	$11.6 \pm 0,1$
$T\,2$	16.18 ± 0.07		11.6 ± 0.1	
Avg T_{avg}	$15,6 \pm 0.1$		12.3 ± 0.2	

Table 6.3: Overview of the widths and injection times for laser and trigger delay measurement with sample 11-5B.

6.3 Measurements with Sample 4-6B

The same measurements that were done with sample 11-5B were also done with sample 4-6B, so it was also tuned to a threshold of 3200 electrons, like it was described in chapter 5.2. To minimize the leakage current, the chuck temperature was set at -40°C, which corresponded a sensor temperature of approximately[10] -25°C. The bias voltage was set to -600 V, and the leakage current was approximately 2.16 µA.

Before the beginning of the measurements it was ensured that the beamspot diameter was smaller than the size of a pixel. Thus it was made sure that the whole charge was injected into one pixel. This was successfully checked by a test measurement, where only the pixel which was illuminated by the laser beam showed hits.

Again, pixel 9/13 was used, for the measurements, all other pixels were disabled. First, the measurements with 10000 electrons injected charge were made with each of the three different delay types, then those with 20000 electrons followed. At the beginning of the measurements with 10000 electrons, the NTC installed at the attachment structure of the single chip card showed a temperature of $(-24 \pm 1)°\,$C. The voltage of the photodiode was $160.5 \pm 1.5\,$mV during the whole measurement, which corresponds to a charge of 11118 ± 104 electrons. At the beginning of the measurement with the injection charge of 20000 electrons, the temperature was $(-25 \pm 1)°\,$C, during the whole measurement the photovoltage had the value $311.3 \pm 0.4\,$mV. That corresponds to a charge of 21583.3 ± 27.7 electrons.

6.3.1 Laser Delay

Table 6.4 shows the results of the laser delay measurement, and figure 6.12 shows the corresponding hit detection probability distributions.

	10000 electrons	200000 electrons
FWHM (ns)	24.90 ± 0.06	24.86 ± 0.07
slope (ns)	1.89 ± 0.04	1.78 ± 0.05
x_0 (ns)	23.53 ± 0.04	23.51 ± 0.04
M (%)	98.0 ± 0.2	98.4 ± 0.2

Table 6.4: Summary of the measured values of the laser delay measurement with sample 4-6B.

The FWHMs of the hit detection probability distributions are, for 10000 and 20000 electrons injection charge, in the range of the errors, equal. This was expected (see chapter 6.1.2) and supports the assumption that the different FWHMs of the laser delay measurement with sample 11-5B are caused by a parasitic error.

The measurement results for the slopes for 10000 and 20000 electrons injected charge are slightly different. This small difference of $110 \pm 60\,$ps can be interpreted as a small injection charge dependence of the slope, but it can also be interpreted as outer or as statistical influences on the measurement. For a charge dependency of the slope, no cause could be found, so the second interpretation seems the more likely one.

The center positions of the hit detection probability distributions are equal in the range of the errors. Because of the timewalk effect, they were expected to have a difference of 6 ns. An explanation for the equal center positions might be some influence of the irradiation. If in

---

[10]The temperature was measured with the NTC that was installed at the attachment of the single chip card.
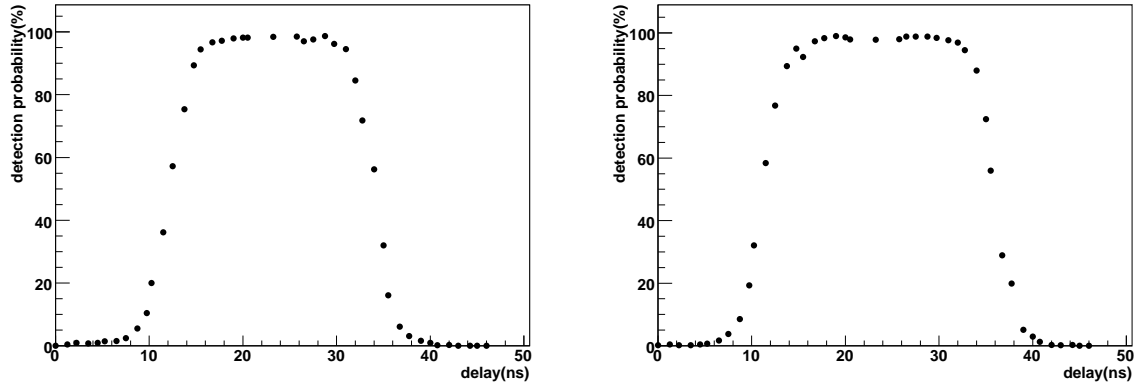
Figure 6.12: Hit detection probabilities for sample 4-6B while delaying the laser; left: 10000 electrons injected charge; right: 20000 electrons injected charge.

an irradiated FE-chip also bigger charges were detected more slowly, the timewalk differences between 10000 and 20000 electrons injected charge would have a smaller relativ effect.

The hit detection probabilities on the plateaus of the distributions are very similar for both injected charges, but that one of 20000 electrons is $(0.4 \pm 0.3)\%$ higher. The lower the injected charges are the likelier it is that the number of electron-hole pairs is no longer high enough to exceed the discriminator threshold. Recombination of electron-hole pairs as well as trapping[11] caused by irradiation can lower the number of free charge carriers. This explains why the hit detection probability of an irradiated sample is bigger for high injection charges.

6.3.2 Trigger Delay

Table 6.5 and figure 6.13 show the results of the trigger delay measurements for sample 4-6B.

	10000 electrons	200000 electrons
FWHM (ns)	24.06 ± 0.08	22.00 ± 0.08
slope (ns)	1.14 ± 0.05	1.03 ± 0.05
x_0 (ns)	19.80 ± 0.04	18.75 ± 0.05
M (%)	98.7 ± 0.4	99.0 ± 0.1

Table 6.5: Summary of the measured values of the trigger delay measurement with sample 4-6B.

During these measurements the hit detection probability distributions start rising at the same delay time ($\approx 5\,\mathrm{ns}$) for both injected charges, but the distribution for 20000 electrons injected charge falls to zero again $2\,\mathrm{ns}$ earlier than the distribution for 10000 electrons ($32\,\mathrm{ns}$ in comparison to $34\,\mathrm{ns}$ delay time). This results in a $2\,\mathrm{ns}$ shorter FWHM and a $1\,\mathrm{ns}$ earlier center position for the detection probability distribution of 20000 electrons injected charge. Such an effect was not seen during the measurements with sample 11-5B, nor during the laser

---

[11]Irradiation causes additional energy levels inside the sensor lattice. These energy levels can capture electrons or holes so that these are no longer available for a sensor signal. Instead electrons and holes are released after several µs and get lost for the signal. This effect is called "trapping".

delay measurements with sample 4-6B. For the FWHMs and for the center positions the same values were expected for both injected charges. By comparing the FWHMs of sample 11-5B and sample 4-6B it appears to be more likely that the measurement with 10000 electrons injected charge showed a too large FWHM. Here again, the reason for this behaviour is ascribed to cable delay problems, because the observed effect cannot be explained with any sensor, FE-chip or irradiation behaviour.

Analogous to the measurements with sample 11-5B it is shown that the slopes are not injection charge dependent.

Similar to the laser delay measurement, the hit detection probabilities on the plateaus were different for both injected charges. The measured hit detection probability of 20000 electrons injected charge was 0.3 ± 0.4 ns higher than that of 10000 electrons injected charge. Again it is possible to relate the higher hit detection probability of the injected charge of 20000 electrons to irradiation effects, but the effect is very small and could also be caused by statistical fluctuations.
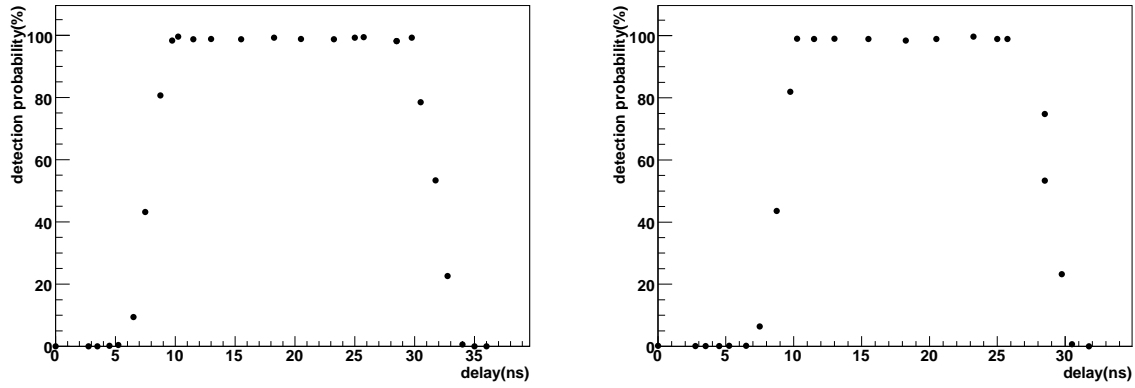
Figure 6.13: Hit detection probabilities for sample 4-6B while delaying the trigger; left: 10000 electrons injected charge; right: 20000 electrons inject charge.

The comparison between the slopes of the laser and the trigger delay measurements showed that the slopes of the laser delay measurement were longer than these of the trigger delay measurement. For 10000 electrons injected charge the slopes were 0.75 ± 0.06 ns wider, for an injected charge of 20000 electrons they were 0.75 ± 0.07 ns wider. Again, the reason for the wider distributions of the laser delay measurements were associated with the sensor behaviour and with the spread of the laser intensity distribution (see chapter 6.1.1). Similar to the measurements with sample 11-5B, the slopes caused by the electronics could be shown. For an injected charge of 10000 electrons the electronics caused slope was 1.14 ± 0.05 ns, for a charge of 20000 electrons it was 1.03 ± 0.05 ns. Relative to those from the trigger delay measurements, the slopes received from the laser delay measurements were broader. As well as for sample 11-5B, this was linked to sensor issues and laser intensity fluctuations.

The plateau values of the hit detection probabilities for the trigger delay measurements, were higher than those for the laser delay measurements. For an injected charge of 10000 electrons the plateau value is $(0.7 \pm 0.4)\%$ higher. For an injected charge of 20000 electrons it was $(0.6 \pm 0.2)\%$ higher. No explanation could be found for this behaviour. For both typs of measurements, on the center of the hit detection probability distribution plateau, the laser pulses and the trigger signal both arrive in the middle of a bunchcrossing. So the conditions of the system were the same. Again, a reason for this behaviour can be assumed in the USBPix system, as it seems

unlikely that this is an intrinsic behaviour of the module.

6.3.3 Laser and Trigger Delay
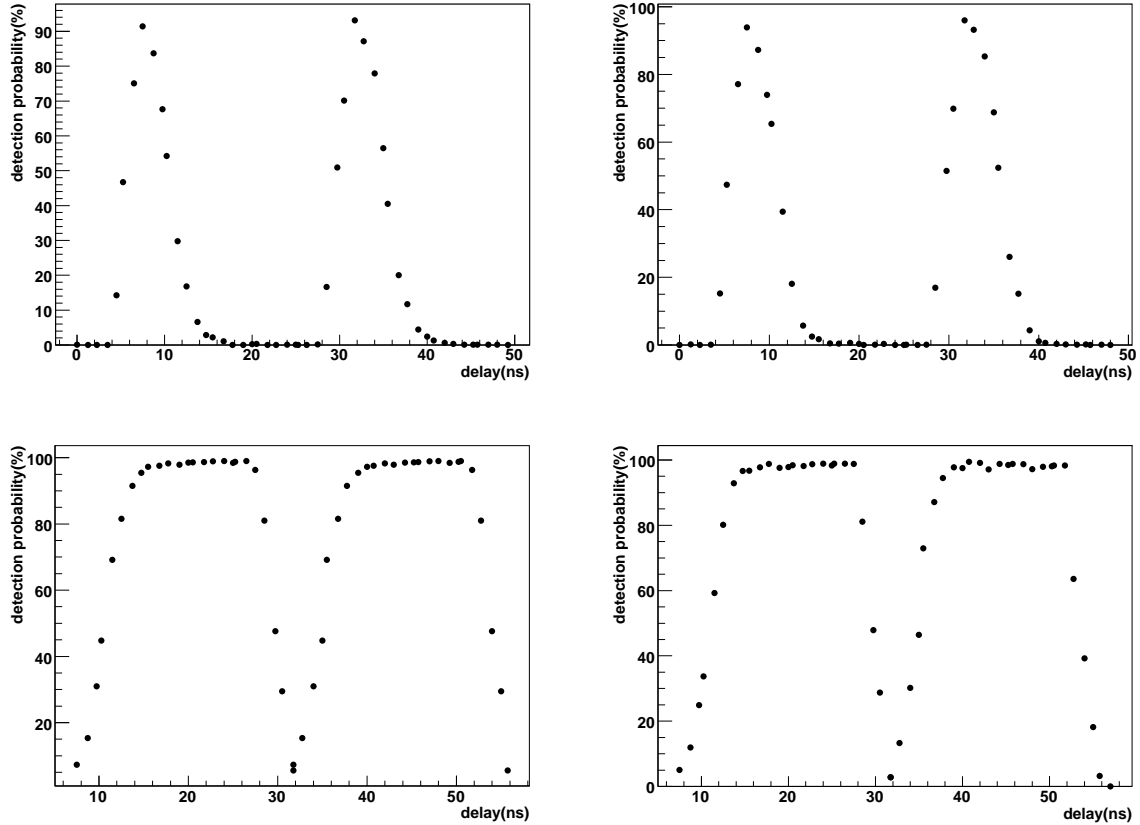
Figure 6.14: Hit detection probabilities for sample 4-6B, LV1ID 8 (above) and LV1ID 9 (below). On the left the plots for 10000 electrons injected charge are shown, on the right these for 20000 electrons injected charge.

Figure 6.14 shows the laser and trigger delay measurement for 10000 and 20000 electrons injected charge for the LV1ID's 8 and 9. The delay time range was chosen long enough to measure two hit detection probability distributions. The FWHMs of the distributions are shown in table 6.6, as well as the laser injection times T, seperately for each hit detection probability distribution. The average T_{avg} of the two distributions was calculated for both injected charges. As for sample 11-5B the different rising and falling times of the hit detection probability distributions are shown in figure 6.14.
It can be seen that the injection times are very similar for both measured distributions. For 10000 electrons the charge was injected 0.9 ± 0.2 ns later than for the 20000 electrons injected charge. Based on the laser delay measurement it was expected that the charges were injected at the same time, but also in this measurement the timwalk is smaller than for sample 11-5B. A possible explanation can be that after irradiation, the timewalk for higher charges shows similar behaviors as for low charges.

	10000 e^-		20000 e^-	
	LV1ID 8	LV1ID 9	LV1ID 8	LV1ID 9
Width 1	$4.5 \pm 0,2$	$19.8 \pm 0,2$	$6,4 \pm 0,3$	$18.7 \pm 0,2$
T	$19.8 \pm 0,2$		18.7 ± 0.2	
Width 2	5.3 ± 0.1	$19.44 \pm 0,08$	$6.4 \pm 0,2$	$18.7 \pm 0,2$
$T\,2$	19.44 ± 0.08		18.7 ± 0.2	
Avg T_{avg}	$19,6 \pm 0.2$		18.7 ± 0.3	

Table 6.6: Overview of the widths and injection times for the laser and trigger delay measurements with sample 4-6B.

6.4 Comparison of the Samples

6.4.1 Hit Detection Probabilities Distribution Slopes

Table 6.7 shows the measured slopes for sample 11-5B and sample 4-6B. Additionally, the calculated differences between the slopes of both samples are shown. It is apparent that the slopes of sample 4-6B, which were measured in the laser delay measurements, were wider than those of sample 11-5B. For an injected charge of 10000 electrons they were 0.56 ± 0.06 ns wider, for 20000 electrons injected charge they were 0.48 ± 0.06 ns wider. The cause for this increase of the slopes was the irradiation of sample 4-6B. Responsible for the width of the slopes are the spread of the laser intensity distribution, the spread of the charge signal, which comes from the sensor, and the behaviour of the FE-electronics as well. The spread of the laser intensity distribution is independent from the sample so this could not be the wider slopes' cause. The spreads difference between the slopes was thus created by the Front-End electronics and the sensor behaviours.

		slope [ns]		
	Injected charge	11-5B	4-6B	Difference
Laser delay	10000 e^-	1.33 ± 0.05	1.89 ± 0.04	0.56 ± 0.06
	20000 e^-	1.30 ± 0.04	1.78 ± 0.05	0.48 ± 0.09
Trigger delay	10000 e^-	1.11 ± 0.04	1.14 ± 0.05	0.03 ± 0.06
	20000 e^-	1.14 ± 0.06	1.03 ± 0.05	-0.11 ± 0.08
Difference	10000 e^-	0.22 ± 0.06	0.75 ± 0.06	0.53 ± 0.8
	20000 e^-	0.16 ± 0.07	0.75 ± 0.07	0.6 ± 0.1

Table 6.7: Measured slopes for sample 11-5B and sample 4-6B with the different delay types. The bottom row shows the differences between the slopes that were measured with the laser delay measurement and these measured with the trigger delay measurement. The last column shows the slope differences between sample 11-5B and sample 4-6B.

The wider slopes of the irradiated sample result in the fact that the interval in which a hit can be related to two bunchcrossings, is increased. If a charge is injected during this time interval, it cannot be decided to which bunchcrossing it belongs.

The slopes of sample 11-5B and sample 4-6B, which were measured with the trigger delay measurements, were nearly equal. For an injected charge of 10000 electrons the slopes were, in the range of the errors, the same, the difference was calculated as 0.03 ± 0.06 ns. For 20000 electrons injected charge the slopes of sample 11-5B were larger than these of sample 4-6B, the difference here was 0.11 ± 0.07 ns. It is apparent from the slope differences between both samples that the irradiation did not broaden the slopes. The widths of the slopes depend on the clock, the beginning of the acceptance window and the electronics. Neither the clock nor the beginning of the acceptance window, which means the time of the trigger input, are influenced by the irradiation. So the behaviour of the slopes resulted only from the FE-electronics and here no worsening was observed. As described above, sensor behaviours had no influence on this measurement.

In chapter 6.2 and 6.3 the differences between the slopes of the laser delay measurements and of the trigger delay measurements were calculated. They are shown in the bottom row of table 6.7, too. These differences gave an upper limit on that part of the slope that was created by the sensor behaviours. Because the laser intensity fluctuations are independent from the used module, the difference between these values show the changing of the sensor performance. For an injected charge of 10000 electrons the difference was 0.53 ± 0.08 ns, and for 20000 electrons it was 0.6 ± 0.1 ns. This result shows that the irradiation of the sensor broadens the slopes of the hit detection probability distributions. The calculated values were equal for both injected charges, so it seems that this effect is not injection charge dependent.

6.4.2 Hit Efficiency Measurement in the Middle of a Bunchcrossing

The plateau heights for sample 11-5B were $(100 \pm 0.1)\%$ for both injected charges and both delay types (laser and trigger delay). This means that in the middle of a bunchcrossing every injected charge was detected. For sample 4-6B, however, the detection probability on the plateau was smaller than 100% for both injected charges and both delay types (see table 6.8). This suggests that the hit detection probability of the sample was diminished by irradiation. A hit detection probability of approximately 98% was also seen before at samples which were irradiated with a similar dose [45].

		Plateau high in [%]		
	Injected charge	11-5B	4-6B	Difference
Laser delay measurement	$10000\ e^-$	100 ± 0.1	98.0 ± 0.02	2.0 ± 0.2
	$20000\ e^-$	100 ± 0.1	98.4 ± 0.2	1.6 ± 0.02
Trigger delay measurement	$10000\ e^-$	100 ± 0.1	98.7 ± 0.04	1.3 ± 0.4
	$20000\ e^-$	100 ± 0.1	99.0 ± 0.1	1.0 ± 0.01

Table 6.8: Plateau values for the hit detection probabilities with samples 11-5B and 4-6B. Also shown are the differences between both modules.

6.4.3 Timing and Timewalk

Table 6.9 gives an overview of the injection times T_{inj} and the laser delay measurement center positions x_0 for sample 11-5B and sample 4-6B. Additionally shown is the calculated timewalk, which shows for both methods an irradiation dependency. The measurements show, that the

timewalk is smaller when the sensor is irradiated. A possible explanation can be that, by irradiation, the worsening of the preamplifier behaviours is more distinct for high charges. This assumption can be proven by redoing the plot of figure 6.9 with an irradiated sample. The described behaviour would appear in a graph that has a similar shape as the old one, but with a lower maximum.

	Injected charge	11-5B	4-6B
T_{avg} [ns]	$10000\ e^-$	15.6 ± 0.1	19.6 ± 0.2
	$20000\ e^-$	12.3 ± 0.2	18.7 ± 0.3
Timewalk		3.3 ± 0.2	0.9 ± 0.4
x_0 [ns]	$10000\ e^-$	27.85 ± 0.04	23.51 ± 0.4
	$20000\ e^-$	30.49 ± 0.04	23.53 ± 0.1
Timewalk		2.64 ± 0.06	0.02 ± 0.04

Table 6.9: Comparison of the laser injection times: Laser injection time from the trigger and laser delay measurements and center position from the laser delay measurements with sample 11-5B and sample 4-6B. The calculated timewalk is shown too.

6.5 Conclusion

Considering the results it can be stated that the hit detection probability measurements showed several unexpected effects, which could not be explained with sensor or Front-End effects. Most of them were ascribed to problems with the setting of the delay times. It is guessed that a LEMO cable extension was not working well and that this caused an extra delay. This suggestion is supported by the fact that all of the strange measurements had too long delay times. These effects were especially seen in the FWHMs and in the center positions x_0. To prevent those delay time problems, in an improved measurement the delay could be done with an frequency generator and instead of delay cables. This would give more exact delay times, and delay time errors would be prevented.

One result of the measurements is that the timewalk gets smaller when the sensor is irradiated. This effect was observed at the laser and trigger delay measurement and at the center positions measurement of the laser delay measurements. In both cases a clear effect was seen, which is an evidence that the effect is not caused by parasitic errors. But because of the delay time uncertainties, further measurements have to be done to make a final statement about the size of this effect.

The hit detection probability distribution slope measurements showed clear results. It could be shown, that the irradiation of the FE-chip has nearly no influence on the width of the slope. It could also be shown, that the widening of the slopes, in the laser delay measurements, after irradiation is related to sensor issues. The effect itself was, with the whole ATLAS lifetime dose, causing a widening of approximately 0.5 ns, still small.

The hit detection efficiency on the plateau of the distribution differed between samples 11-5B and 4-6B by about 1 to 2%. For sample 4-6B a very small charge dependency of the hit detection efficiency could be shown. Nevertheless the hit detection efficiency of approximately 98% after the irradiation with the ATLAS lifetime dose showed the expected value.

7 Hit Induced Noise

The aim of the measurements that are shown in this chapter was to determine if injecting hits into the sensor increases the noise of the module. For this reason the hit occupancy, which is defined as the number of hits per bunchcrossing and pixel, was calculated. This can be done by measuring the hitbus rate. With a BK Precision 4085 40 MHz Arbitrary/Function Generator with counter, the positive hitbus slopes within a measurement time t=5 minutes were counted. With this rate N the hit occupancy O can be calculated by

$$O = \frac{N/t}{P} \cdot 25\,ns \tag{7.1}$$

where P is the number of module pixels. For single chip sensors, which where used for these measurements, P=2880. For the calculation of the hit induced noise occupancy, measurements were done while the sensor was irradiated with an Americium 241 source and without a source. The experiments are based on several assumptions. For the measurement with a source it was assumed that for a high threshold the hit occupancy O_{high} is created by two parts. The first part is the noise occupancy $O_{high,noise}$. It is created by the noise of the module. The discriminator threshold is more often exceeded by the noise of the analogue part of the read out chain when the threshold is low than when it is high. So at a high threshold the noise occupancy is low and it increases when decreasing the threshold. The second part of the hit occupancy $O_{high,source}$ is created by the hits that are produced by the Americium source.
For a low threshold it was assumed that the hit occupancy O_{low} is created by three parts. The first two are the same as at the high threshold: $O_{low,noise}$ for the noise occupancy without a source and $O_{low,source}$ for the occupancy that is created by the source[1]. The third part is the hit induced noise occupancy $O_{hitnoise}$.

$$O_{high} = O_{high,noise} + O_{high,source} \tag{7.2}$$

$$O_{low} = O_{low,noise} + O_{low,source} + O_{hitnoise} \tag{7.3}$$

$O_{high,noise}$ can be measured at a high threshold without a source. With a second measurement at a high threshold, but with the source, the sum of the source occupancy and the noise occupancy O_{high} can be measured.
Likewise, at the low threshold $O_{low,noise}$ can be measured without a source and O_{low} with the source. With these four measurements the hit induced noise occupancy is calculated:

$$O_{hitnoise} = O_{low} - O_{low,noise} - (O_{high} - O_{high,noise}) \tag{7.4}$$

For the calculation of the hit induced noise occupancy each measurement was done ten times. As high threshold 4000 electrons were chosen. As low thresholds 2500 electrons, 2100 electrons and the threshold of the incremental threshold scan (see below) were chosen. With these thresholds a possible threshold dependency of the hit induced noise can be shown.

---

[1]The rate of the source does not depend on the threshold $O_{low,source} = O_{high,source}$.

Incremental Threshold Scan

With the incremental threshold scan the minimal threshold at which measurements are still possible, is found. For this reason a special tuning procedure was implemented where the T-DAC values are decreased individually for each pixel. After the T-DAC value is decreased a threshold scan is done and the noise of the threshold (see chapter3.1.2) σ is checked. If σ is smaller than a set cut value, the scan is considered successfully, if it is larger the scan failed. This noise cut can be set manually separately for normal, long, ganged and inter-ganged pixels. The cuts shown in table 7.1 where used for sample 11-5B.

In the beginning of the tuning procedure the T-DAC values are decreased by five digital units (DU). If the scan is considered successfully, the T-DAC is again decreased by five DU. If the noise is to high, the scan failed and the T-DAC is increased by five DU. Then the step size is reduced by one and the T-DAC is decreased again. This procedure is done until the minimal possible T-DAC value for every pixel is found.

After this scanning procedure all T-DAC values are increased by one. This step is done to get a more stably working module. With this incremental threshold scan the minimal threshold of the module can be found. After the whole scanning procedure a threshold scan is done to find the threshold of the module. For the used sample 11-5B the minimal threshold was 1900 ± 25.8 electrons with a noise σ of 238 ± 27.59 electrons.

| Pixel type	normal	long	ganged	inter-ganged
Cut [e]	300	350	450	350

Table 7.1: Noise cuts for the incremental threshold scan.

Hitbus Measurements

With the USBPix system it is possible to measure the hitbus signal by connecting the counter to a LEMO connector. The counter measures the number of positive hitbus slopes. At a measurement without a source, on a high threshold (e. g. 4000 electrons), there are nearly no noise hits. Only hits from cosmic muons are expected. With the source, the pure source rate should be measured, except a small contribution from cosmic muons.

Approximately 10000 muons per square meter and minute reach the surface of the earth [46]. For the senor area of approximately $0.6\,\mathrm{cm}^2$ 0.62 muons are expected in one minute. This results in 3.1 muons for a measurement time of five minutes. The average of ten measurements with a threshold of 4000 electrons and without a source gives 3.8 ± 0.7 muons within five minutes. That shows that at a threshold of 4000 electrons, nearly no noise hits are created.

Figure 7.1 shows that the plotted noise occupancy increases, when the threshold is reduced. Furthermore, it is shown that for a certain threshold the noise level fluctuates very strongly. The measurements illustrated by red circles and pink triangles were done with sample 11-5B. The red circles show the average values of ten measurements. These were the measurements that were used to calculate the hit induced noise occupancy. The pink triangles show single measurements that were recorded with another module configuration. Finally, the blue squares show measurements [46] that were recorded with a different single chip card. It can be seen that for similar thresholds the occupancies differ a lot, even if the same sample and configuration is observed. The large fluctuations in the occupancy are related to different external parameters
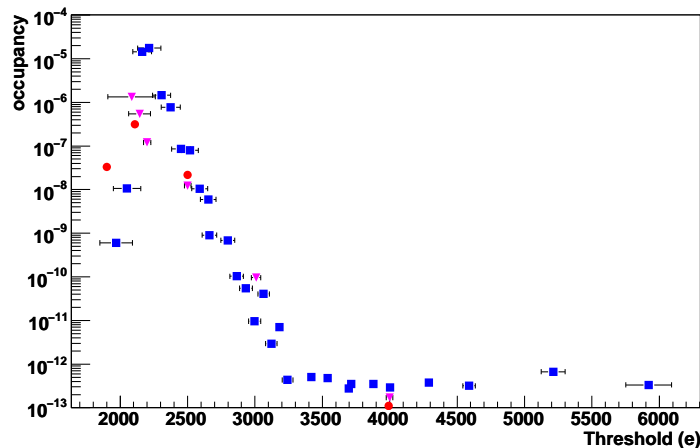
Figure 7.1: Noise occupancy versus threshold. The red circles show the average values from ten single measurements, taken with sample 11-5B. With pink triangles measurements that were also taken with sample 11-5B, but with another module configuration, are shown. The blue squares show measurements with another single chip card [46].

like electromagnetic pick-up, ripples on the buildings power nets, temperature etc. [46]. These external influences lead to a bad reproducibility of the hitbus measurement for very low thresholds.

In figure 7.1 it is shown that for low thresholds the occupancy decreases again. This can be explained by the hitbus noise, which is so big that the signal does not fall to logical zero again after every single hit. So the number of positive slopes is reduced. Furthermore, it is shown that the occupancy, where the hitbus rate starts decreasing again, varies for different measurements.

7.1 Results

4000 Electrons Threshold

For the measurement at high threshold a setting of 4000 electrons was chosen. The threshold tuning for 4000 electrons resulted in a threshold of 3993 ± 25.44 electrons. The noise σ was 201.9 ± 8.4 electrons. During the hitbus measurement without a source 3.8 ± 0.7 hits were measured in five minutes. That conforms a hit occupancy $O_{high,noise}$ of $(1.1 \pm 0.2) \cdot 10^{-13}$. The measurement reveals that at this threshold the hits occur according to the rate of cosmic muons. With the source 127299 ± 96 hits were collected. This gives an occupancy of $O_{high} = (3.683 \pm 0.003) \cdot 10^{-9}$.

2500 Electrons Threshold

The tuning for the threshold of 2500 electrons gave a mean value of 2499 ± 24.2 electrons and a noise σ of 198.5 ± 8.48 electrons. The measurement without the source gave 755588 ± 21652 counts in five minutes and an occupancy $O_{low,noise}$ of $(2.18 \pm 0.06) \cdot 10^{-8}$. With the source the rate was 825913 ± 10575. This gave an occupancy of $O_{low} = (2.39 \pm 0.03) \cdot 10^{-8}$. With this measurement and the measurement at the high threshold the hit induced noise occupancy could

be calculated with equation (7.4) as $(-1.6 \pm 0.7) \cdot 10^{-9}$.

A negative occupancy does physically not make sense. It is mentioned that this result occurs in the measurement at 2500 electrons threshold without the source. In these ten measurements the measured rate was rising from measurement to measurement (from 670055 counts to 891796 counts, see figure 7.2). This behaviour is attributed to external influences.
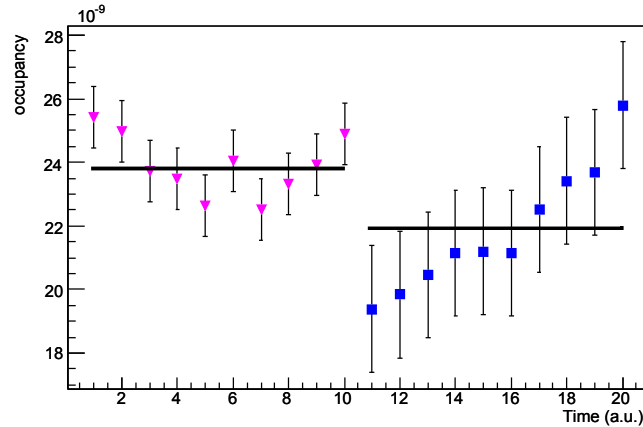
Figure 7.2: Occupancy plotted as a function of the time when the measurement was taken, for a threshold of 2500 electrons. The first measurement got the timestamp 1, the last one the timestamp 20. The time between two measurements was approximately five minutes. The blue squares signify the noise measurements, the pink triangles those with the source. The mean values are shown with the black lines.
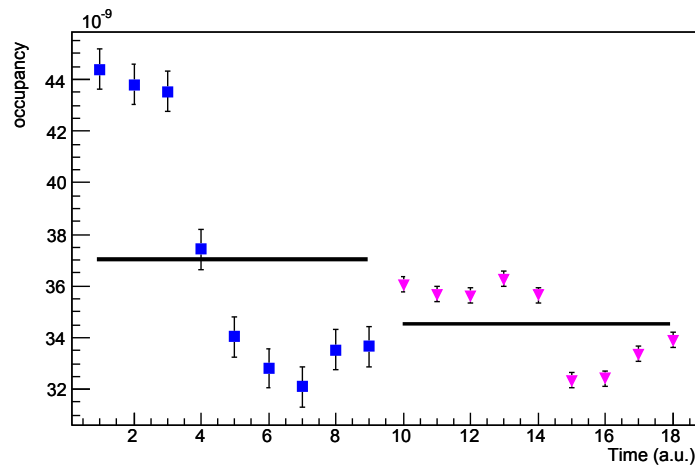
2100 Electrons Threshold

The tuning for the threshold of 2100 electrons resulted in 2108 ± 37.88 electrons as mean value and 203.7 ± 10.4 electrons for the noise. Without the source a rate of 10775615 ± 24189 counts was measured. With the source the rate was 11976960 ± 155216. This gave occupancies of $O_{low,noise} = (3.118 \pm 0.007) \cdot 10^{-7}$ and $O_{low} = (3.47 \pm 0.04) \cdot 10^{-7}$. With these values the hit induced noise occupancy was calculated to $O_{hitnoise} = (3.1 \pm 0.5) \cdot 10^{-8}$. This is $9.9 \pm 1.6\%$ of the total noise occupancy.

Minimal Threshold

The minimal threshold scan gave a threshold of 1900 ± 25.8 electrons with a noise σ of 238 ± 27.59 electrons. In the measurement without a source a leap was observed (see figure 7.3). The first five measurements had a rate of approximately 1.5 million counts in five minutes, then the rate jumped to approximately 1.1 million counts in five minutes. During the measurement with the source, a leap was observed once more after five measurements. This time the rate jumped from approximately 1.3 million counts in five minutes to 1.1 million counts in five minutes. The cause of these leaps in the hitbus rate was again assumed in external sources.

Another problem, of a measurement at such a low threshold is that it lies behind the maximum of figure 7.1. Here, it is expected that at a rising rate the counted hitbus slopes are decreasing (see chapter Hitbus measurements). This leads to negative hit induced noise occupancies which causes this kind of measurement to be unapplicable.

Figure 7.3: Occupancy plotted as a function of the time when the measurement was taken, for a threshold of 1900 electrons. The first measurement got the timestamp 1, the last one the timestamp 20. The time between two measurements was approximately five minutes. The blue squares signify the noise measurements, the pink triangles the measurements with the source. The mean values are shown with the black lines.

Conclusion

Table 7.2 shows the results of the hit induced noise measurements. It can be seen that only the measurement at a threshold of 2100 electrons shows a physically reasonable result. For the measurement with a threshold of 2500 electrons and 1900 electrons leaps or the slowly but continuously changing of the occupancy were seen. They result in a bad reproducibility of the measurements.

Threshold [e]	Hit induced noise occupancy	% of noise occupancy
2500 (all values)	$(-1.6 \pm 0.7) \cdot 10^{-9}$	/
2100	$(3.1 \pm 0.7) \cdot 10^{-8}$	9.9 ± 1.6
minimal threshold	/	/

Table 7.2: Hit induced noise occupancies for three different thresholds.

Only the measurement at a threshold of 2100 electrons showed a clear existence of hit induced noise. The remaining measurements at a low threshold showed not understood effects which seem to come from external sources. The measurement at a threshold of 1900 electrons showed no result. At such low thresholds the noise level is so high that the counting of the rising hitbus slopes is no longer a useful method. Another possibility to measure the hitbus rate could be the measurement of the time on which the hitbus has the level high in comparison to the entire measurement time.

Concluding it can be said, that the outer influences on the hitbus measurement prevent a reproducible and quantitative measurement of the hit induced noise rate. To quantify this effect, more measurements with a better hitbus measurement method have to be done.

8 Summary and Outlook

For the measurements that are described in this thesis a laser system for charge injection in a semiconductor sensor was built. The adjustment of this laser system was one of the main tasks that had to be done for the realization of these measurements. The whole system was built to be flexible, the changing of the used laser head or the changing of the devices under test is possible within a few minutes. Two laser heads, with wavelengths of 671 nm and 1060 nm, which are used to inject charge in different depths into a sensor, are available. For the realization of different beamspot diameters one can choose between four different objective lenses. The laser intensity can be set by an attenuator, and the temperature of the device under test can be controlled, too.

During the measurements the system showed a good performance and allowed very precise charge injection. In chapter 4 it was shown that it is possible to set injection charges with an accuracy of several ten electrons. The system also allows injecting charges of less than 100 electrons, or more than 200000 electrons, in silicon. With the $20\times$ object lens it is possible to reach laser beamspot diameters of about $10\,\mu\mathrm{m}$. With a finer adjustment of the laser system's components it will be possible to reach even smaller beamspot diameters. Furthermore, the re-installation of the $50\times$ objective lens will lead to a much smaller beamspot diameter. With these improvements it will be possible to do spatially resolved measurements within one single pixel.

With the help of this laser system it was possible to examine different module behaviours. The possibility of doing time resolved measurements allowed to disentangle the behaviours of the FE-chip and the sensor by injecting charges at various times. The comparison of an unirradiated sample with an irradiated one lead to statements about irradiation caused changes of the hit detection efficiency during a bunchcrossing. These measurements showed, after the irradiation with the ATLAS lifetime dose, very good FE-chip as well as good sensor performances.

The irradiation caused changing of the hit detection probability, and its behaviour at the edges of a bunchcrossing were shown. Furthermore, an interesting change in the timewalk behaviour was observed. Additionally, some not understood effects were observed during the measurements. It was suggested that some of these effects have their origin in the setting of the charge injection time. This was the biggest problem occurring during the measurements, where the biggest source of errors was the setting of the laser injection time by extending a delay cable. For a better time resolution and a more exact setting of the charge injection time this delay mechanism has to be improved. A possible mechanism, which is able to fulfill such a task, is a frequency generator with two outputs triggered by the same signal. If one of these outputs has the possibility to send its signal delayed, the laser injection time can be set very precisely and mechanical defects in the delay line can be excluded.

The hit induced noise measurements by measuring the hitbus rate were not successful. For further investigation on this effect, a completely new method to measure the hitbus, or even the sensor noise itself, has to be invented.

In conclusion, it can be said that as long as the modules are working, the hit detection efficiency

is good. So even when the ATLAS lifetime dose for the b layer is exceeded (after approximately five years), the modules are supposed to work with a good hit detection probability.

Bibliography

[1] D. Griffiths, *Einführung in die Elementarteilchenphysik*, vol. 1, Akademie Verlag, (1996).

[2] *Standard Model of Elementary Particles*, website, available online at
http://www.neuroquantology.com/repository/index.php?option=com_fireboard&Itemid=54
&func=view&catid=40&id=44; visited on March 21th 2011.

[3] K. Nakamura et al, *Review of Particle Physics*, Jornal of Physics **G 37** (2010).

[4] The LEP Higgs Working Group, *Search for the Standard Model Higgs Boson at LEP*,
arXiv:hep-ex/0306033v1.

[5] *Supersymetric Particles*, website, available online at
http://hasylab.desy.de/images/content/e232/e242/index_eng.html; visited on March 29th
2011.

[6] *Overall View of the LHC Experiment*, website, available online at
http://livefromcern.web.cern.ch/livefromcern/antimatter/history/historypictures/LHC-
drawing-half.jpg; visited on November 17th
2010.

[7] *LHC Design Report*, CERN-2004-003-V-2 (2007).

[8] M. Lamon, *Status of LHC*, website, available online at
http://indico.cern.ch/getFile.py/access?contribId=0&resId=1&materialId=
slides&confId=113256; visited on April 18th 2011.

[9] J. Grosse-Knetter, *Vertex Measurement at Hadron Colider - The ATLAS Pixel Detector*,
University Bonn (2007).

[10] *The Atlas Experiment*, website, available online at http://www.atlas.ch; visited on
October 14th 2010.

[11] The ATLAS Collaboration, *The ATLAS Inner Detector commissioning and calibration*,
arXiv:1004.5293v2 (2008).

[12] B. M. Demirköz, *Construction and Performance of the ATLAS SCT Barrels and Cosmic
Tests*, Oxford University (2007).

[13] *The ATLAS Muon system*, website, available online at http://www.physik.uni-
wuerzburg.de/fileadmin/11010700/Teilchenphysik/ATLAS-muon-xy-tdr.jpg; visited on
November 24th 2010.

[14] *The ATLAS Pixel Detector*, website, available online at
http://www.atlas.ch/inner_detector1.html; visited on Mai 5th 2011.

[15] M. George, *Implementation of an Electronical Read-Out System for Multi-Module Laboratory Tests of the ATLAS Pixel Detector; diploma tesis*, Georg-August-Universität Göttingen (2010).

[16] *The ATLAS Pixel Module*, website, available online at http://hep1.physik.uni-bonn.de/atlas_pixels.html; visited on Mai 5th 2011.

[17] C. Gemme, *Study of indium bumps for the ATLAS pixel detector*, Nuclear Instruments and Methods in Physics Research **465** (2001).

[18] F. G. Hügging, *Der ATLAS Pixel Sensor Der state-of-the-art Pixelsensor für teilchenphysikalische Anwendungen mit extrem hohen Strahlungsfeldern; PHD Thesis.*

[19] P. Hettkamp, *Messungen zur Charakterisierung der Ladungsmessung von DEPFET-Matrizen durch Lasereinstrahlung; diploma thesis*, University Bonn (2007).

[20] F. Scholz, H. Henneken, P. Kuschnerus, H. Rabus, M. Richter, and G. Ulm, *Determination of the electron-hole pair creation energy for semiconductors from the spectral responsivity of photodiodes*, Nuclear Instruments and Methods in Physics Research **A 439** (2000).

[21] T. Flick, *Studies on the Optical Readout for the ATLAS Pixel Detector; Systematical Studies on the Functions of the Back of Crate Card and the Timing of the Pixel Detecto; PHD Thesis.*

[22] F. Huegging, *Der ATLAS Pixel Sensor; PHD Thesis*, Universität Dortmund (2001).

[23] T. Flick, *Studies of the Optical Readout for the ATLAS Pixel Detector; PHD Thesis*, Universität Wuppertal (2006).

[24] *Neutron fluence*, website, available online at http://rd11.web.cern.ch/RD11/rkb/PH14pp/node123.html; visited on Mai 20th 2011.

[25] O. Krasel, *Charge Collection in irradiated Silicon-Sensors; PHD Thesis*, University Dortmund (2004).

[26] J. Schneider and H. Krüger, *S3 Multi IO System*, website, available online at http://icwiki.physik.uni-bonn.de/twiki/pub/System/WebHome/S3_Multi_USB_V1.0_Documentation; visited on Mai 26th 2011.

[27] *USBPix - USB based readout system for ATLAS FE-I3 and FE-I4*, website, available online at http://icwiki.physik.uni-bonn.de/twiki/bin/view/Systems/UsbPix#Introduction; visited on Mai 10th 2011.

[28] H. Krüger, *Test Systems for ATLAS Pixel Detector Upgrade Activities*, University Bonn (2008).

[29] K. Schmieden, *Charakterisierung einer neuen Generation von DEPFET-Sensoren mit Hilfe eines Lasermesssystems; diploma thesis*, University Bonn (2008).

[30] A. R. Shayan, *Laser absorption for Si and SiC*, website, available online at www.wmich.edu/mfe/mrc/Amir%20and%20Broga_Laser%20Absorbtion%20for%20Si%20and%20SiC_10-24-2008.pdf.

[31] D. McMorrow at al., *Subbandgap Laser-Induced Single Event Effects: Carrier Generation via Two-Photon Absorption*, IEEE Transactions on nuclear science **49** (2002).

[32] *Picosecond Injection Laser (PiLas) - Owner's Manual Rev. 0.3 Dec. 04*, Advanced Laser Diode Systems A.L.S. GmbH (2004).

[33] *Private communications with Boris Khoury from ALS.*

[34] *Sony CCD Black-and-With Video Camera Module - Operating Instructions*, Sony Coperation (1999).

[35] *Probe Systems PA300IS PA300PS - User Manual M10-123299ß02*, Süss MicroTec 2006.

[36] att systems, *Manual Control Unit A Series B Series C Series*, ATT Systems GmbH 2004.

[37] *Manual: Präzisions Temperatursensor CON-TS-NTC*, Hygrosens Instruments GmbH 2008.

[38] *Hamamatsu Si photodiode with preamp S9269, S9270 Datasheet*, Hamamatsu Photonics K.K. Solid State Division (2004).

[39] F. Köhler, *Performance Study of a Diamond Pixel Detector Prototype for Future ATLAS Upgrades Using Beam Test Data; diploma teases*, University Göttingen (2010).

[40] F. Kinsey at al., *The NUDAT/PCNUDAT Program for Nuclear Data*, website, available online at
http://web.archive.org/web/20040109104128/www2.bnl.gov/CoN/nuc/C/Cd109.shtml;
visited on March 7th 2011.

[41] *Industrial Radiation Sources - Product information*, Eckert & Ziegler Isotope Products 2008.

[42] F. K. Kneubühl and M. F. Sigrist, *Laser*, vol. 7, Vieweg+Teubner, (2008).

[43] *Private communications with Matthias George.*

[44] *Serie AFG3000 Arbiträrsignal-/Funktionsgeneratror Schnellstart-Benutzerhandbuch*, Tektronix 071-1633-04.

[45] T. Lari, *Radiation hardness studies of silicon pixel detectors*, Nuclear Instruments and Methods in Physics Research **A 560** (2005).

[46] J. Rieger, *Bachelor's Thesis: Measurement of Operational Stability of the ATLAS Pixel Read-Out Chip at low Threshold*, Georg-August-Universität Göttingen (2010).

Acknowledgements

First of all I would like to thank Prof. Dr. Arnulf Quadt, who gave me the possibility to write my diploma thesis in his working group. It has been a great experience to work in a field of research, where the fundamental coherences in nature are explored.
I also want to thank PD. Dr. Jörn Grosse-Knetter for his supports and for a large number of great ideas during the evolution of this work.

Especially I would like to thank Dr. Jens Weingarten, my supervisor during my time in the II physical institute. Without his help and his supervision, this thesis would not have been possible. I would like to thank him for the stimulating discussions and for the great help by fixing many problems which occurred during this thesis.

I also want to thank Natascha, who had reviewed this thesis and had supported me during the work on this thesis. Last, but not least, I would like to thank the whole HEP working group of the II physical institute for a great time and a good working atmosphere.